MONITORING OF TRANSFORMER OIL USING MICRODIELECTRIC SENSORS

by

Lama Mouayad

B.S., Massachusetts Institute of Technology
1983

SUBMITTED IN PARTIAL FULFILLMENT
OF THE REQUIREMENTS FOR
DEGREE OF

MASTER OF SCIENCE

at the

MASSACHUSETTS INSTITUTE OF TECHNOLOGY

February, 1985

© Massachusetts Institute of Technology 1985

Signature of Author ....
Department of Electrical Engineering
and Computer science, February 1, 1985

Certified by ....
J. R. Melcher
Thesis Supervisor

Accepted by ....
A. C. Smith
Chairman, Departmental Committee
on Graduate Student

سلسلة الدراسات

MONITORING OF TRANSFORMER OIL

USING MICRODIELECTRIC SENSORS

by

Lama Mouayad

ABSTRACT

The possibility of using microdielecric sensors in an
on-line monitoring system of transformers is examined. A
numerical technique based on a transfer relation approach is
used to solve for the field in the sensor. This numerical
approach facilitates the inclusion of surface effects. The
sensor geometry has a mixed boundary at the sensor/fluid
interface, and the numerical technique used here is equally
applicable to other mixed boundary value problems.

The sensors show a clear difference between the response of
clean oil and contaminated oil obtained from a failed
transformer. The microscopic dimensions of the sensors make
them sensitive to surface phenomena. The surface phenomena
can provide additional information about the state of the
transformer not necessarily reflected in changes of the bulk
properties of transformer oil.

Experimental work using the microdielectric sensors in clean
and contaminated oil shows evidence of heterogeneity caused
by surface phenomena. The main surface phenomena involved
are the polarization of the electrodes caused by space
charge accumulation and a conduction path between the two
electrodes caused by adsorption on the interface.

The polarization of the electrodes increases with the
increase of the bulk conductivity of the oil. Stirring of
the fluid causes a clear reduction of the polarization of
the electrodes caused by turbulence enhanced diffusion.

Acknowledgements

My deepest thanks to Prof. Melcher who gave ample time and attention to guide me through this thesis. His contribution to my education goes beyond the scientific knowledge, to include a welcomed influence on my social awareness and moral stands.

Special thanks to Prof. Senturia for providing valuable advice. Discussions with Dr. Cooke were a great help. Members of the continuum electromechanics group gave a lot of technical assistance and friendly support. Conversations with Mark Zaretsky and Philip von Guggenberg were very helpful. Thanks to Norman Sheppard and Mike Coln from the microelectronics laboratory for their readiness to help. Special thanks to my friends who gave me an essential moral support.

Most of all, my deepest gratitude to my parents and my sisters who helped me in determining my direction in life, and gave me ample encouragement throughout my education. They are always a part of everything I do, and this thesis would not have been possible without their support.

Table of Contents

Table of Figures

Chapter I

Introduction

1.1 Overview of Monitoring of Transformers

Large power transformers are monitored regularly to predict their deterioration and prevent failure [1]. Monitoring the transformers periodically helps in determining the need for service before the transformer reaches a critical state which will cause it to fail.

Many aging processes contribute to the deterioration of the status of the transformer, and the detection of their increase above acceptable levels is essential. These damaging processes can be chemical (i.e. decomposition and oxidation of the insulating oil, decomposition of the cellulose insulation, or sludge formation), mechanical (i.e. vibrations, corrosion, or blockage of the flow in the cooling pipes) or electrical in nature (i.e. electrical discharges). A correlation often exists between some of these aging processes. In some cases, various aging phenomena are triggered by common causes, such as a condition of high moisture in the transformer causing both the deterioration of the dielectric strength of the oil, and the decomposition of the cellulose insulation. In some other cases, one of these phenomena can lead to another, such as the decomposition of the cellulose insulation causing a weakening in the mechanical support of the windings, and leading to an increase of mechanical vibrations.

The oil filling the transformer carries important information about the general state of the transformer, and mirrors most of the degradation events. For example, the thermal aging of the cellulose insulation generates carbon monoxide and carbon dioxide [2], so the detection of these two gasses dissolved in the oil reflects the degradation of the cellulose insulation. This technique of detecting damaging processes by examining the gas content of the oil is well established [3] [4] and is widely practiced by the utility companies in the industry.

In general, the utility industry relies heavily on testing the oil to monitor the status of the transformer. These tests are done by obtaining field samples of oil from the transformer unit, and transporting them to the laboratory where they are analyzed. This style of sampling the oil is costly, and limits the frequency of tests on the oil. Fast developing events cause failure of the unit before being detected by this style of monitoring. Another limitation of this technique is the change of status of the oil between sampling time and testing time. The time delay and the required handling of the oil in sampling and transporting cause a loss of critical information and limit the reliability of the analysis [5] . An on-line continuous monitoring of transformer oil can provide a more reliable technique of fault detection. The development and use of special sensors tuned to the detection of various degradation processes is an attractive possibility. In this

work the use of microdielectric sensors in transformer oil is investigated.

1.2 Background on Microdielectric Sensors

Microdielectric sensors are designed to measure the dielectric properties of a surrounding material. The sensors were developed by Prof. S. D. Senturia and coworkers at M.I.T., and were used to measure the impedance of thin films [6] , and to study the curing of resins [7]. The sensor consists of a pair of planar interdigitated electrodes (figure 1.1) , with an equivalent impedance circuit which is determined by the dielectric properties of the surrounding material. One of the electrodes (the driven gate) is driven by an alternating potential, and the other electrode (the floating gate) assumes a potential which depends on the mutual impedance between the two electrodes and their respective impedances to ground. The floating gate controls the current flowing through a field effect transistor used to amplify the response signal. The floating gate potential is obtained via an interface feedback circuit (figure 1.2) which causes the gate of a reference FET, manufactured on the sensor, to assume the same potential as the floating gate. The ratio of the floating gate potential to that of the driven gate indicates the dielectric properties of the surrounding material. A finite difference simulation was done by Lee [8] under the assumption that the material in question could be modeled as homogeneous and no surface
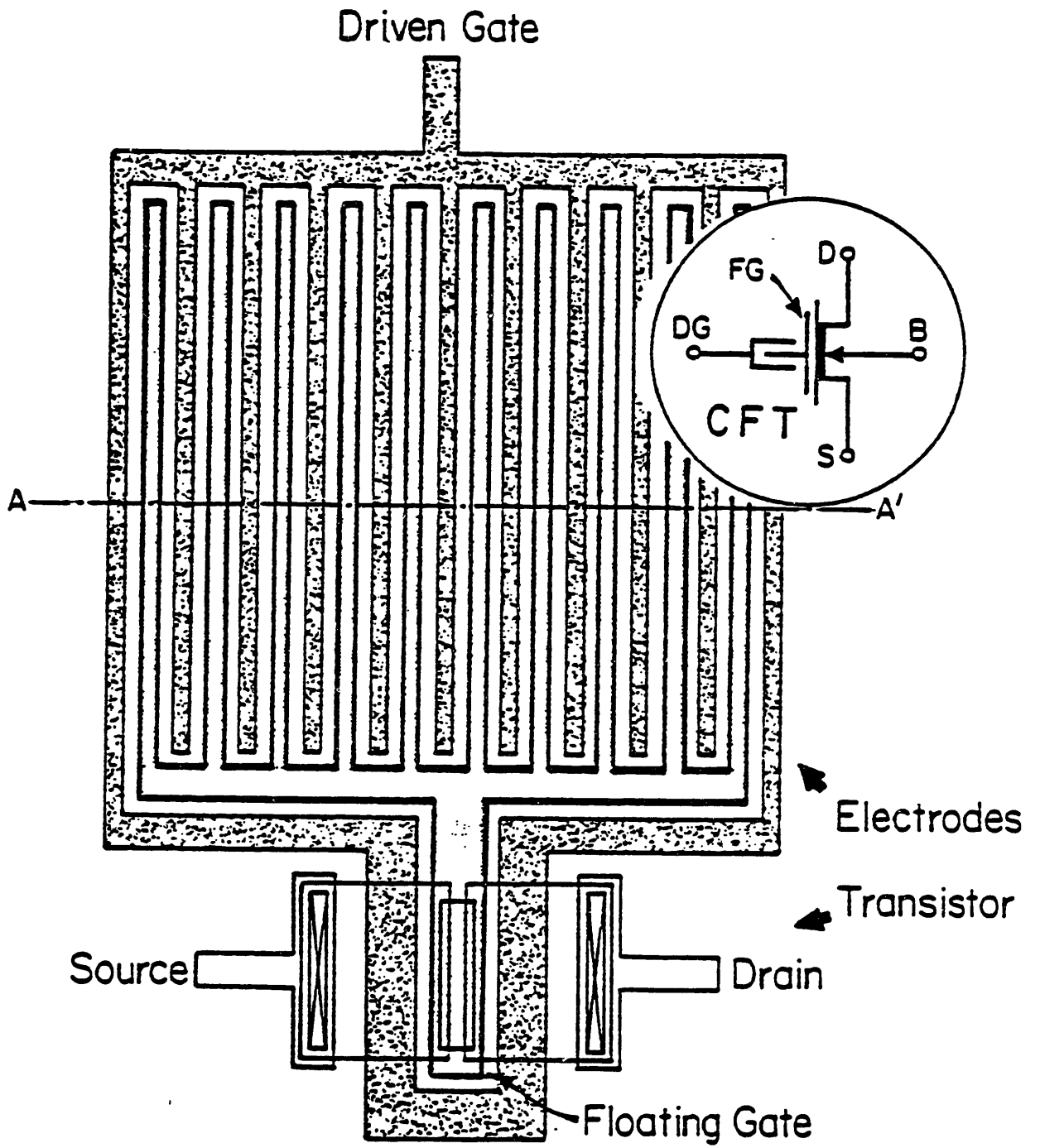
Figure 1.1

Top view of sensor [8]
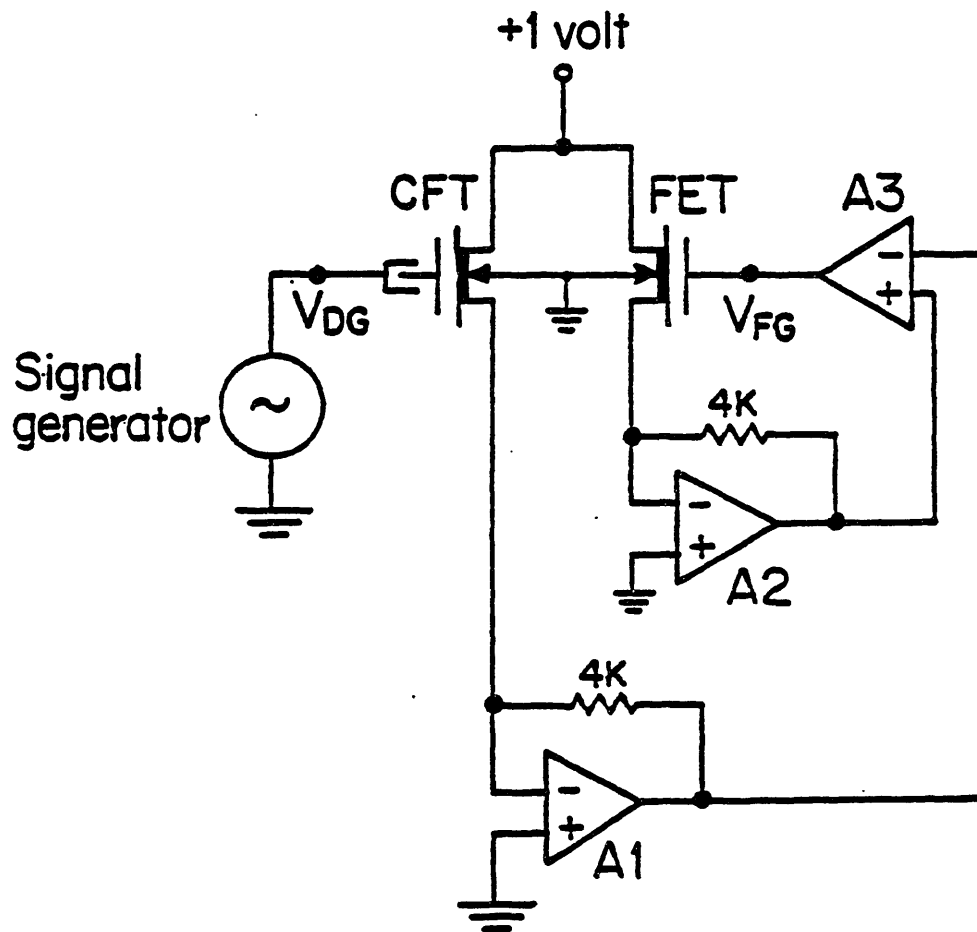
Figure 1.2
Feedback circuit [8]

phenomena are present at the interface, and calibration curves were generated for converting the potential ratio response into the dielectric constant and loss. The sensors provide also a measurement of the temperature based on the current flowing through a pn junction built into the sensor.

1.3 Overview of this Work

Current literature which describes dielectric and loss phenomena in transformer oil and associates trends in the loss with aging processes is summarised. Moisture, a basic factor in the deterioration of transformers, is discussed because of the potential use of the microdielectric sensors to monitor water content in oil.

The microscopic size of the microdielectric sensors makes them sensitive to surface phenomena occurring at the interface of the sensor with the surrounding material. In the case of transformer oil as a surrounding medium, the response of the sensor can be sensitive to a double layer forming at the interface, and to other changes of the surface properties of the sensor/fluid interface due to adsorption of water or other contaminants. The ability to analyze the sensor's response under flexible boundary conditions is needed to be able to account for surface and surface-related phenomena. With such a flexible model, the microdielectric sensor becomes the basis for the identification and study of surface phenomena. Such phenomena have promise for sensing changes in the oil not

16

reflected in a sensitive way in the bulk conductivity and permittivity.

A method for solving for the electric field in the sensor geometry based on a transfer relation approach is developed. This approach facilitates the inclusion of surface phenomena when simulating the response.

Experiments are performed to determine the characteristics of the sensor's response in transformer oil. The sensitivity of sensors to the water content in the oil is examined. The effects of induced motion and added contaminants are studied.

Chapter two of this thesis gives a background on the dielectric properties of transformer oil, and their response to aging events. Chapter three describes the method used to solve for the field in the sensor based on a transfer relation approach. In chapter four, the numerical method developed is used to predict the response of the sensor under various bulk and surface conditions. Experimental work is described in chapter five. Results are discussed and analysed in chapter six, and suggestions of further work needed to tailor the sensors for transformer monitoring are provided in chapter seven.

Chapter II
Dielectric Properties of Transformer Oil

Transformer oil is a mixture of hydrocarbons, with an undefined exact composition. Mineral transformer oil is derived from crude petroleum. The physical, chemical, and electrical properties of the transformer oil need to meet specific industrial standards to be used properly in the transformer. A large number of tests [9] are usually performed the oil samples extracted from an operating transformer. These test measure the various physical, electrical and chemical properties which are significant in determining the state of the insulating oil, and of the transformer.

To be cost effective, an on-line monitoring system has to be selective in the properties it monitors. One of the properties useful to observe is increased conduction in the oil. The microdielectric sensor is designed for measuring the dielectric properties especially at very low frequencies. Measurements of loss and permittivity at frequencies ranging from .005 Hz to 10 kHz can be used in the on-line monitoring system. But, the usefulness of the sensor's low frequency capacity in deducing bulk properties remains to be determined.

Measurements of water and gas content in oil are more revealing indicators of a transformer condition than loss measurements. The microdielectric sensor is likely to be

tailored for measurements of water content in the oil, or dissolved gasses and other byproducts of degradation.

In this chapter, dielectric and loss phenomena in transformer oil are discussed as background for the experimental analysis. Literature which correlates various aging phenomena with increase of loss of transformer oil is reviewed. The significance of water content is also discussed due to the observed sensitivity of the sensors to humidity. Two aspects of water content in transformer oil are discussed: the effect of water on the dielectric properties of oil, and the relation between water content in oil and the general status of the transformer.

2.1 Dielectric and Loss Phenomena in Transformer Oil

The dielectric behavior of insulating liquids in general is not well understood, and is still a research topic. Losses in insulating liquids like transformer oil are generally attributed to three basic mechanisms, namely ionic conduction, dipole orientation, and space charge polarization [10] [11] . Because ionic space charge can link the motion of ions to the convection of the liquid, there is also a complex electrohydrodynamic phenomena involved. The mechanical-to-electrical half of this interaction will be evident in our measurements demonstrating the effect of turbulent mixing on the diffuse double layer existing between an electrode and the oil.

The loss due to dipole orientation is caused by the

viscous rotation of dipoles subject to thermal disorientation in response to an alternating field. For a single relaxation time Debye model [12] , often represented by a complex dielectric constant, the loss (i.e. imaginary part of the dielectric constant) ε''_r is:

$$\varepsilon''_r = \frac{\varepsilon'_0 - \varepsilon'_\infty}{1+(\omega\tau)^2} \, \omega\tau \tag{1}$$

where ε'_0 is the static permittivity, ε'_∞ is the high frequency permittivity (equivalently the permittivity of free space ε_0 multiplied by the square of the index of refraction of the oil n^2), and τ is the dipole relaxation time constant. The permittivity corresponding to a Debye relaxation (i.e. the real part of the complex dielectric constant) is given by the following equation.

$$\varepsilon'_r = \varepsilon'_\infty + \frac{\varepsilon'_0 - \varepsilon'_\infty}{1+(\omega\tau)^2} \tag{2}$$

The tangent of loss caused by this mechanism is

$$\tan\delta_r = \frac{\varepsilon'_0 - \varepsilon'_\infty}{\varepsilon'_0 + \varepsilon'_\infty(\omega\tau)^2} \, \omega\tau \tag{3}$$

This function has a peak around the frequency ω_0 as given by

$$\omega_0 = \frac{1}{\tau} \, (\frac{\varepsilon'_0}{\varepsilon'_\infty})^{\frac{1}{2}} \tag{4}$$

The existence of many types of dipoles cause the response to

deviate from the ideal Debye model, but the general behavior of dipole orientation remains similar to that of a single relaxation time model. The dipole relaxation time constant increases linearly with the viscosity of the oil, and thus is a strong function of temperature [11]. For transformer oil at room temperature the frequency of maximum loss is on the order of 10^7 Hz. If the dipole relaxation time constant is assumed to be [12] [13]

$$\tau = \frac{4\pi \eta \ a_d^3}{kT} \tag{5}$$

where η is the viscosity of the liquid, k Boltzman's constant, T the temperature, and a_d is the radius of dipoles, then the size of the dipoles is on the order of few Angstroms.

The dipole orientation loss is sensitive to degradation. Hakim [13] shows that after oxidation of oil, ω_o decrease, which suggests an increase in the size of the rotating dipoles. He suggests that with oxidation, a hydrogen bond develops between the dipole and its surroundings. At high frequencies (on the order of 10^7 Hz) where losses due to ion conduction are insignificant, dipole orientation is the dominant factor.

The ionized species causing ion migration are believed to be ion-clusters or molecular aggregates in which ions are surrounded by other molecules. Ion conduction loss is related to conductivity by:

$$\epsilon_c'' = \frac{\sigma}{\omega} \tag{6}$$

where ϵ_c'' is the loss due to ionic conduction, σ is the conductivity of the oil, and ω is the angular frequency of excitation.

The ion migration loss is highly dependent on the concentration of impurities within the oil. Impurities introduced to the oil produce higher ionic conduction [14]. The natural contaminants in transformer oil cause ionic losses similar to those obtained by adding artificial impurities. Hydrogen ions are proposed by Hakim [12] as additional charge carriers in transformer oil, and he suggests that oxidation causes an increase of their concentration due to the formation of acids.

Values of ionic conductivity in transformer oil are typically less than 10^{-12} mho/m. The conductivity assuming a concentration of ions n, with an average mobility b and charge q is

$$\sigma = nqb \tag{7}$$

Typical values for the mobility of ions in transformer oil at room temperature are on the order of $10^{-9} \frac{m^2}{V\text{-}sec}$ [13]. Assuming that the ions carry a single electronic charge, the concentration of ions based on the mentioned value of mobility is on the order of $10^{16} m^{-3}$ at room temperature. Assuming that the mobility of ions is given by Stoke's

equation [14] [15]

$$b = \frac{q}{6\pi\eta a_i} \tag{8}$$

where a_i is the radius of the ion, an oil with a viscosity of $5 \times 10^{-2} \frac{Kg-sec}{m^2}$ and a carrier mobility of 10^{-9} should have ions with a radius on the order of few Angstroms.

Ion migration and dipole orientation are both bulk phenomena. The third type of dielectric phenomena in insulating liquids, namely space charge polarization, is an interface phenomena. In homogeneous liquids, the interfaces occur between the liquid and the solid electrodes or insulation, and space charge orientation is a strictly surface phenomena.

The effect of space charge accumulation near the electrodes (i.e. the electrical double layer) has been investigated thoroughly in electrolytes [16] . Space charge in dielectric solids and liquids creates a similar electrode polarization effect. Studies on dielectric solids at very low frequencies show an increased capacitance attributed to space charge accumulation [17].

Interfaces of solids with dielectric liquids show evidence of space charge effects demonstrated by an increase of the capacitance of the structure and the departure of loss from the ionic $\frac{1}{\omega}$ dependence. Commercial paper capacitors impregnated with mineral oil show an increase of measured capacitance at low frequencies [18]. Thin films of

23

mineral oils [19] and other insulating fluids [20] show a clear space charge effect, with stronger influences with increasing temperature or decreasing layer thickness.

Solid/liquid interfaces have two aspects, accumulation of ions at the interface as space charge, or an adsorption/absorption process at the interface [21] [22]. An adsorbed layer can create a conducting surface at the interface. Such a surface conducting layer will have an effect if an electric field is applied parallel to the interface.

2.2 Effect of Transformer Oil Aging on its Loss

Several studies have investigated the change of conduction and dielectric properties of transformer oil due to degradation. A study by EPRI [23] reveals no apparent increase of loss in transformer oil samples degraded by accelerated aging in transformers operating under overload conditions. A study by El-Sulaiman et al. [24] shows an increase in the high field dc conduction of an aged oil sample. However, no molecular changes in the oil were detected using various spectroscopy techniques, which indicates that the deterioration was caused by impurities rather than a change in composition. Crine et al. [25] examined samples of oil obtained from transformers which have been in service for various lengths of time. Their study shows a tendency of increase of loss with the age of transformer, but the values for samples of similar age were

scattered over two orders of magnitude. The effect of thermal aging on transformer oil was investigated by Cesar [26], and an increase of loss with aging was detected.

The loss in most studies is measured at 60 Hz. Lower frequency measurements of the loss are likely to be more effective in determining transformer oil condition. At low frequencies the loss is larger and thus less sensitive to noise.

2.3 Moisture in Transformers

Moisture can leak into transformers through gaskets, or be generated internally by degradation of the cellulose insulation. Being the major cause of deterioration of the insulation of a transformer, moisture distribution in transformers has been investigated in recent studies [27] [28].

Water dissolved in transformer oil increases its conductivity. Guizonnier [29] indicates that water forms ionization centers injecting conduction ions throughout the fluid. Furthermore, the dissolved water reduces the dielectric strength of transformer oil. Another important factor in deterioration due to moisture is the increase of losses in the paper insulation. Due to the difficulty of a direct measurement of water content in the paper insulation, water content in the oil can be used as an indication of it [30].

Water content in oil is currently determined by drawing

samples from the transformer, and analyzing them [31] [32].
Selectively coated sensors could provide an on-line
measurement of water in the transformer oil. In addition,
moisture sensitive sensors could be covered by samples of
the cellulose insulation and used as a direct indication of
the amount of water held by the paper insulation.

Chapter III

Field Solution Using a Transfer Relation Approach

Due to the complexity of the solid/liquid interface between the sensor and the surrounding transformer oil, a general flexible approach is needed to account for surface phenomena. In this chapter an approach based on transfer relations is used to find the field solution for the sensor's geometry. The approach described here is generally applicable to piece-wise and smoothly inhomogeneous media interfaced by the microdielectrometer. This includes diffuse double layer, adsorbed surface layer, ions injected into solid coatings, and other inhomogeneities of interest.

The field solution developed here is used in chapter four to calculate the equivalent circuit parameters of the sensor, and thus predict the sensor's response with an arbitrary load.

An analytical limit is provided to check the validity of the numerical approach. Solution for a coated sensor, which might prove necessary if the sensor is going to be coated with special materials to sensitize it to specific gasses or other byproducts of degradation, is outlined.

3.1 Geometry of Sensors

The sensor consists of an interdigitated set of aluminium electrodes, separated from a ground substrate by a layer of silicon dioxide with a thickness h as shown in

figure 3.1. The fluid whose properties are to be measured (i.e. transformer oil in this case) is assumed to extend from the sensor's surface to infinity. The width of each electrode and the separation between two consecutive electrodes is w. The total period of the structure is $\lambda=4w$. The periodic structure is assumed to extend to infinity on both sides of the x axis. The silicon dioxide has no conductivity and has the permittivity ϵ_{ox}. The interface between the silicon dioxide and the fluid has a surface conductivity σ_s and a surface dielectric constant ϵ_s. The fluid above the sensor has a conductivity σ_ℓ and a permittivity ϵ_ℓ. At the interface the two surfaces just below and just above the interface are labeled "a" and "b" respectively.

3.2 Boundary Conditions

The driven electrode is at an alternating potential with amplitude $V_\emptyset$ and frequency ω, and the floating electrode is assumed to be grounded[*] . The boundary conditions are:

1) At y=$\emptyset$ the potential is zero.

2) At y=∞ the electric field goes to zero.

3) The potential is continuous at y=h (i.e. at the interface between the sensor and the fluid).

---

[*]Since the electrodes represent a linear system, the equivalent circuit obtained from the field solution with a grounded floating gate can be used to predict the response for any other load.

28
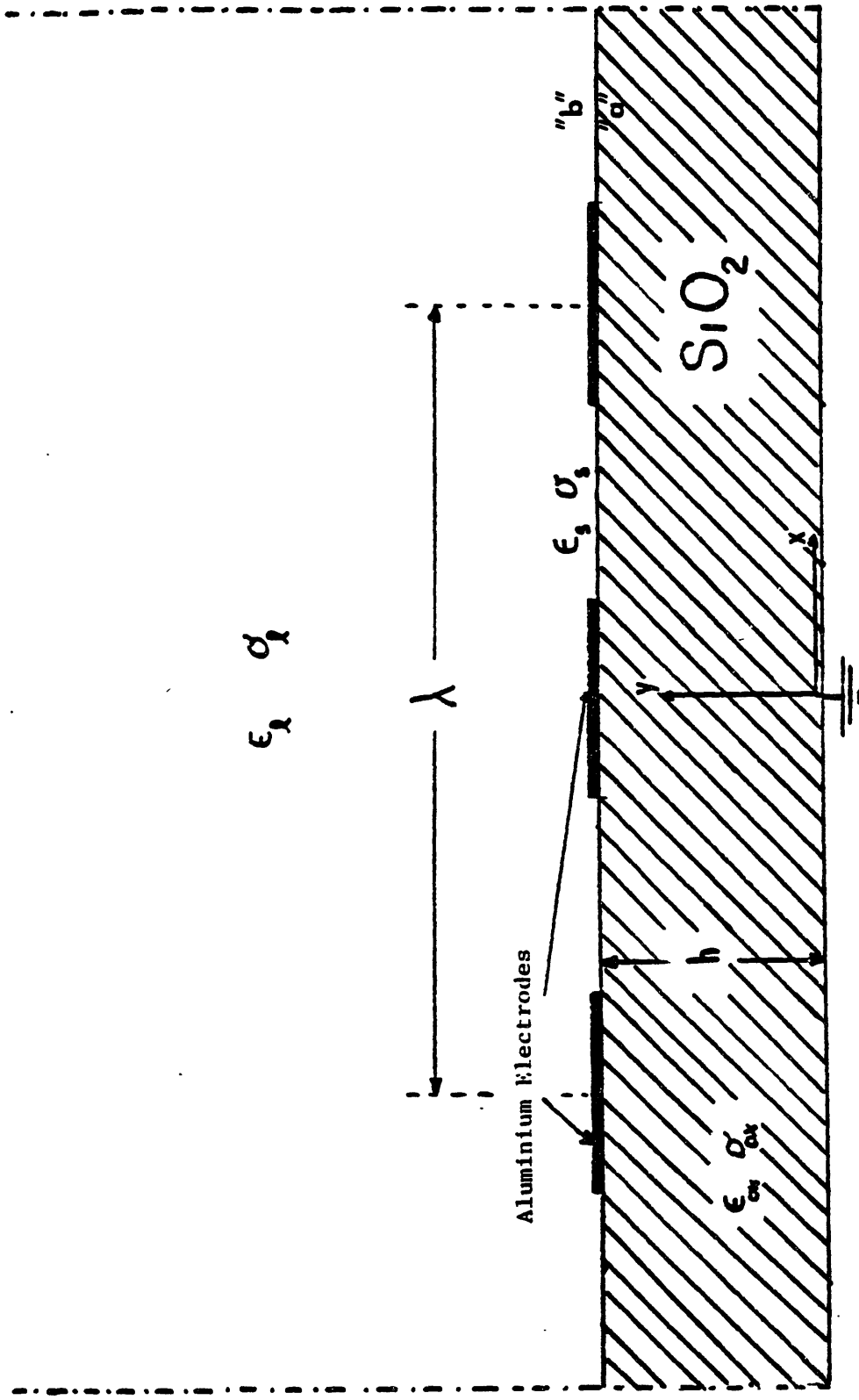
Figure 3.1
Schematic cross section
of a sensor

4) At y=h the potential is constrained at the electrodes region, while charge is constrained to satisfy conservation of charge at the silicon oxide region.

The fourth boundary condition represents a mixed boundary. The constrained potential at the electrodes implies:

$$\Phi^a(x)=V_\emptyset \qquad \text{for } -\frac{\lambda}{8} < x < \frac{\lambda}{8}$$

$$\Phi^a(x)=\emptyset \qquad \text{for } |\frac{3\lambda}{8}|<|x|<|\frac{\lambda}{2}| \qquad (9)$$

The surface charge at the silicon dioxide/fluid interface σ_f is:

$$\sigma_f=\epsilon_\ell E_y^b(x)-\epsilon_{ox}E_y^a(x)+\frac{\partial \epsilon_s E_x^a}{\partial x} \qquad \text{for } |\frac{\lambda}{8}| < |x| < |\frac{3\lambda}{8}| \qquad (10)$$

Including $\frac{\partial \epsilon_s E_x^a}{\partial x}$ in the surface charge implies that surface dipoles can polarize in the x direction[*], creating surface charges. By conserving the surface charge at the interface we get:

$$\frac{\partial \sigma_f}{\partial t} +(J_y^b-J_y^a)+ \frac{\partial K_s}{\partial x} =\emptyset \qquad \text{for } |\frac{\lambda}{8}| < |x| < |\frac{3\lambda}{8}| \qquad (11)$$

The surface current K_s and the normal current densities J_y^a and J_y^b are:

---

[*]This term is negligible in the case of the transformer oil/sensor interface.

$$J_y^a(x)=\emptyset \tag{12}$$

$$J_y^b(x)=\sigma_\ell E_y^b(x) \tag{13}$$

$$K_s(x)=\sigma_s E_x^a(x) \tag{14}$$

Substituting the above equations into equation (10), and assuming steady state and uniform surface properties (i.e. ϵ_s & σ_s are both independent of x), we get the boundary condition for charge conservation at the fluid/silicon dioxide interface.

$$j\omega \left(\ \epsilon_\ell E_y^b(x)-\epsilon_{ox}E_y^a(x)\ \right) +\sigma_\ell E_y^b(x)+ (\sigma_s+j\omega\epsilon_s)\frac{\partial E_x^a(x)}{\partial x} = \emptyset$$
$$\text{for } |\frac{\lambda}{8}| < |x| < |\frac{3\lambda}{8}| \tag{15}$$

Normalizing as follows:

$$\underline{\epsilon}_\ell = \frac{\epsilon_\ell}{\epsilon_{ox}} \ , \ \underline{\epsilon}_s = \frac{\epsilon_s}{\lambda\epsilon_{ox}}$$
$$\underline{\sigma}_\ell = \frac{\sigma_\ell}{\omega\epsilon_{ox}} \ , \ \underline{\sigma}_s = \frac{\sigma_s}{\omega\lambda\epsilon_{ox}}$$
$$\underline{x} = \frac{x}{\lambda}$$

We can write the normalized form of equation (15)

$$(\epsilon_\ell-j\sigma_\ell)E_y^b(x)-E_y^a(x)+(\epsilon_s-j\sigma_s)\frac{\partial E_x^a(x)}{\partial x} = \emptyset$$
$$\text{for } |\frac{1}{8}| < |x| < |\frac{3}{8}| \tag{16}*$$

---

*Underlined equation numbers indicate a normalized equation.

The solution for the field has to satisfy these boundary conditions in addition to satisfying a bulk equation (Laplace's if space charge is assumed to be zero).

3.3 A Transfer Relation Approach for Solving the Mixed Boundary Value Problem

The method used in solving for the field satisfying the boundary conditions given in section 3.2 is based on a Fourier representation of the solution. The potential at $y=h$ and the normal electric field at surfaces "a" and "b" can be written in terms of their Fourier components.

$$\phi^a(x) = \phi^b(x) = \sum_0^\infty \tilde{\phi}^a(n) \cos(\frac{2\pi n x}{\lambda})$$

$$E_y^a(x) = \sum_0^\infty \tilde{E}_y^a(n) \cos(\frac{2\pi n x}{\lambda})$$

$$E_y^b(x) = \sum_0^\infty \tilde{E}_y^b(n) \cos(\frac{2\pi n x}{\lambda}) \tag{17}$$

If the potential at the sensor-liquid interface $\phi^a(x)$ were known, then $\tilde{\phi}^a(n)$ can be found using the Fourier series relation.

$$\tilde{\phi}^a(n) = \frac{2}{\lambda} \int_0^\lambda \phi^a(x) \cos(\frac{2\pi n x}{\lambda}) \, dx \qquad \text{for } n \neq 0$$

$$\tilde{\phi}^a(0) = \frac{1}{\lambda} \int_0^\lambda \phi^a(x) \, dx \tag{18}$$

However, the potential at the interface is known at the electrodes only. At the surface between the two electrodes the potential assumes the appropriate functional dependence

32

in order to satisfy conservation of charge as expressed by equation (16). The interface potential can be approximated by linear segments with values chosen to satisfy conservation of charge.

The potential is assigned to unknown values, V_j, at k different collocation points along the silicon dioxide/fluid interface as shown in figure 3.2. The potential is symmetric with respect to the y axis because of the symmetry in the geometry of the sensor. The first collocation point which is assigned the potential V_1 is $\frac{\lambda}{8k}$ away from the edge of the driven electrode. All other collocation points are separated by $\frac{\lambda}{4k}$ intervals, which leaves the last point with the potential V_k at a distance $\frac{\lambda}{8k}$ away from the edge of the floating electrode. So each potential V_j corresponds to the collocation point $x_j = \pm \frac{\lambda}{8k}(k+2j-1)$ along the interface. Using equation (18) we can find the Fourier coefficients $\tilde{\phi}^a(n)$ in terms of the assigned voltages V_j.

$$\tilde{\phi}^a(\emptyset) = V_\emptyset \left(\frac{1}{4} + \frac{1}{8k}\right) + \frac{3}{8k}(V_1 + V_k) + \frac{1}{2k} \Sigma_2^{k-1} V_j$$

$$\begin{aligned}
\tilde{\phi}^a(n) = \frac{4k}{n^2\pi^2} \Big\{ & V_\emptyset \left(2\cos\left(\frac{n\pi}{4}\right) - 2\cos\left(\frac{n\pi}{4k}(k+1)\right)\right) \\
& + V_1\left(3\cos\left(\frac{n\pi}{4k}(k+1)\right) - \cos\left(\frac{n\pi}{4k}(k+3)\right) - 2\cos\left(\frac{n\pi}{4}\right)\right) \\
& + \Sigma_2^{k-1} V_j\left(2\cos\left(\frac{n\pi}{4k}(k+2j-1)\right) - \cos\left(\frac{n\pi}{4k}(k+2j+1)\right)\right. \\
& \left. - \cos\left(\frac{n\pi}{4k}(k+2j-3)\right)\right) \\
& + V_k\left(3\cos\left(\frac{n\pi}{4k}(3k-1)\right) - \cos\left(\frac{n\pi}{4k}(3k-3)\right) - 2\cos\left(\frac{3n\pi}{4}\right)\right) \Big\}
\end{aligned}$$

$$\text{for } n \neq \emptyset \tag{19}$$

Assuming that there is neither space charge in the fluid nor

33
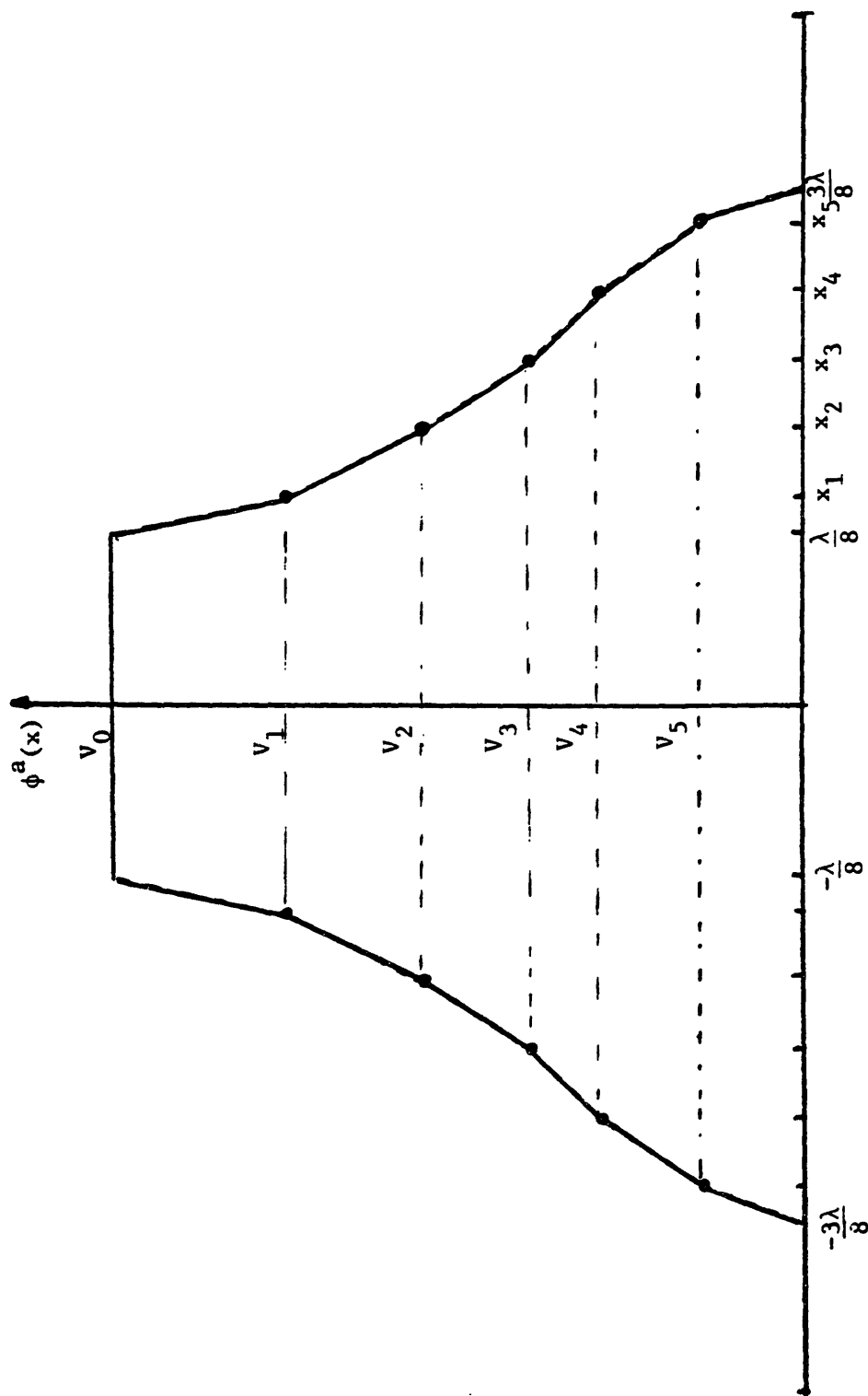
Figure 3.2

The potential at the interface

in the silicon dioxide, and that each region is one of uniform permittivity and conductivity, the potential satisfies Laplace's equation. Relating the normal electric field at surfaces "a" and "b" to the potential at the interface for each of the Fourier components using transfer relations [33] we get:

$$\tilde{E}_y^a(n) = - \frac{2\pi n}{\lambda} \coth(\frac{2\pi n h}{\lambda}) \; \tilde{\phi}^a(n) \qquad \text{for } n \neq 0$$

$$\tilde{E}_y^a(0) = - \frac{\tilde{\phi}^a(0)}{h}$$

$$\tilde{E}_y^b(n) = \frac{2\pi n}{\lambda} \; \tilde{\phi}^a(n) \qquad\qquad\qquad (20)$$

By differentiating the potential at the interface with respect to x we get the tangential electric field at the interface.

$$E_x^a(x) = - \frac{\partial \phi^a(x)}{\partial x} \qquad\qquad\qquad (21)$$

The assumed tangential electric field for the interface potential is shown in figure 3.3 (corresponding to k=5). The tangential field can be related to the unknown V_j in a simple manner. For each segment on the interface $E_x^a = - \frac{\Delta V}{\Delta x}$, yielding the following relations:

$$E_x(x) = \frac{4k}{\lambda}(V_j - V_{j+1}) \qquad \text{for } x_j < x < x_{j+1} \; \& \; 0 < j < k$$

$$E_x(x) = \frac{8k}{\lambda}(V_0 - V_1) \qquad \text{for } \frac{\lambda}{8} =< x < x_1$$

35
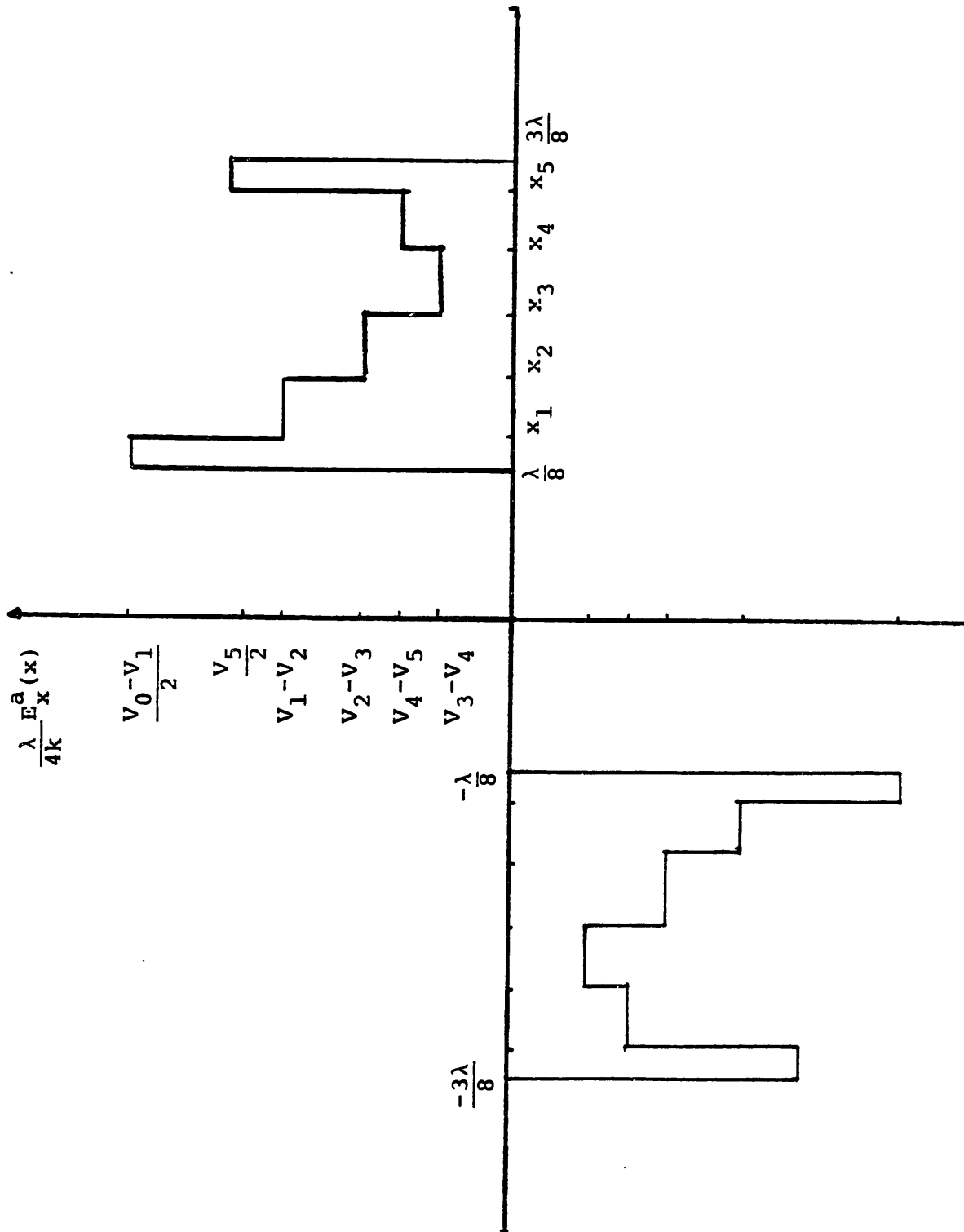
Figure 3.3

The tangential electric field at the interface.

36

$$E_x(x) = \frac{8k}{\lambda} V_k \qquad\qquad \text{for } x_k < x =< \frac{3\lambda}{8} \qquad (22)$$

The tangential field is antisymmetric with respect to the y axis, and thus only the field on the positive side of the x axis is appropriately represented by the above relations.

With a finite number of collocation points at the interface, conservation of charge can not be satisfied at every value of x along the interface as required by equation (16). An approximation can be obtained by dividing the interface into k intervals, and satisfying conservation of charge within every interval. As figure 3.4 demonstrates, this amounts to integrating equation (11) between the two end points x_i and x_{i+1} and setting the value of the integral to zero.

$$K_s(x_{i+1}) - K_s(x_i) + \int_{x_i}^{x_{i+1}} \left(\frac{\partial \sigma_f}{\partial t} + (J_y^b - J_y^a) \right) = 0 \qquad (23)$$

The points x_i are chosen at the edges of the electrodes and at mid intervals between two consecutive collocation points x_j and x_{j+1}. So the distance between $\frac{\lambda}{8}$ and $\frac{3\lambda}{8}$ is divided into k segments stretching $\pm \frac{\lambda}{8k}$ around each collocation point. By this choice of x_i the points along the interface at which the tangential field is not well defined are in the middle of each segment, so that any numerical error they introduce is not more heavily weighted on one side of the segment than on the other. The only exceptions happen at the two segments bordering the edges of the electrodes, where

Figure 3.4

Conservation of charge in a segment along the interface.

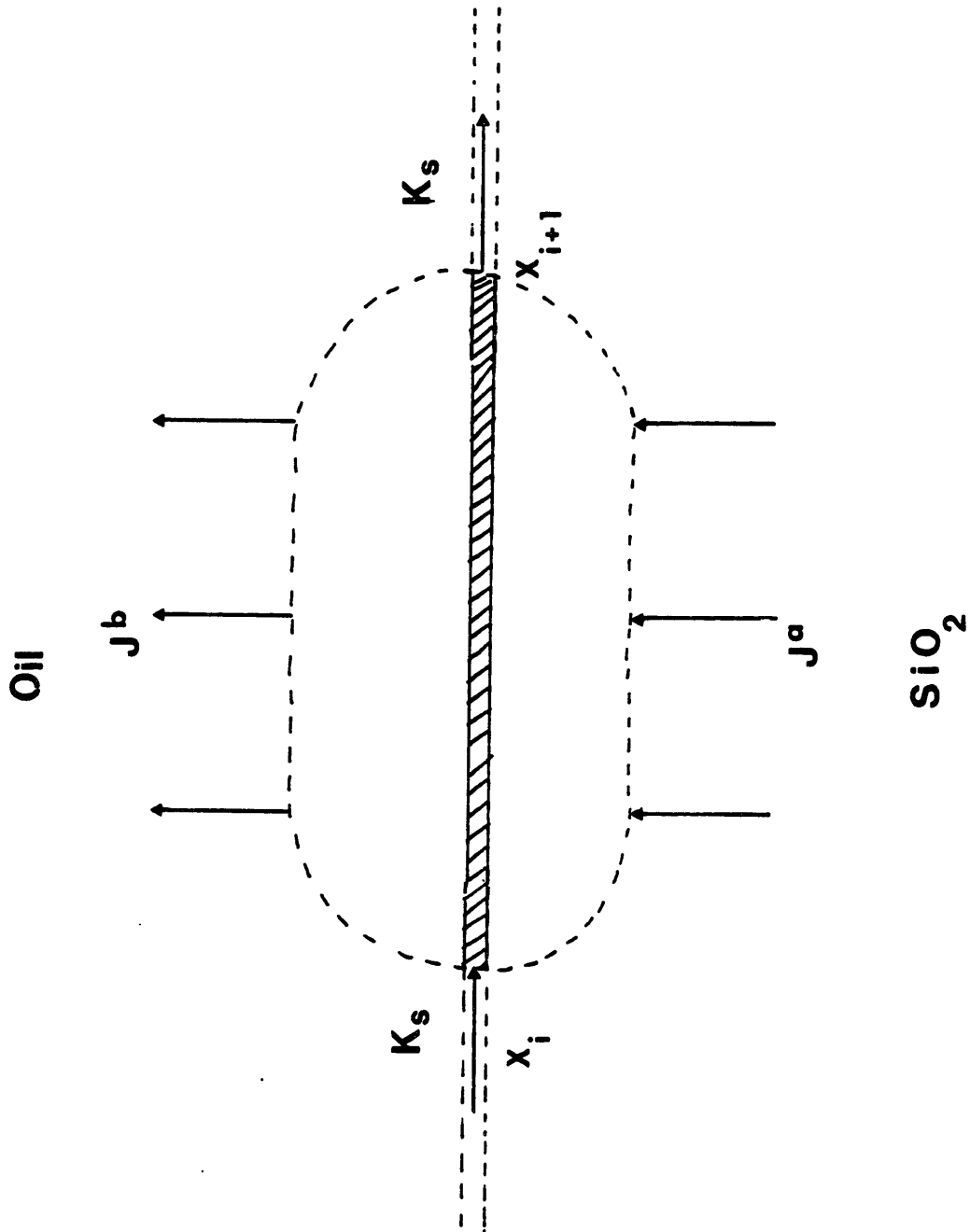the tangential field is discontinuous at the edge of segment
next to the electrode. It is possible to use an average at
the points of discontinuity, but it is closer to reality to
assume that the value of the field at the segment extends to
include the boundary points as expressed earlier by equation
(22). This distinction between discontinuities at the
electrode edges and other points of discontinuity along the
interface exists because in the first case a discontinuity
caused by the infinite but integrable surface charge at the
contact point appears even in an exact solution, while the
rest of the points of discontinuity are artifacts of the
linear approximation and would not appear if the solution
was exact.

Equation (16) is integrated along each segment j of the
interface between the two points $x_i = x_j - \frac{\lambda}{8k}$ and $x_{i+1} = x_j$
$+ \frac{\lambda}{8k}$ and the integral is set to zero as required by equation
(23). The resulting equation, which relates the tangential
electric field to the Fourier components of the normal
field, is:

$$(\epsilon_s - j\sigma_s) \left[E_x(x_j + \frac{\lambda}{8k}) - E_x(x_j - \frac{\lambda}{8k}) \right] + \frac{\lambda}{4k} \left\{ (\epsilon_\ell - j\sigma_\ell) \tilde{E}_y^b(0) - \tilde{E}_y^a(0) \right\}$$

$$+ \sum_1^\infty (\frac{\lambda}{2\pi n}) \left\{ (\epsilon_\ell - j\sigma_\ell) \tilde{E}_y^b(n) - \tilde{E}_y^a(n) \right\} \left\{ \sin(\frac{n\pi}{4k}(k+2j)) - \sin(\frac{n\pi}{4k}(k+2j-2)) \right\}$$

$$= 0 \qquad\qquad (24)$$

By combining equations (19) and (20) the Fourier components
of the normal field $\tilde{E}_y^a(n)$ and $\tilde{E}_y^b(n)$ can be expressed in
terms of the unknowns V_j as shown below:

$$\tilde{E}_y^a(0) = - \frac{1}{h} \left(V_0 \left(\frac{1}{4} + \frac{1}{8k}\right) + \frac{3}{8k}(V_1 + V_k) + \frac{1}{2k} \right\}$$

$$\tilde{E}_y^a(n) = - \frac{8k}{n\pi\lambda} \coth\left(\frac{2\pi nh}{\lambda}\right) \left(V_0\left(2\cos\left(\frac{n\pi}{4}\right) - 2\cos\left(\frac{n\pi}{4k}(k+1)\right)\right)\right.$$

$$+ V_1\left(3\cos\left(\frac{n\pi}{4k}(k+1)\right) - \cos\left(\frac{n\pi}{4k}(k+3)\right) - 2\cos\left(\frac{n\pi}{4}\right)\right)$$

$$+ \sum_2^{k-1} V_j \left(2\cos\left(\frac{n\pi}{4k}(k+2j-1)\right) - \cos\left(\frac{n\pi}{4k}(k+2j+1)\right)\right.$$

$$\left. - \cos\left(\frac{n\pi}{4k}(k+2j-3)\right)\right)$$

$$+ V_k\left(3\cos\left(\frac{n\pi}{4k}(3k-1)\right) - \cos\left(\frac{n\pi}{4k}(3k-3)\right) - 2\cos\left(\frac{3n\pi}{4}\right)\right) \right\}$$

<div align="center">for n ≠ 0</div>

$$\tilde{E}_y^b(0) = 0$$

$$\tilde{E}_y^b(n) = \frac{8k}{n\pi\lambda} \left(V_0\left(2\cos\left(\frac{n\pi}{4}\right) - 2\cos\left(\frac{n\pi}{4k}(k+1)\right)\right)\right.$$

$$+ V_1\left(3\cos\left(\frac{n\pi}{4k}(k+1)\right) - \cos\left(\frac{n\pi}{4k}(k+3)\right) - 2\cos\left(\frac{n\pi}{4}\right)\right)$$

$$+ \sum_2^{k-1} V_j \left(2\cos\left(\frac{n\pi}{4k}(k+2j-1)\right) - \cos\left(\frac{n\pi}{4k}(k+2j+1)\right)\right.$$

$$\left. - \cos\left(\frac{n\pi}{4k}(k+2j-3)\right)\right)$$

$$+ V_k\left(3\cos\left(\frac{n\pi}{4k}(3k-1)\right) - \cos\left(\frac{n\pi}{4k}(3k-3)\right) - 2\cos\left(\frac{3n\pi}{4}\right)\right) \right\}$$

<div align="center">for n ≠ 0   (25)</div>

Substituting for $\tilde{E}_y(n)$ and $E_x(x)$ from equations (25) and (20) into equation (24), and evaluating for each segment on the interface we get a matrix of the form $\bar{\bar{A}} \cdot \bar{V} = \bar{X}$, where $\bar{V}$ is the vector of unknowns V_j. Details of the coefficients of the matrix $\bar{\bar{A}}$ and the vector $\bar{X}$ are given in Appendix A.

One of the issues concerning the numerical simulation is the number of collocation points to be placed along the interface, namely k. The steepest change in the field occurs at the edges, but when the conductivity of the medium above the sensor increases, the field becomes less steep and the solution converges with less points. Shown in figure 3.5 are

the successive approximations to the potential at the interface for a continuous medium, and $\frac{\lambda}{h} = 10$. For a medium with a higher conductivity the decay in the potential is more uniform as shown in figure 3.6. Also the thickness of the silicon dioxide layer influences the number of the terms that need to be used since the decay rate of the potential increases with increasing $\frac{\lambda}{h}$. In general the number of points to be used has to be larger than the minimum of $|\frac{\lambda}{h(\underline{\varepsilon}_s - j\underline{\sigma}_s)}|$ and $|\frac{\lambda}{h(\underline{\varepsilon}_\ell - j\underline{\sigma}_\ell)}|$.

3.4 The Long Wave Limit

In the limit where the separation between the two electrodes is much longer than the silicon dioxide thickness, the numerical solution reaches an analytical solution. When $\frac{h}{\lambda} \to 0$, the Fourier components of the normal field as given in equation (20) reach the following limits:

$$\tilde{E}_y^a(n) \to -\frac{\tilde{\phi}^a(n)}{h}$$

$$\tilde{E}_y^b(n) << \tilde{E}_y^a(n) \tag{26}$$

The above equation shows the legitimacy of using the quasi one dimensional approximation , namely

$$E_y^a(x) \simeq - \frac{\phi^a(x)}{h} \tag{27}$$

Assuming that $|\underline{\varepsilon}_\ell - j\underline{\sigma}_\ell|$ is not much larger than one, we can neglect the current on surface "b" compared to the current
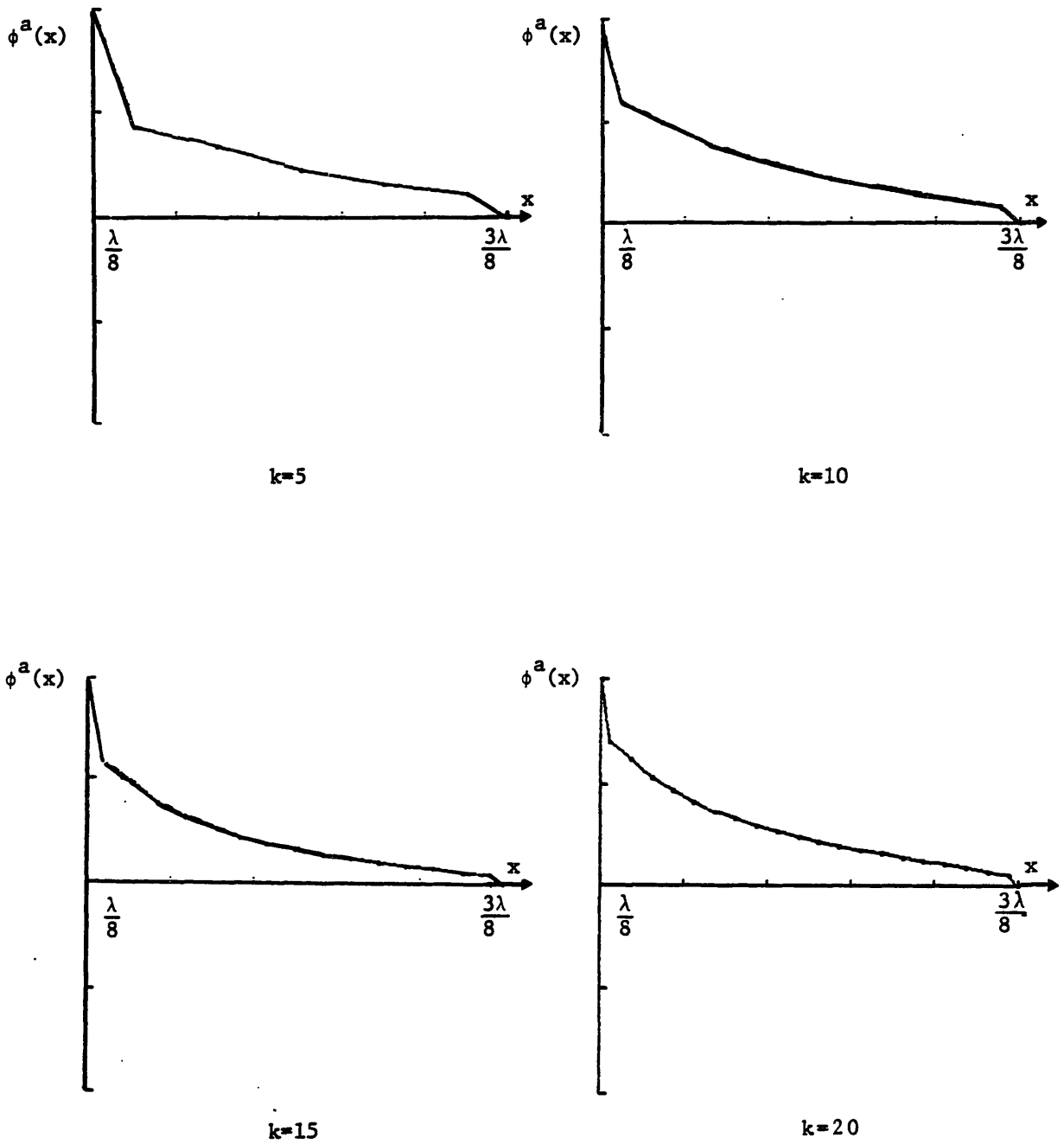
Figure 3.5

Successive approximation to the potential
at the interface
$$\frac{\lambda}{h} = 10 \ , \ \underline{\varepsilon}_\ell = 1 \ , \ \underline{\sigma}_\ell = 0 \ .$$
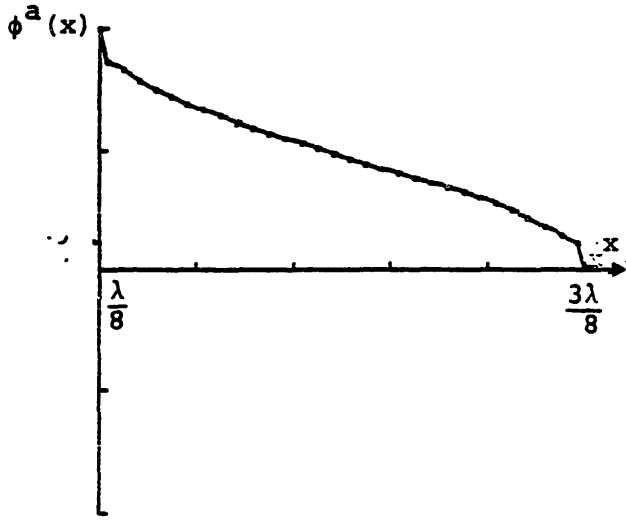
$\omega t = 0$
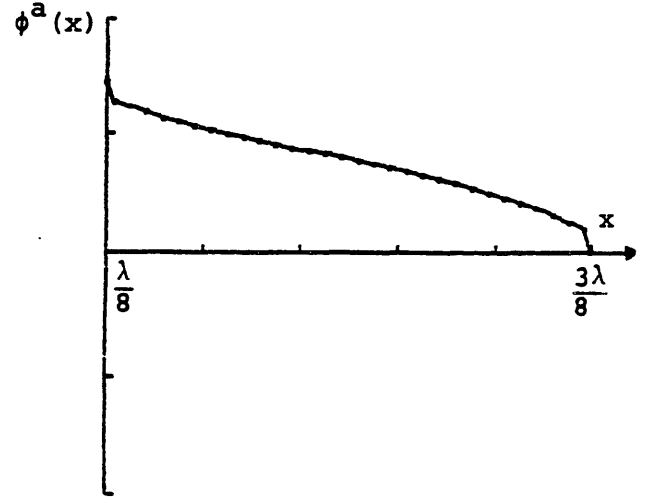
$\omega t = \dfrac{\Pi}{4}$
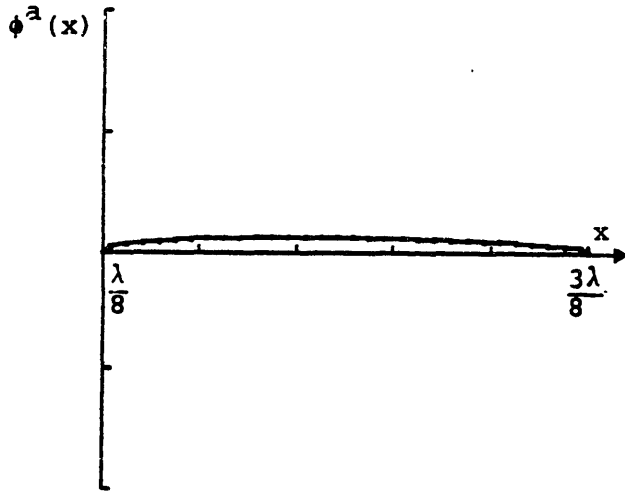
$\omega t = \dfrac{\Pi}{2}$
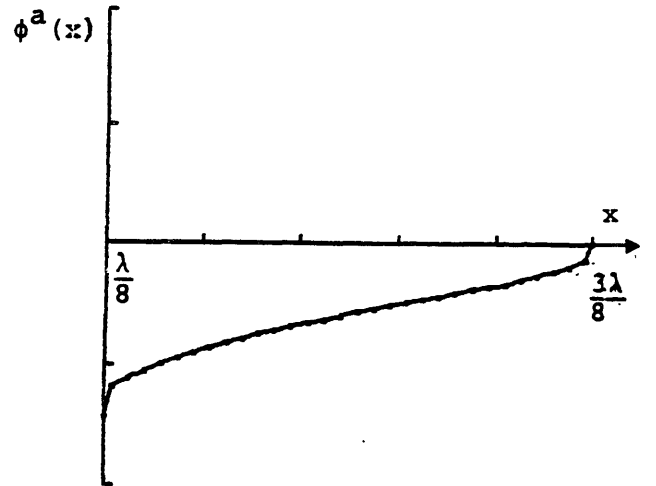
$\omega t = \dfrac{3\Pi}{4}$

Figure 3.6

Snapshots of the interface potential during a cycle.
$\dfrac{\lambda}{E} = 10$, $\underline{\varepsilon}_\ell = 1$, $\underline{\sigma}_\ell = 10$

on surface "a". Substituting for $E_y^a(x)$ and $E_x^a(x)$ in terms of $\phi^a(x)$ equation (16) becomes a second order linear differential equation.

$$\frac{d^2\phi^a(x)}{dx^2} = \frac{\lambda}{h(\varepsilon_s - j\sigma_s)} \phi^a(x) \tag{28}$$

Solving the above equation with the boundary conditions at the electrodes $\phi(\frac{1}{8}) = 1$ and $\phi(\frac{3}{8}) = 0$ we get a hyperbolic sine dependence for the interface potential.

$$\phi^a(x) = \frac{\sinh\alpha(\frac{3}{8} - x)}{\sinh\frac{\alpha}{4}} \tag{29}$$

Where α is defined by:

$$\alpha^2 = \frac{\lambda}{h(\underline{\varepsilon}_s - j\underline{\sigma}_s)}$$

This solution is equivalent to the transmission line model used by Garverick [6] to evaluate the surface impedance of a thin film on the sensor. The numerical solution obtained using the transfer relations approach for long wavelength geometry is in good agreement with the analytical solution as described by equation (29). Figure 3.7 shows the interface potential between the two electrodes for $\frac{\lambda}{h} = 40$ and the medium parameters $\underline{\varepsilon}_\ell = .1$, $\underline{\sigma}_\ell = 0$, $\underline{\varepsilon}_s = 0$, and $\underline{\sigma}_s = 1$ at four different moments during the first half of the excitation cycle. For a highly conducting surface $\alpha \to 0$, and the interface potential drops linearly between the two electrodes. The numerical solution predicts accurately this

44

Figure 3.7

Snapshots of the interface potential during a cycle.

$\frac{\lambda}{h} = 40$, $\underline{\varepsilon}_\ell = .1$, $\underline{\sigma}_\ell = 0$, $\underline{\varepsilon}_s = 0$, $\underline{\sigma}_s = 1$

limit.

3.5 Solution for a Two Layers Geometry and an Ambient Field
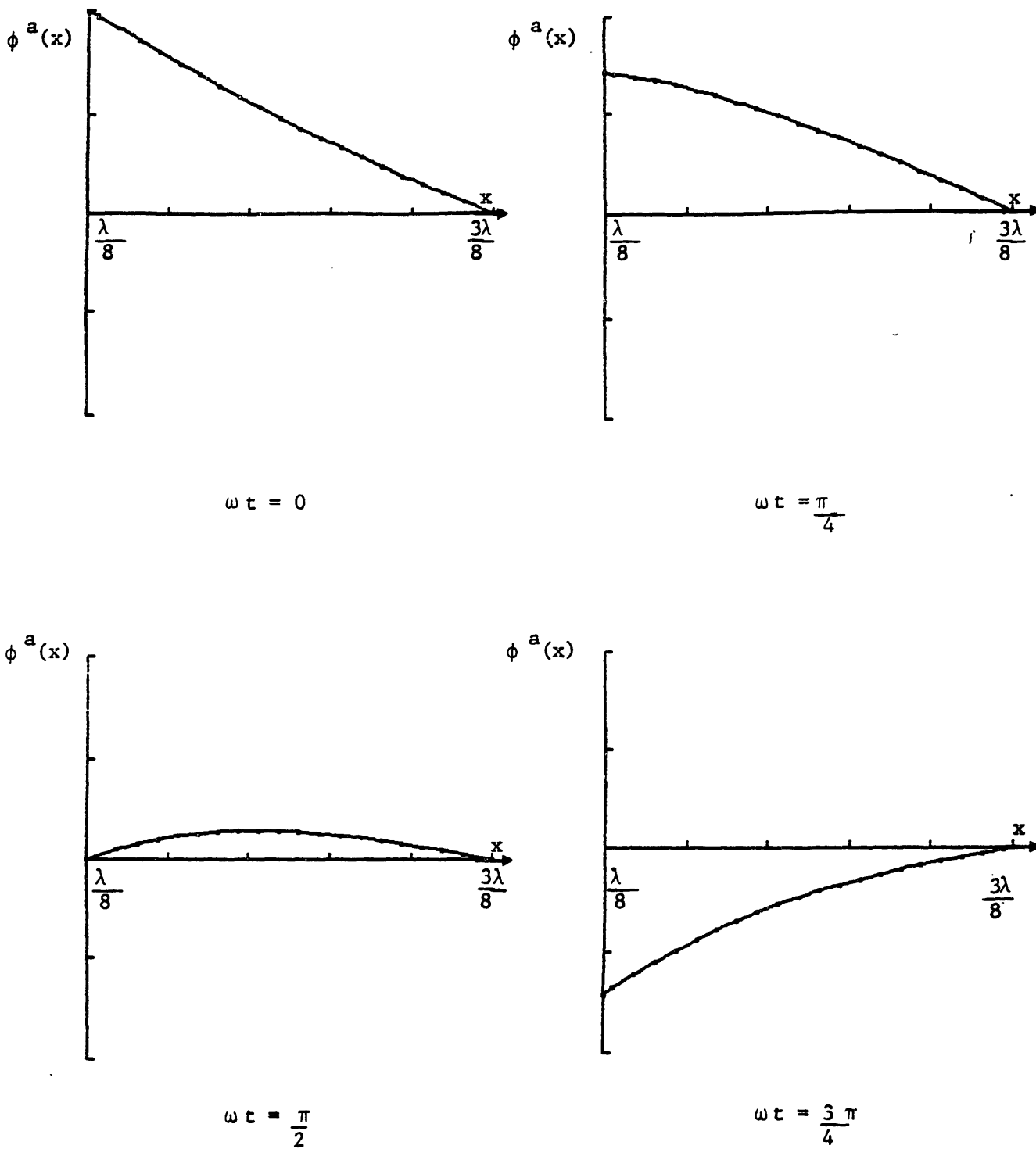
Changing the boundary conditions requires only a simple change in solving the problem. In this case we consider putting an additional layer on the sensors and an ambient electric field at infinity. The layer directly above the sensor (figure 3.8) has a thickness t, a conductivity $\sigma_{\ell 1}$ and a dielectric constant $\varepsilon_{\ell 1}$. The material above the coating layer extends to infinity and has a conductivity $\sigma_{\ell 2}$ and a dielectric constant $\varepsilon_{\ell 2}$. At infinity the electric field is constant (in space) and has frequency ω and an amplitude $E_{\emptyset}$. Using transfer relations, the Fourier components of the normal electric field at surfaces "a" and "b" can be related to $\tilde{\phi}^a(n)$ (see derivation in appendix B).

$$\tilde{E}_y^a(n) = - \frac{2\pi n}{\lambda} \coth(\frac{2\pi nh}{\lambda})\tilde{\phi}^a(n) \qquad n \neq \emptyset$$

$$\tilde{E}_y^a(\emptyset) = - \frac{\tilde{\phi}^a(\emptyset)}{h} \quad .$$

$$\tilde{E}_y^b(n) = \frac{2\pi n}{\lambda}\tilde{\phi}^a(n) \left[(\frac{-1}{\sinh\frac{2\pi nt}{\lambda}}) \frac{1}{\frac{\varepsilon_{\ell 2}-j\sigma_{\ell 2}}{\varepsilon_{\ell 1}-j\sigma_{\ell 1}}\sinh(\frac{2\pi nt}{\lambda})+\cosh(\frac{2\pi nt}{\lambda})} \right.$$

$$\left. +\coth(\frac{2\pi nt}{\lambda}) \right\} \qquad n \neq \emptyset$$

$$\tilde{E}_y^b(\emptyset) = \frac{\varepsilon_{\ell 2}-j\sigma_{\ell 2}}{\varepsilon_{\ell 1}-j\sigma_{\ell 1}} E_{\emptyset} \qquad\qquad (3\emptyset)$$

This equation is the equivalent of equation (2$\emptyset$) for the uniform medium. When the ambient field is zero and in the limit of t$\rightarrow\infty$ or $\varepsilon_{\ell 1}=\varepsilon_{\ell 2}$ and $\sigma_{\ell 1}=\sigma_{\ell 2}$ equation (3$\emptyset$) reduces to
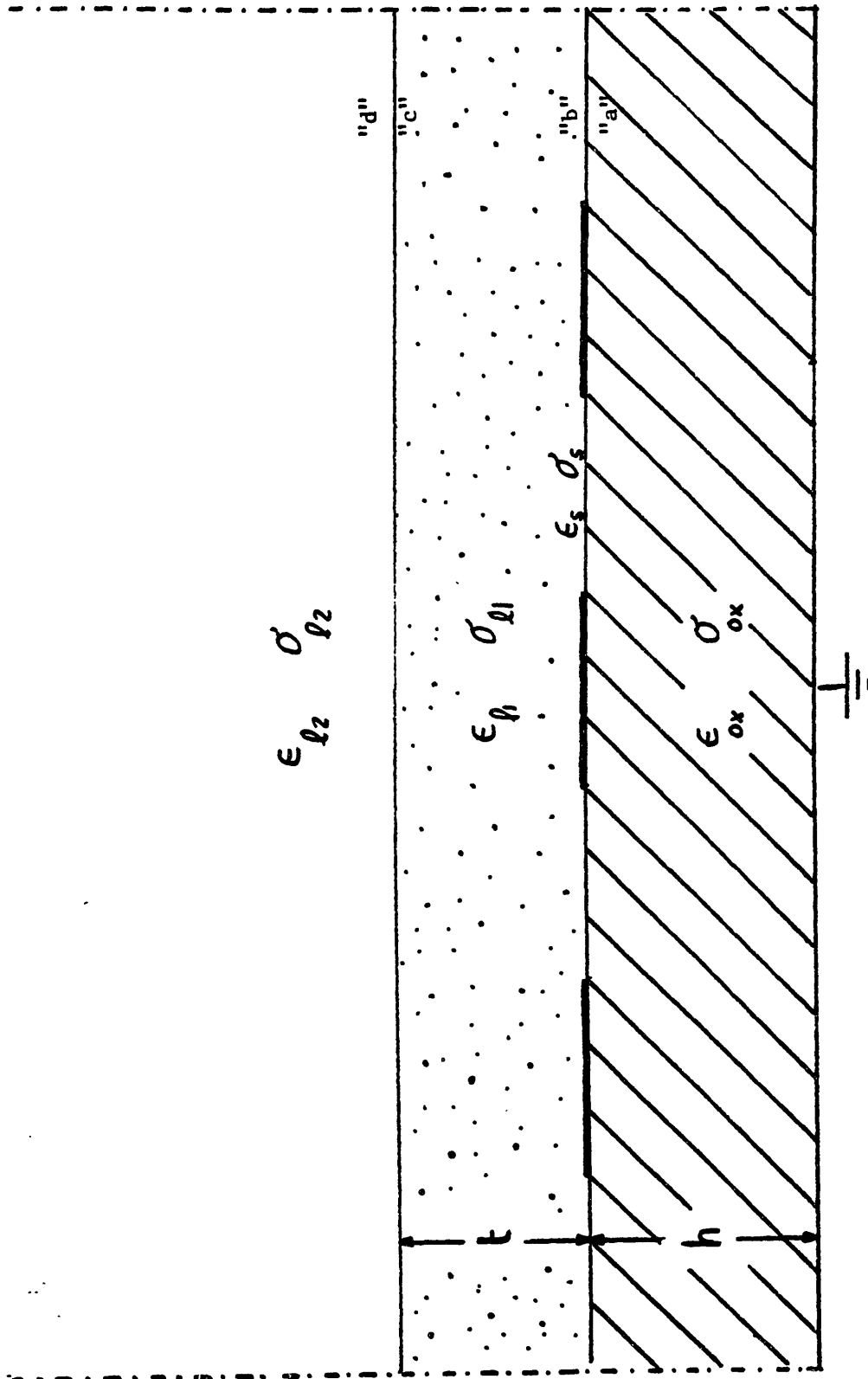
Figure 3.8

Geometry of a coated sensor

equation (2∅) because the medium becomes uniform. Again substituting for the normal and tangential fields in equation (16) we get the k equations necessary to solve for the k unknowns V_j.

This addition of a layer was pursued not only to demonstrate the generality of the approach, but also because of the possibility of coating the sensor with a material sensitive to the degradation of oil. The addition of an ambient electric field also might be necessary if the sensor is to be used near an applied electric field.

3.6 Generality of the Approach

The use of transfer relations can be applied to a general class of mixed boundary problems. The geometry of interdigital electrodes is used often for various applications, and this method is of direct application in such a geometry. This method can be equally useful for a medium with nonuniform properties or with the presence of space charge in the bulk. If space charge exists in the bulk, the transfer relations for a medium with space charge [34] can be used instead of equation (2∅). Other phenomena such as the convection of the space charge due to the fluid motion, or the formation of an electrical double layer at the interface can be accounted for once their appropriate transfer relations are used.

Other field problems with mixed boundaries appear frequently, and can be solved using this approach. For

example the simple Maxwell attenuator becomes a mixed boundary problem if the box is bent as shown in figure 3.9, and can be solved using this approach. Mixed boundaries appear frequently in electromechanical devices such as motors and generators, and can be approached using this method in combination with the appropriate transfer relations in polar coordinates [35].
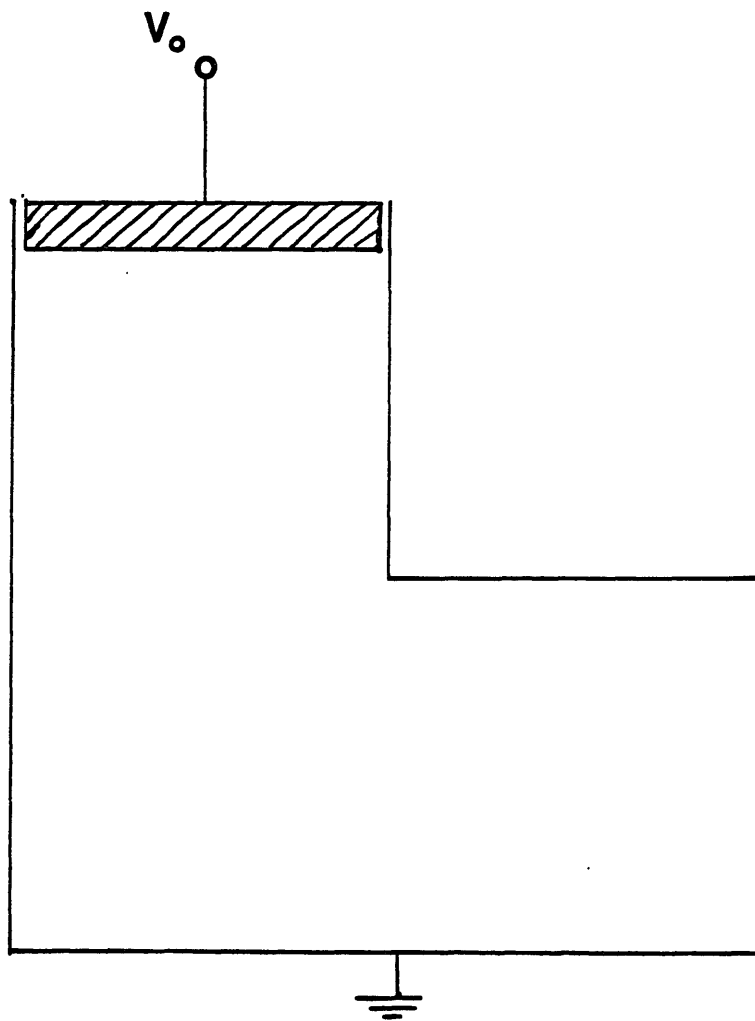
Figure 3.9

A bent Maxwell's attenuator, a mixed
boundary value problem.

Chapter IV

Gain and Phase Response Under Various Boundary Conditions

Since the response of the sensor is given as the ratio of the floating gate potential to the driven gate potential, the field solution obtained using the numerical method described in the previous chapter must be converted to the equivalent circuit parameters of the sensor. In this chapter the response of the sensor is calculated under various bulk and surface conditions. The effect of adding surface and contact impedance is discussed.

4.1 Frequency Variant Circuit Parameters

The response of the sensor is given as the ratio of floating gate potential to that of the driven gate. In terms of equivalent circuit parameters which are shown in figure 4.1 the ratio of the two voltages is:

$$\frac{V_f}{V_d} = \frac{Y_{12}}{Y_{11}+Y_{12}+Y_L} \tag{31}$$

where Y_L is the load on the driven gate, and Y_{12}, Y_{11} are the equivalent admittances of the sensor. Having solved for the field in the sensor for a specific set of parameters and a short circuit excitation (i.e. for $V_f=\emptyset$) the equivalent admittances Y_{11} and Y_{12} can be found. For a short circuit excitation the current to the driven and floating electrodes, respectively i_d and i_f are:
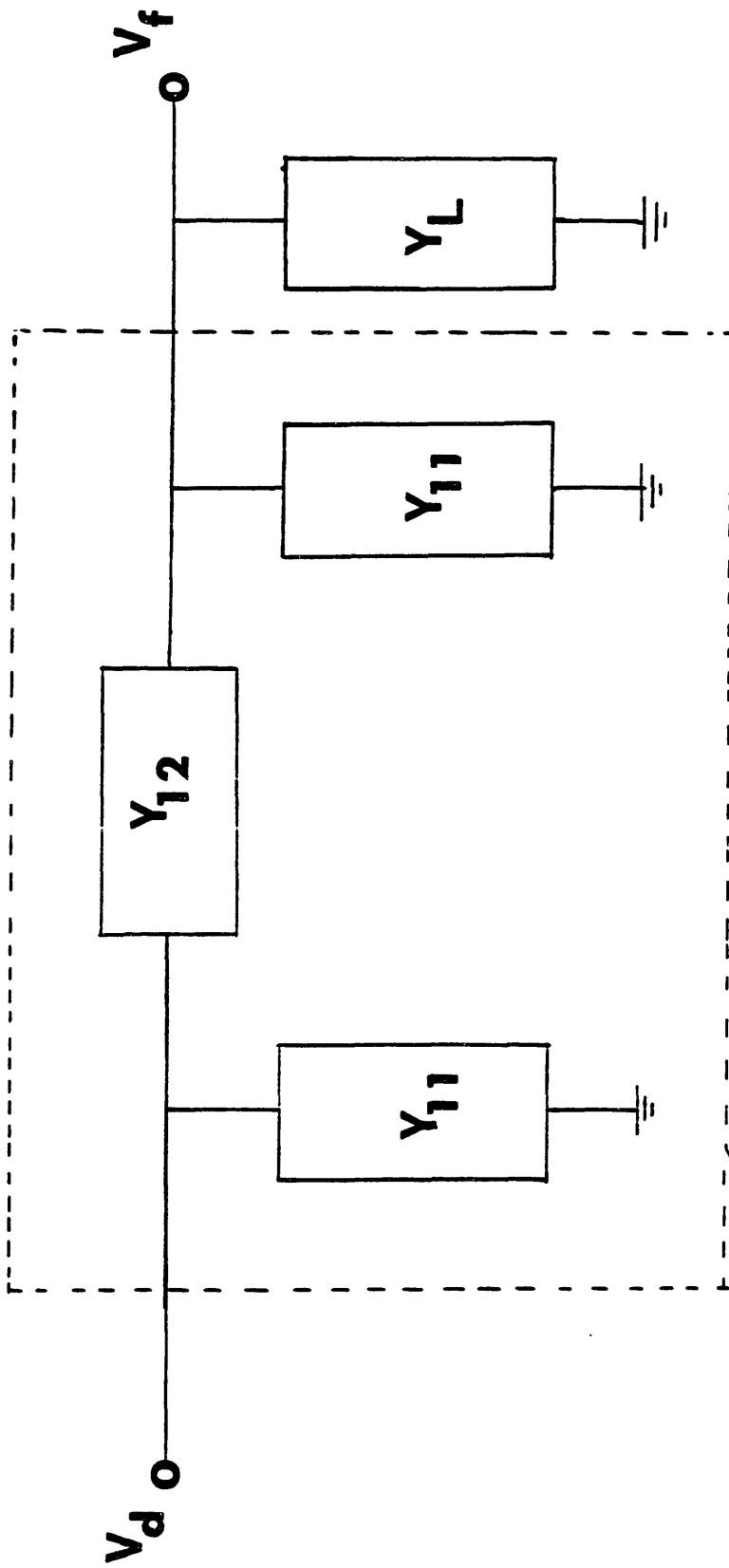
Figure 4.1

Equivalent circuit of sensor

$$i_d = (Y_{12} + Y_{11})V_o$$

$$i_f = -Y_{12}V_o \qquad (32)$$

The current to both the driven and floating gates is obtained by integrating the current around the electrode surface. Assuming that the number of repetitions of the periodic structure within the sensor is N and that the depth of the structure is d, then the current per unit length to each electrode is:

$$\frac{i_d}{Nd} = 2(\sigma_s + j\omega\epsilon_s)E_x^a(\frac{\lambda}{8}) + \int_{\frac{-\lambda}{8}}^{\frac{\lambda}{8}} \left[(j\omega\epsilon_\ell + \sigma_\ell)E_y^b(x) + j\omega\epsilon_{ox}E_y^a(x)\right]dx$$

$$\frac{i_f}{Nd} = 2(\sigma_s + j\omega\epsilon_s)E_x^a(\frac{5\lambda}{8}) + \int_{\frac{3\lambda}{8}}^{\frac{5\lambda}{8}} \left[(j\omega\epsilon_\ell + \sigma_\ell)E_y^b(x) + j\omega\epsilon_{ox}E_y^a(x)\right]dx \quad (33)$$

The current and the equivalent admittances are normalized as follows:

$$\underline{i} = \frac{i}{j\omega\epsilon_{ox}Nd}$$

$$\underline{Y} = \frac{Y}{j\omega\epsilon_{ox}Nd}$$

Substituting for the field in equation (33) we get:

$$i_d = \frac{\lambda\phi^a(\emptyset)}{4h} + 16k(\epsilon_s - j\sigma_s)(V_o - V_1)$$
$$+ 2\sum_1^\infty \left[\epsilon_\ell - j\sigma_\ell + \coth(\frac{2\pi nh}{\lambda})\right]\phi^a(n)\sin(\frac{n\pi}{4})$$

$$i_f = \frac{\lambda\phi^a(\emptyset)}{4h} - 16k(\epsilon_s - j\sigma_s)V_k$$
$$+ 2\sum_1^\infty \left[\epsilon_\ell - j\sigma_\ell + \coth(\frac{2\pi nh}{\lambda})\right]\phi^a(n)\sin(\frac{n\pi}{4})\cos(n\pi) \qquad \underline{(34)}$$

The equivalent admittances can the be obtained from equation (32).

$$Y_{11}= \frac{1}{V_0}\left(\frac{\lambda\phi^a(\emptyset)}{2h} +16k(\varepsilon_s-j\sigma_s)(V_0-V_1-V_k) \right.$$
$$\left. +2\sum_1^\infty \left(\varepsilon_\ell-j\sigma_\ell+coth(\frac{2\pi n h}{\lambda})\right)\phi^a(n)sin(\frac{n\pi}{4})(1+cos(n\pi)) \right.$$

$$Y_{12}= \frac{1}{V_0}\left(\frac{-\lambda\phi^a(\emptyset)}{4h} +16k(\varepsilon_s-j\sigma_s)V_k \right.$$
$$\left. -2\sum_1^\infty \left(\varepsilon_\ell-j\sigma_\ell+coth(\frac{2\pi n h}{\lambda})\right)\phi^a(n)sin(\frac{n\pi}{4})cos(n\pi) \right. \qquad \underline{(35)}$$

Since the values of V_j will change for different values of bulk and surface properties, the Y parameters have strong frequency dependences.

4.2 Effects of Surface Impedance on the Gain-Phase Response

The ratio of the potential at the floating gate to the driven gate is presented in terms of gain and phase as defined below

$$Gain= -20log_{10}(|\frac{V_f}{V_d}|)$$

$$Phase= \sphericalangle\frac{V_f}{V_d}$$

For a uniform medium and no surface conductance or capacitance on the silicon dioxide/fluid interface, the gain phase response was obtained for varying bulk parameters. The calculated response agrees with the finite difference simulation for the sensor done by Lee [8]. Figure 4.2 shows the calculated gain-phase response for typical transformer
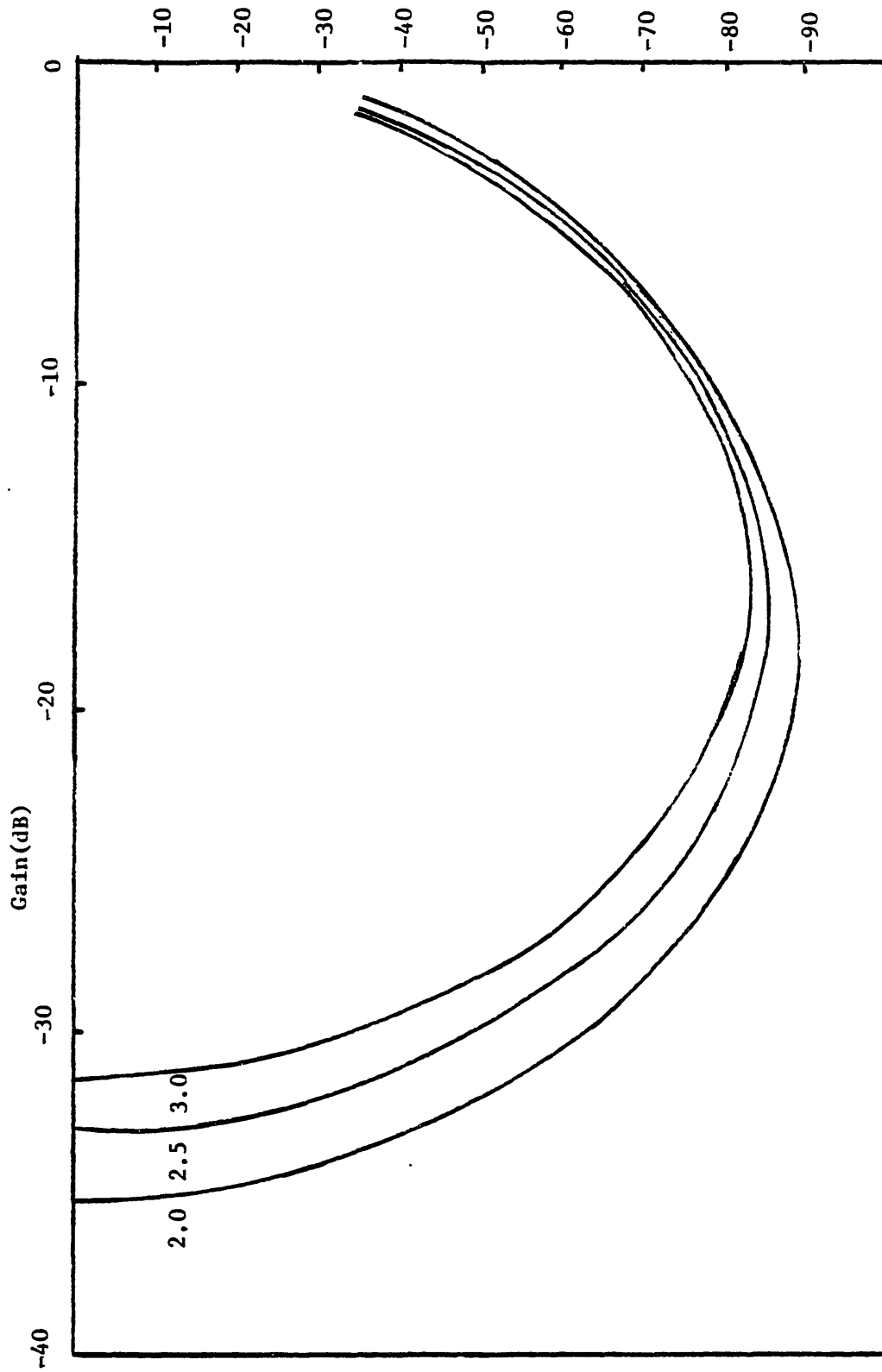
Figure 4.2

Calculated gain-phase response at typical oil permittivities
with no surface effects

oil permittivities and no surface effects. The intersection of the gain-phase curve with the gain axis corresponds to the high frequency response. The frequency decreases counterclockwise on the plot, corresponding to an increasing loss.

A conducting layer at the silicon dioxide/fluid interface can be formed by adsorption. The effect of surface conductivity on the gain-phase response is shown in figure 4.3, for a medium of relative permittivity of 2. The high frequency gain remains at its value with no surface conduction because at high frequencies, the loss approaches zero. The effect of surface conductivity starts dominating once it starts approaching the bulk conductivity.

An interesting phenomena is that the high frequency gain is no longer the minimum gain once the surface conductivity becomes appreciable compared to the bulk. The high frequency response corresponds to the capacitive voltage divider relation:

$$\frac{V_f}{V_d} = \frac{C_{12}}{C_{11}+C_{12}+C_L} \tag{36}$$

The mutual capacitance decreases with an increasing bulk or surface loss. This decrease of the equivalent capacitance at higher loss occurs because the electric field next to the floating gate develops a negative phase with respect to the applied potential. Thus, the conduction current has a negative phase also. The imaginary part of the conduction

56
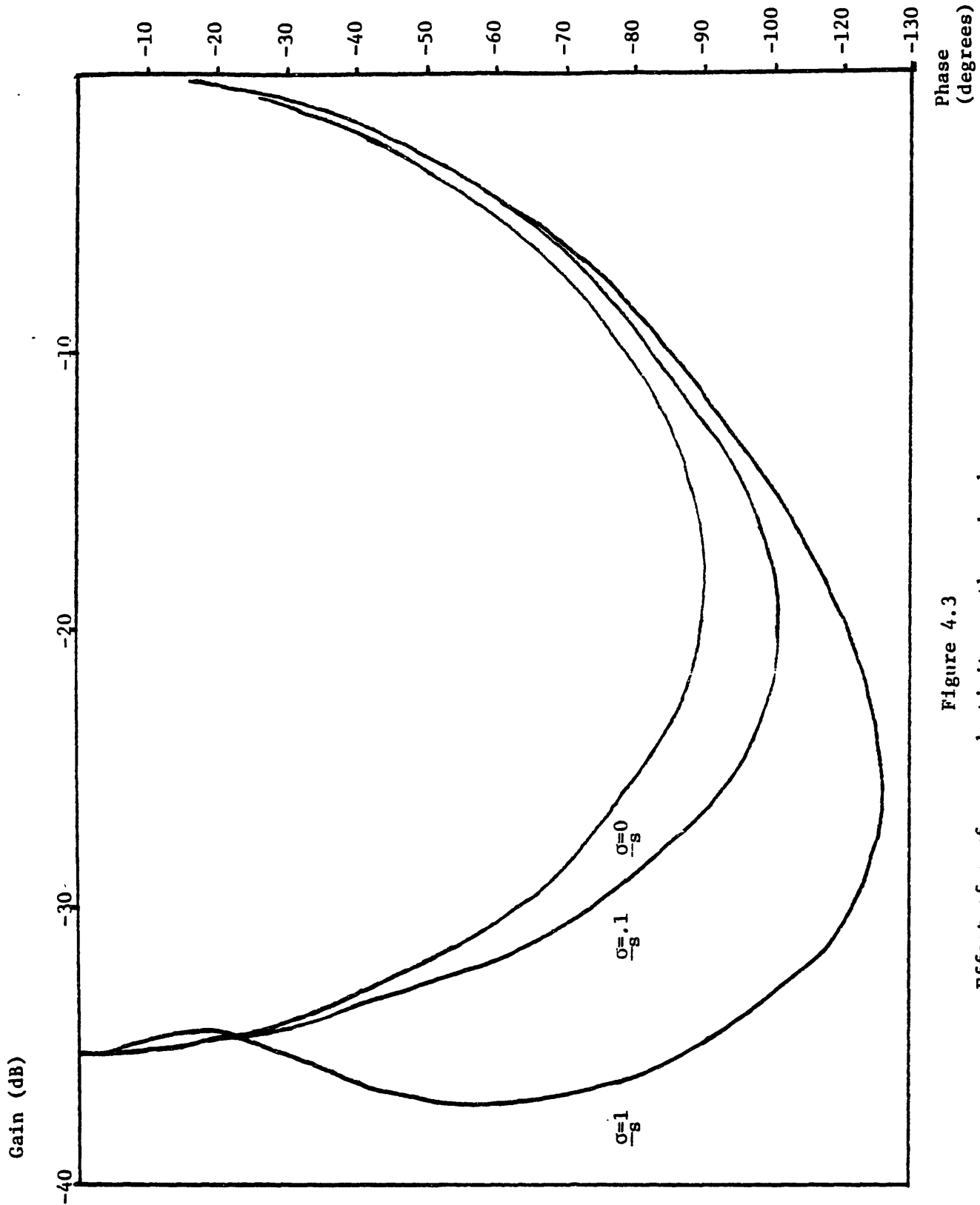
Figure 4.3

Effect of surface conductivity on the gain-phase response

for $\frac{\epsilon_\ell}{\epsilon_o} = 2.0$ and $\underline{g}_\ell = 1.0$

current contributes a negative component to the capacitive current to the floating gate, thus decreasing the equivalent mutual capacitance between the two electrodes. The mutual conductance $\underline{G}_{12}$ (i.e. the imaginary part of $\underline{Y}_{12}$) does not compensate for the decrease of $\underline{C}_{12}$, and thus the gain reaches a value less than its high frequency limit. As the frequency increases the mutual capacitance rises back to its value with no surface conductance, and the gain increases.

The surface permittivity might not be applicable to the transformer oil measurement, since an appreciable surface permittivity needs very highly polarizable molecules to align along the interface in great concentrations. However, it might be appropriate to model another surface phenomena with such a surface permittivity. The effect of various surface permittivities on the gain phase response of a medium with a permittivity of 2 is shown in figure 4.4. The high frequency gain increases due to the contribution of the surface polarization current.

4.3 Surface Contact Effect

The surface conductance between the electrodes can be non uniform. If the surface conduction is caused by electrically induced adsorption, the lack of uniformity of the electric field causes the surface conductivity to vary along the x axis. The numerical simulation can account for a spatially varying surface impedance.

An accumulation of charges next to the electrodes

58
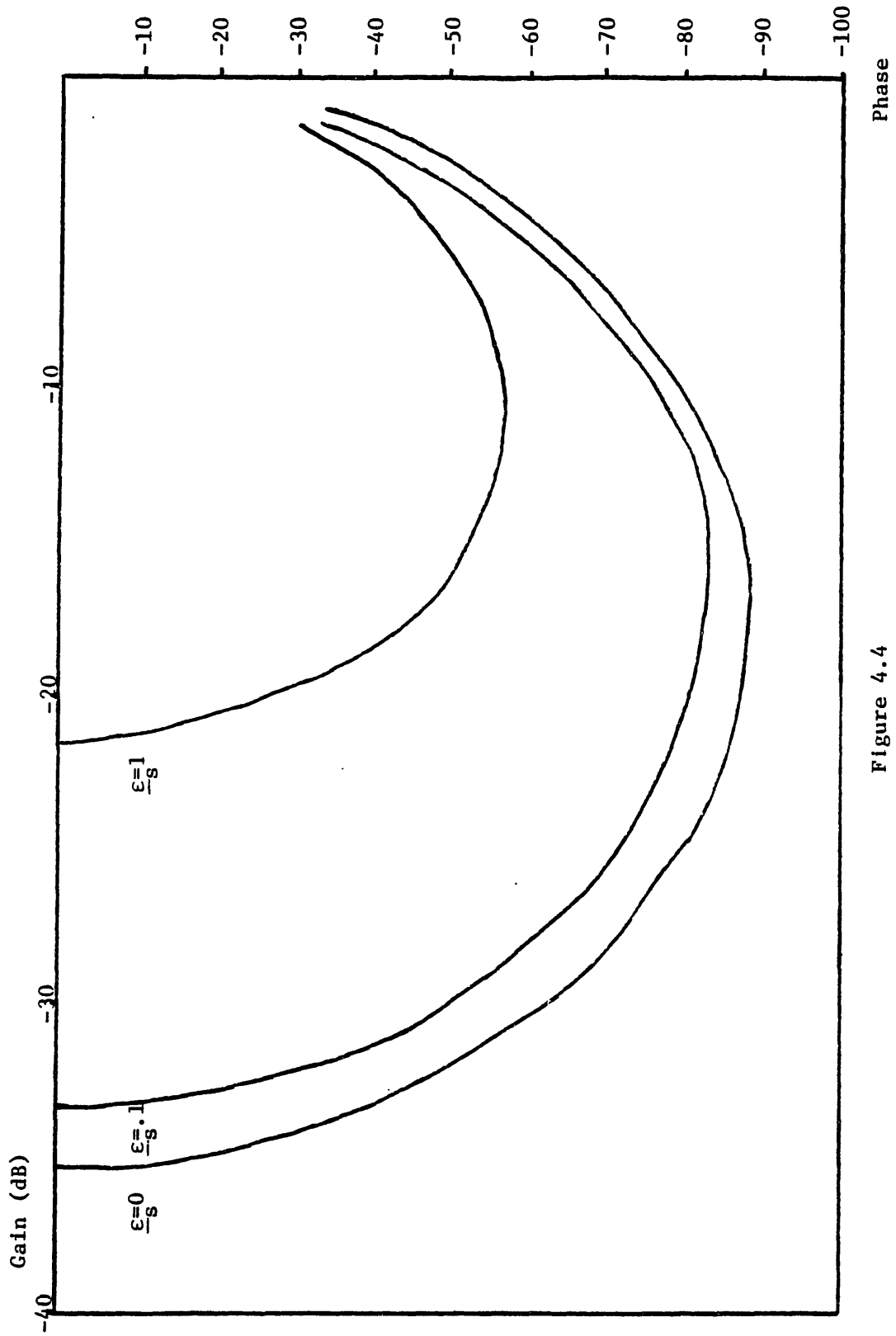
Figure 4.4

Effect of surface capacitance on the gain-phase response

for $\frac{\epsilon_\ell}{\epsilon_o} = 2.0$

causes a difference between the surface properties next to the electrodes and the rest of the interface [36]. From the edge of each electrode to a distance Δ on the interface, the surface conductivity is σ_{sc} and the surface permittivity is ϵ_{sc}. The two surface parameters σ_{sc} and ϵ_{sc} are referred to as the contact parameters because they reflect the surface properties next to the contact, but their dimensions are still surface dimensions (i.e. mhos for σ_{sc} and mhos/sec for ϵ_{sc}). The effect of zero contact conductance is shown in figure 4.5 for a contact region width $\Delta = \frac{W}{50}$ and bulk and surface parameters as indicated in the figure.

For a medium with a small bulk conductivity and a high surface conductivity, the gain-phase response has a dual hump shape as shown in figure 4.6 caused by the zero contact conductivity. Starting from the high frequency limit, the gain decreases with frequency, approaching an asymptotic gain determined by the capacitance of the structure. As the frequency decreases further, conduction through the bulk causes the gain to increase to zero following the second hump on the gain-phase curve. The width of the contact region Δ determines the asymptotic gain value of the first hump. As shown in figure 4.6, the asymptotic gain increases with decreasing Δ.
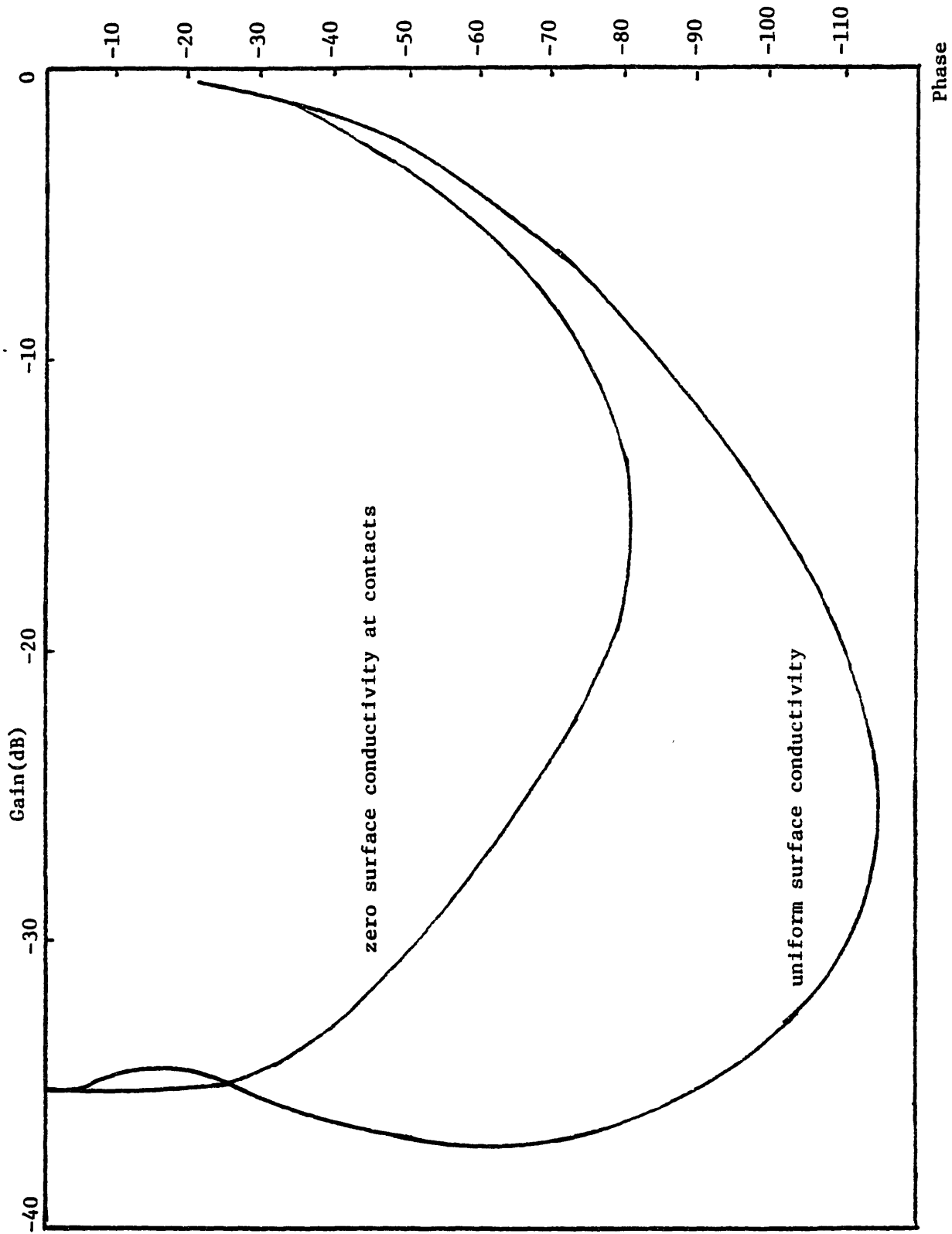
Figure 4.5

Effect of zero surface conductivity at contacts on the gain-phase response for $\frac{\varepsilon_\ell}{\varepsilon_o} = 2.0$ and $\frac{\lambda \sigma_\ell}{\sigma_s} = 1.0$
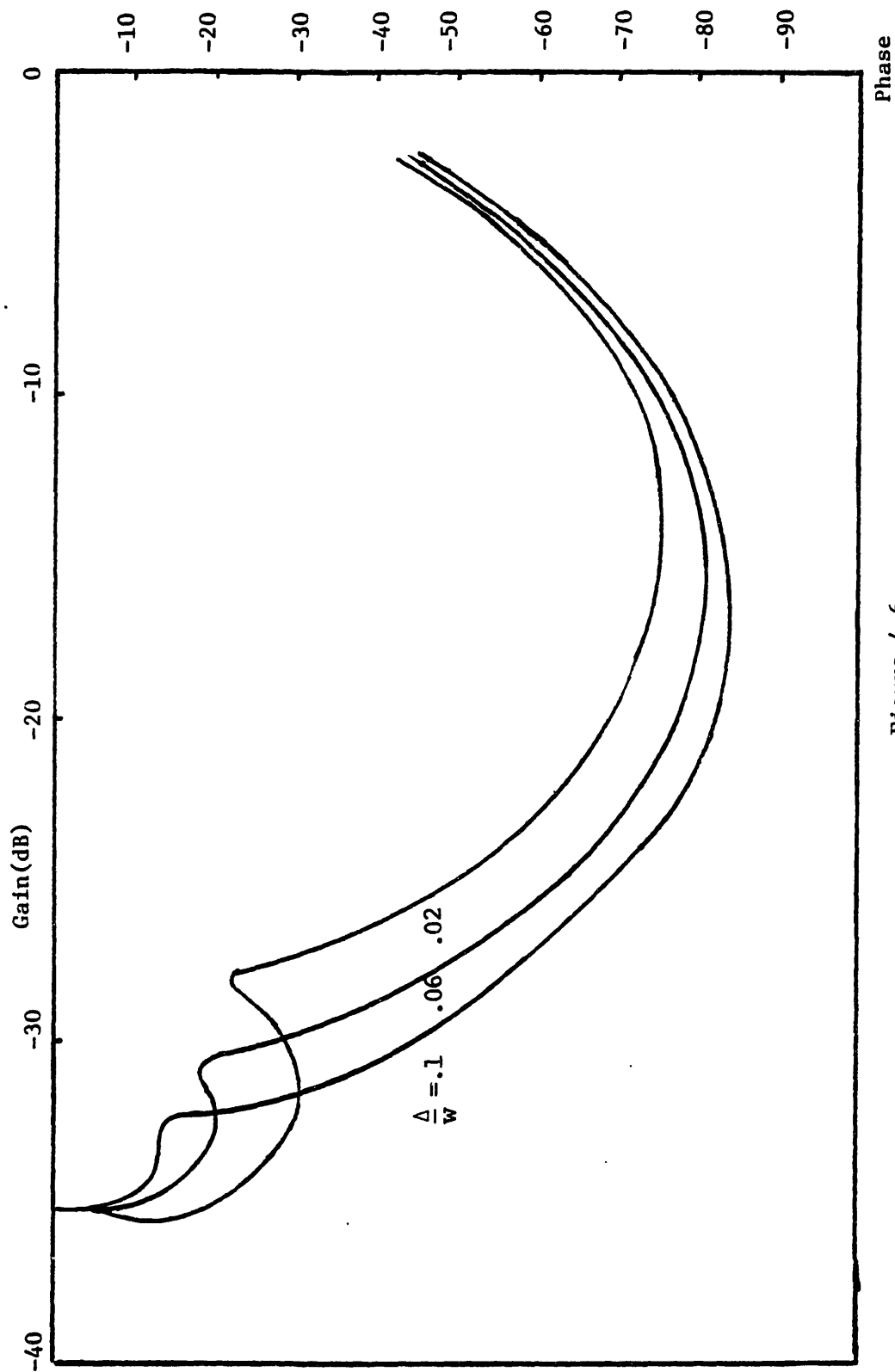
Figure 4.6

Effect of zero contact conductivity on the gain-phase response for a highly conducting interface

$$\frac{\epsilon_\ell}{\epsilon_o} = 2 \quad \& \quad \frac{\lambda\sigma_\ell}{\sigma_s} = .1$$

Chapter V

Experimental Work

Basic experiments characterizing the response of microdielectric sensors in transformer oil are described in this chapter. The goal of these experiments has two aspects, one concerning understanding the nature of the surface phenomena occurring at the surface, the second is investigating the ability of the sensors to detect contamination which causes a rise of conductivity.

5.1 The Experimental Setup

Microdielectric sensors are used to study the dielectric properties of transformer oil. The experimental setup is shown in figure 5.1. The sensor is connected to a Micromet SystemII which applies a synthesized ac voltage to the sensor, and measures the response (i.e. the floating electrode potential). A conversion table based on the uniform medium assumption is built into the memory of the system and provides conversion from gain and phase of the response signal to the permittivity and loss of the medium. An IBM personal computer interfaces with the Micromet SystemII and monitors the experiments. The range of frequencies available are between .005 Hz and 10 kHz.

The sensor is immersed in the oil sample in a beaker. Since the sensors show a sensitivity to humidity, they are dried and introduced to the oil sample in a nitrogen
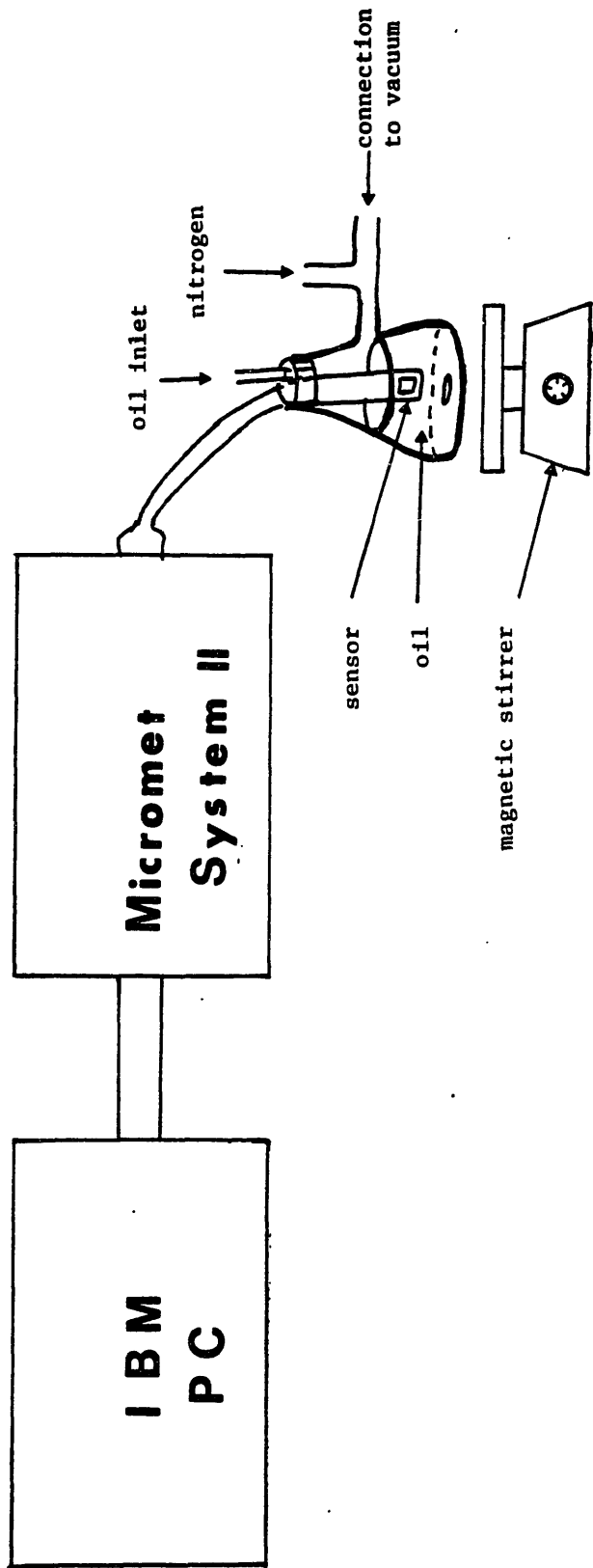
Figure 5.1
The experimental setup

ambient. The sensor is exposed to a flow of nitrogen for about 20 minutes in an empty beaker, then a vacuum is pulled over the beaker. Oil is dropped into the evacuated beaker, and a second flow of nitrogen brings the beaker back to atmospheric pressure. The sample is then sealed from the atmosphere. The response of various oils is studied as described in the following sections.

In the experimental results to be presented, surface effects are evident. Since the conversion table does not account for the surface phenomena, it can not be used to extract the bulk permittivity $\frac{\epsilon_\ell}{\epsilon_o}$ and loss $\frac{\sigma_\ell}{\omega\epsilon_o}$. However, the values obtained from the conversion table for the equivalent permittivity ϵ' and loss ϵ'', while not necessarily representative of the bulk parameters, can provide hints on the surface phenomena involved.

5.2 Response of Clean Oil

Transformer oil of commercial purity was studied. The oil had 35 ppm water contents. The oil sample was stirred under vacuum for a few hours. After the oil had stopped degassing the response of the sample was recorded while it was still stirred under vacuum. The results shown in figure 5.2 were obtained using two different sensors, and show a good agreement between sensors. Figures 5.2a and 5.2b show the gain and phase at frequencies ranging between .005 Hz and 100 Hz. Figure 5.2c shows the gain vs the phase. The gain phase response deviates from the response of a medium

65

Gain(dB)

Figure 5.2a

Figure 5.2

Response of clean oil
sample stirred under
vacuum.

Log frequency (Hz)

Phase

Figure 5.2b

Log frequency (Hz)

Figure 5.2c

Figure 5.2d

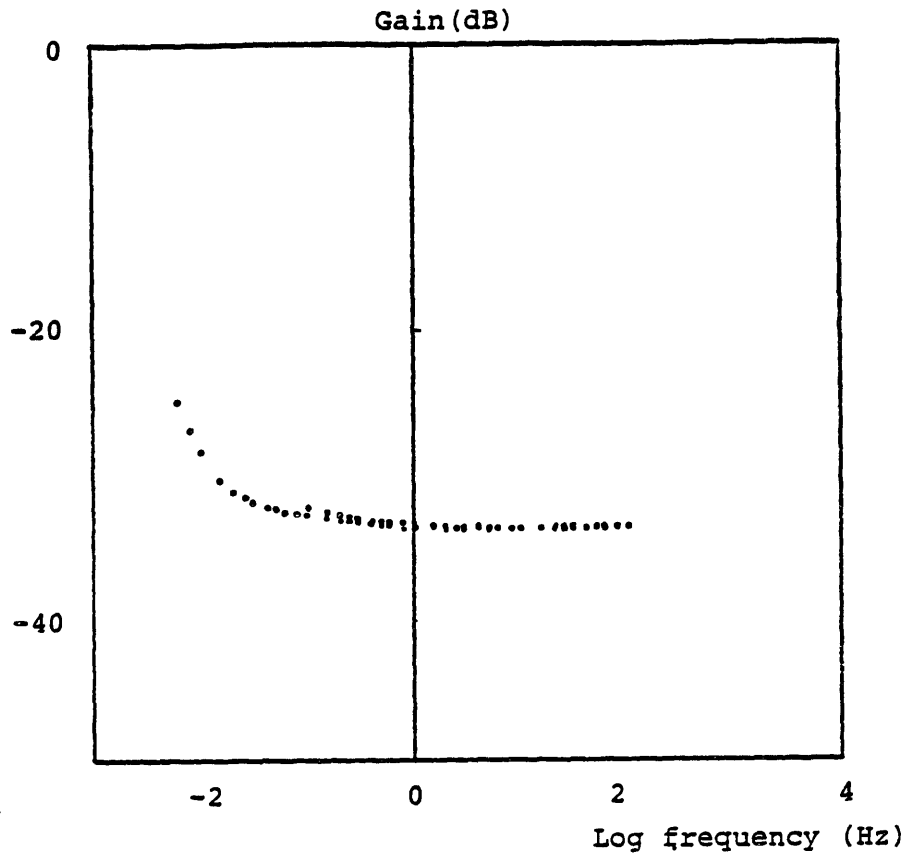Figure 5.2e
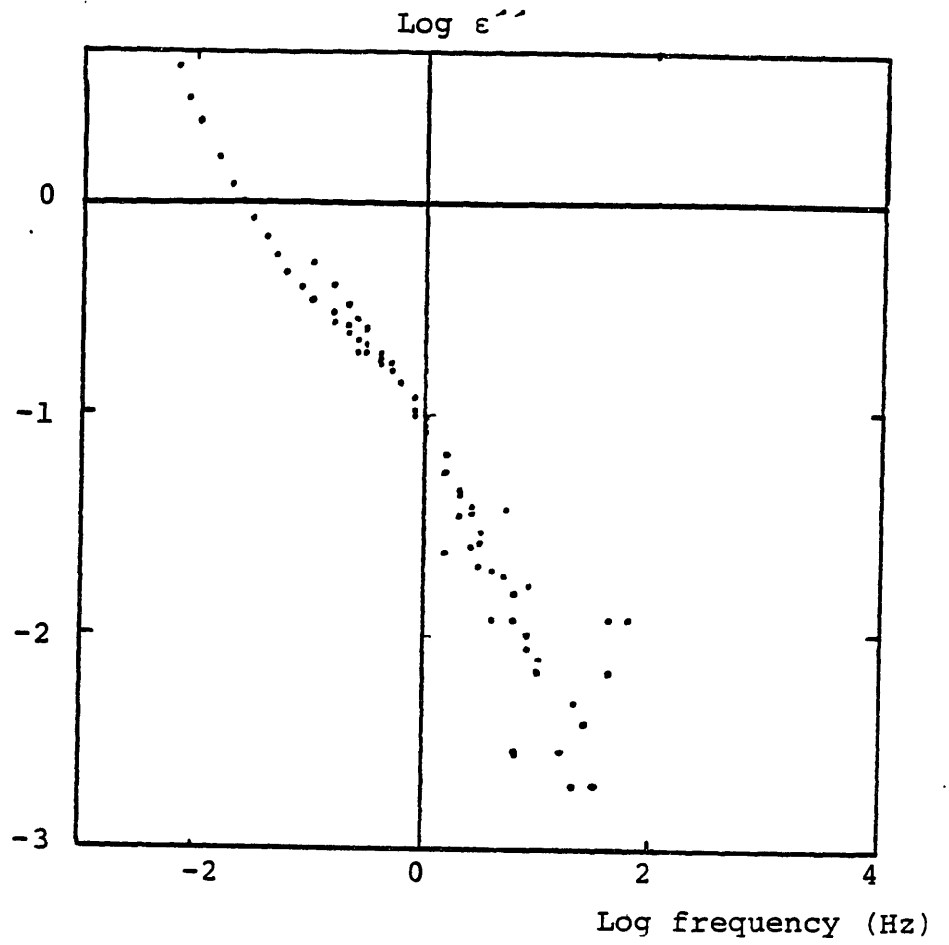
Figure 5.2f
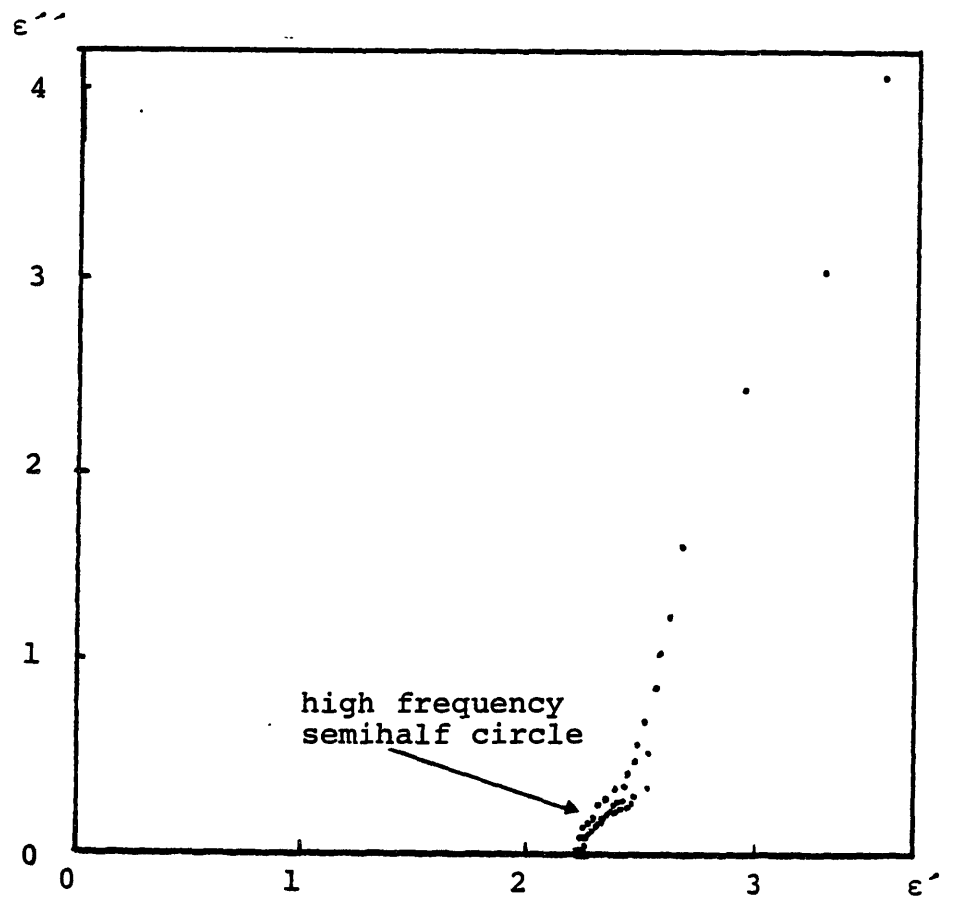
with uniform non dispersive bulk and no surface effects. The dashed line on figure 5.2c indicates the calculated response for a uniform medium with no surface effects. When the gain phase information is converted to relative permittivity ε' and loss ε'', the permittivity, as shown in figure 5.2d, deviates from its high frequency value of 2.25. Deviation occurs for frequencies less than 1 Hz. The loss also deviates from the $\frac{1}{\omega}$ behavior (corresponding to a slope of -1 on the log-log scale of figure 5.2e) expected for ionic loss. The high degree of noise at higher frequencies of loss measurement is due to the loss value approaching the sensitivity range of the device. A plot of ε'' vs ε' (i.e. a Cole-Cole plot) in figure 5.2f shows the beginning a small semi circle for higher frequencies followed by a curve of a larger curvature at lower frequencies. In the next chapter it is shown that the properties measured are not the bulk parameters but are highly influenced by surface phenomena. A measurement of the bulk permittivity at 200 Hz using a General Radio bridge yields a permittivity of 2.26. The conductivity was below the sensitivity of the bridge.

A sample of reclaimed oil was also studied. The response as shown in figure 5.3 is similar to that of pure oil. The permittivity is again 2.2 at high frequencies and increases for frequencies below 1 Hz. The small semicircle is not clearly apparent on the Cole-Cole plot (figure 5.3f). When the sample was left exposed to air for few days, and then connected again to the vacuum pump and stirred under

Figure 5.3a
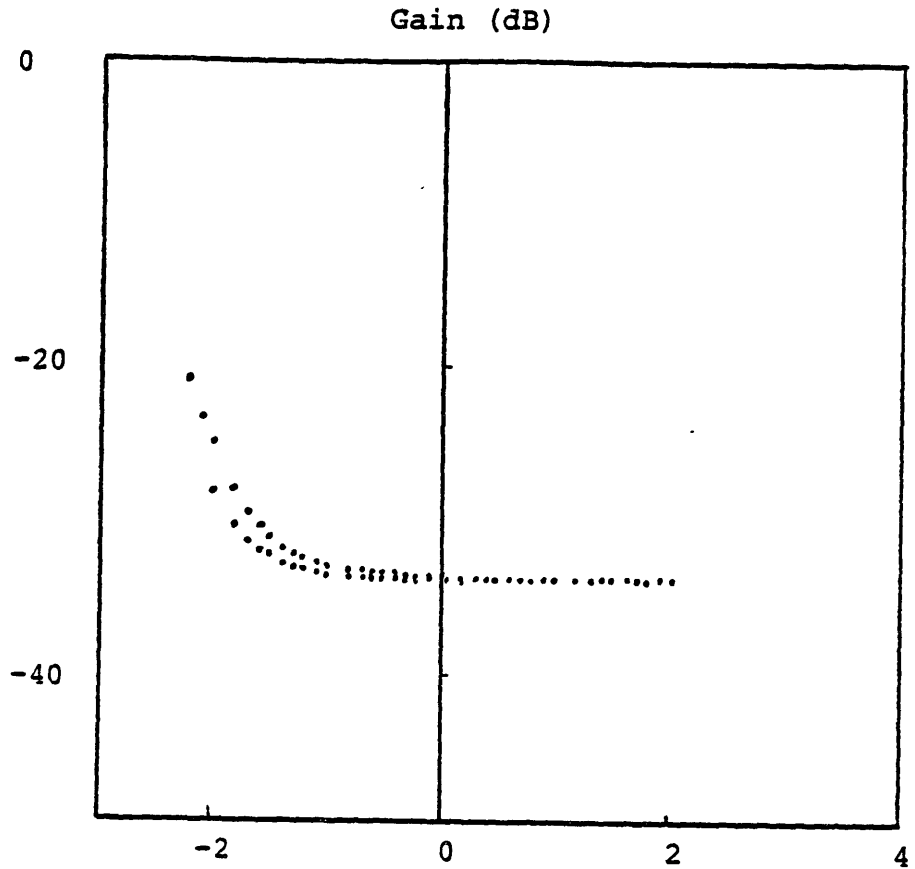
Figure 5.3

Response of reclaimed
oil stirred under vacuum.

Figure 5.3b

Gain (dB)

−40 −20 0

Figure 5.3c

Phase

Log ε′

Figure 5.3d

Log frequency (Hz)

Figure 5.3e

Figure 5.3f
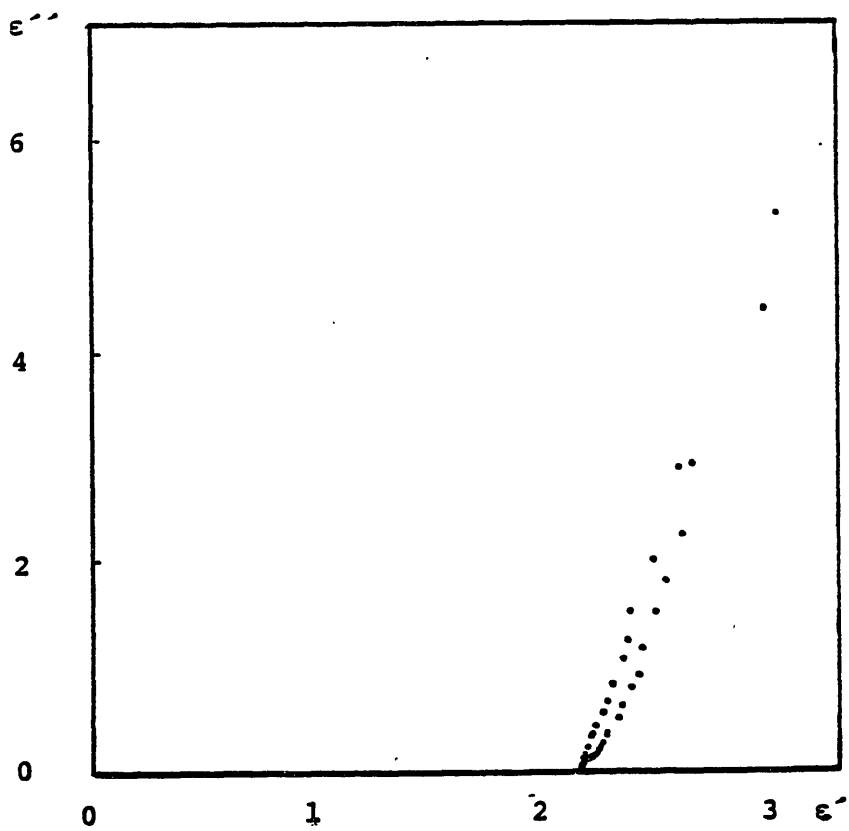
vacuum, the response (shown in figure 5.4d) showed an increased conductivity (at 1 Hz) from 4.6×10^{-12} mho/m before exposure to air to 12.4×10^{-12} mho/m following the exposure to air. The high frequency semihalf circle is more apparent for this case with higher conductivity as shown in figure 5.4f. Furthermore, the gain-phase plot also has two lobes, the smaller lobe corresponding to the higher frequencies. The frequency corresponding to the breakpoint on the gain-phase and Cole-Cole plots is around .25 Hz. This type of gain-phase response is explained in chapter six.

The response of a sample sealed under nitrogen was studied. The sample was not stirred while taking the measurements shown in figure 5.5. The response in the first 24 hours shows a high similarity to that of the sample stirred under vacuum shown in figure 5.2. Three of the measurements shown in figure 5.5 were taken in the first 24 hours of immersing the sensor in the oil sample. The sample was left sealed under nitrogen and was checked 20 days later. The response 20 days later has changed considerably. It is shown in figure 5.5 superimposed on the response obtained earlier. The conductivity at 1 Hz has increased from $\simeq 3 \times 10^{-12}$ to 14.5×10^{-12}. The gain-phase plot also has a hump of similar nature to that shown in figure 5.4c, but approaching a larger gain. The hump in figure 5.4c reaches an asymptotic gain of -32 dB, while in figure 5.5c it heads towards a gain of -17 dB. When the sample used in figure 5.5 was stirred the asymptotic value of the hump on the gain

Figure 5.4a

Gain (dB)

0

−20

−40

−2   0   2   4
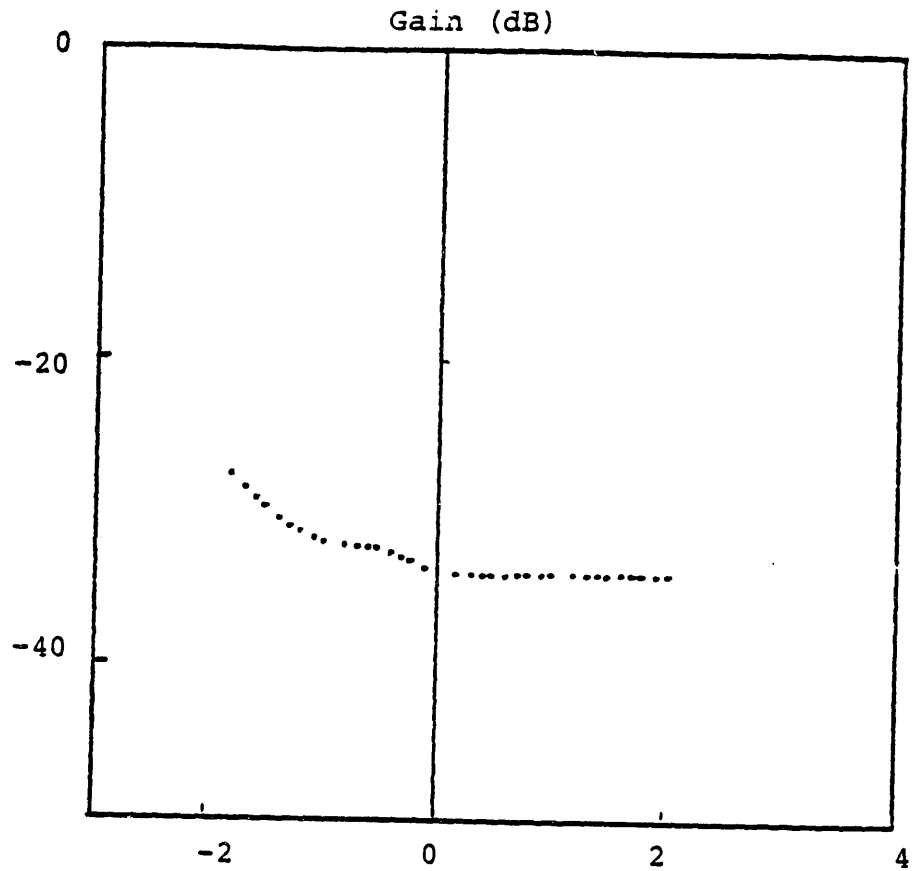
Log frequency (Hz)

Figure 5.4

Response of reclaimed
oil stirred under vacuum
after it has been left
exposed to air.

Figure 5.4b

Phase

0

−20

−40

−60

−2   0   2   4

74
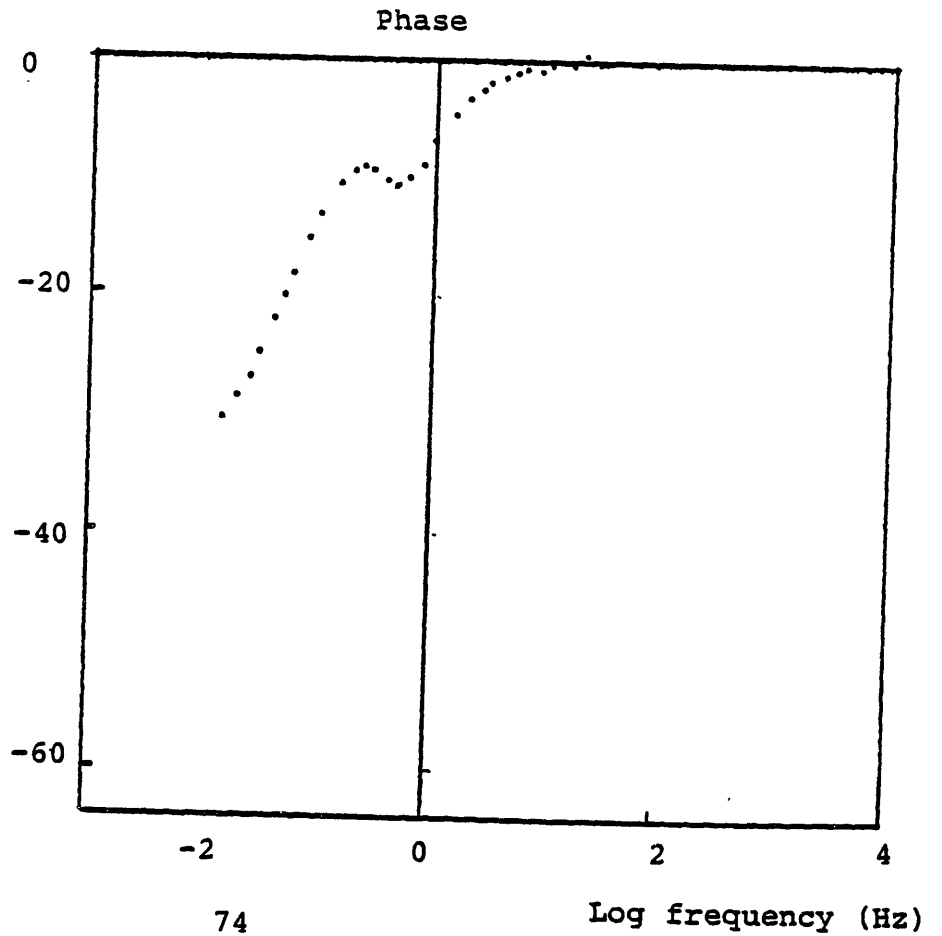
Log frequency (Hz)

Figure 5.4c
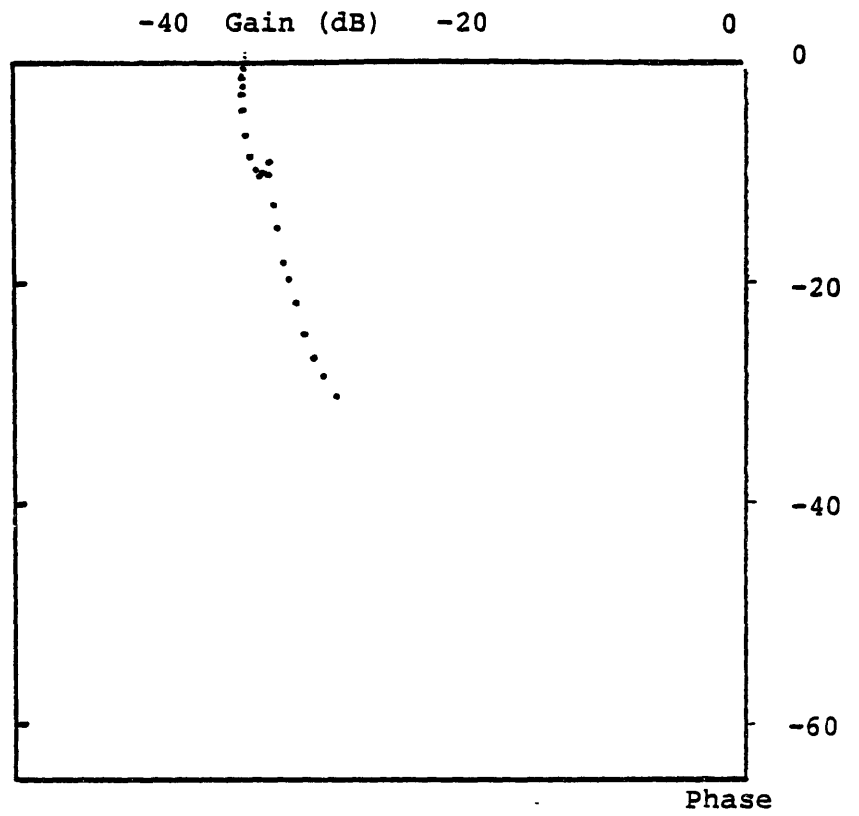
Figure 5.4d
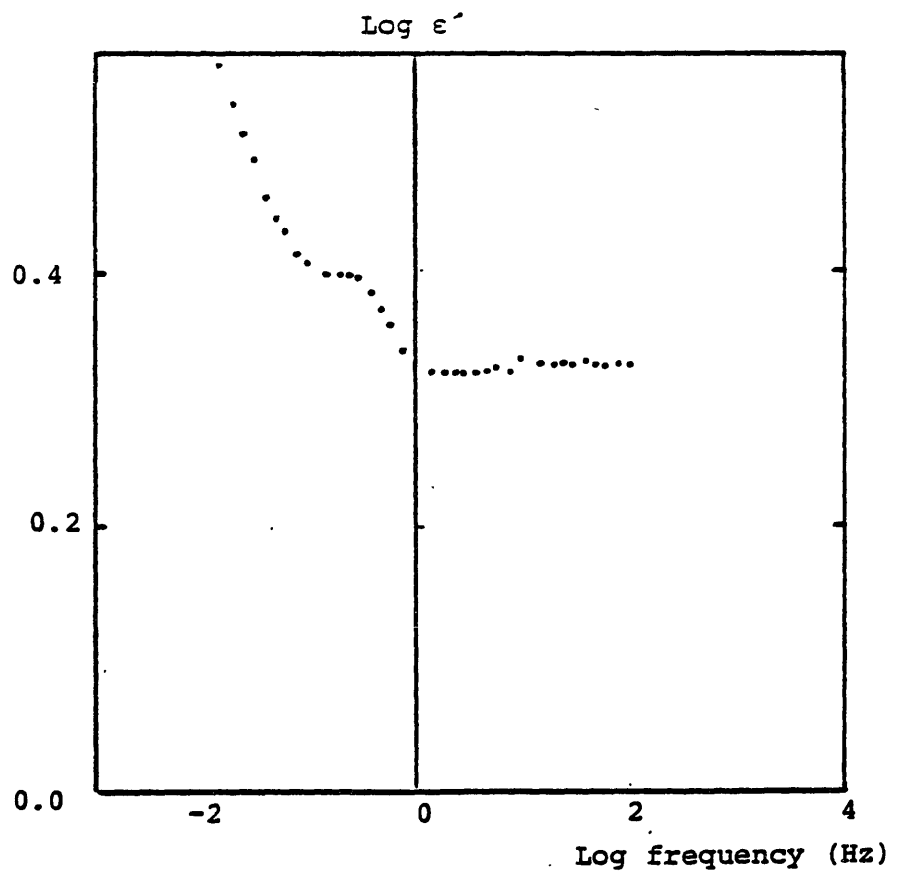
Figure 5.4e
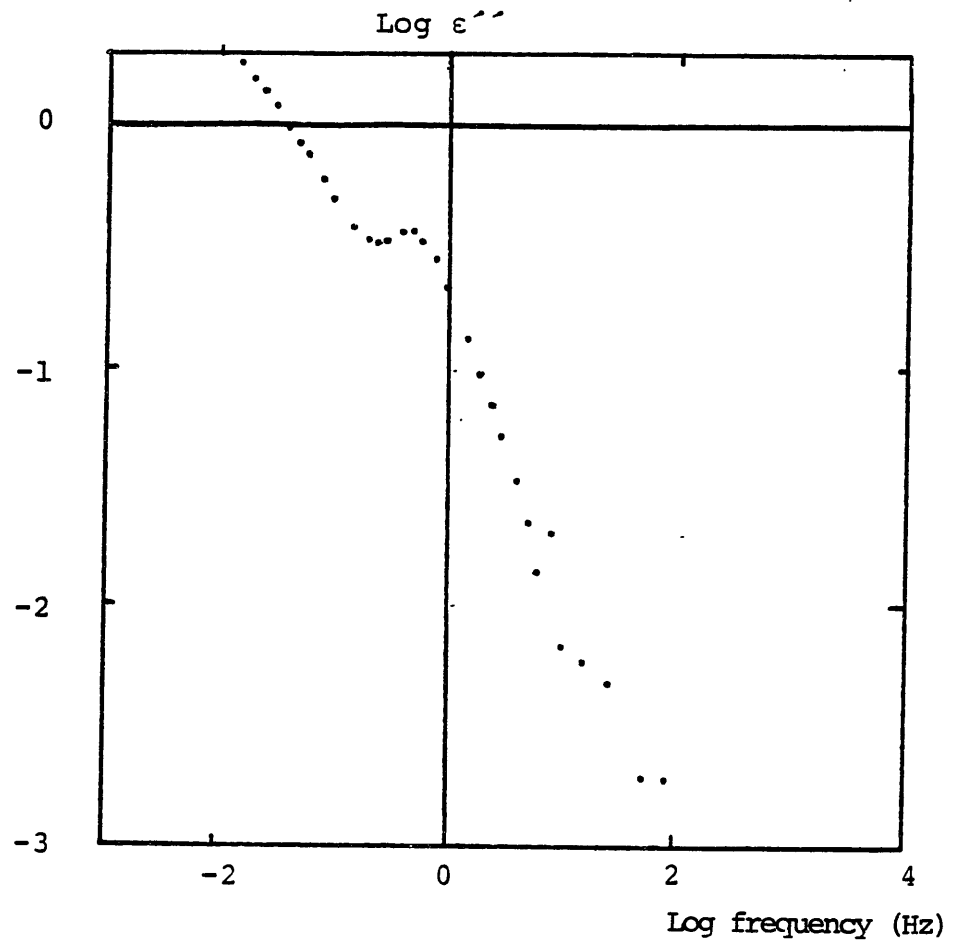
Figure 5.4f

Figure 5.5a

Gain (dB)
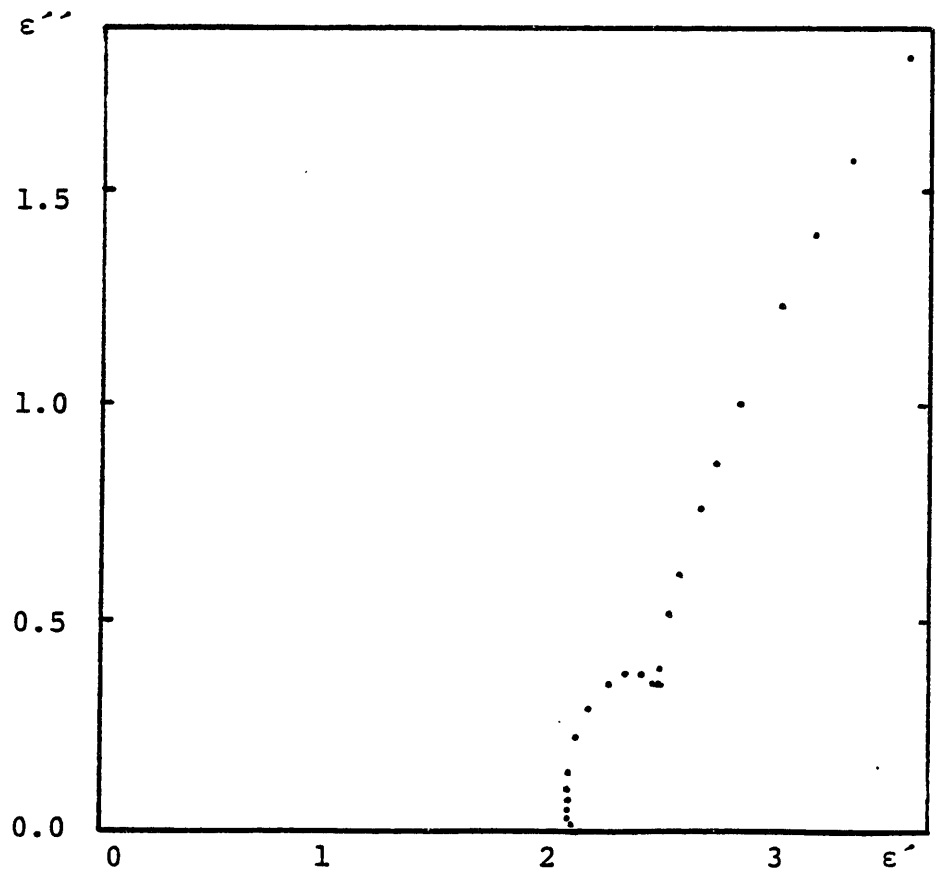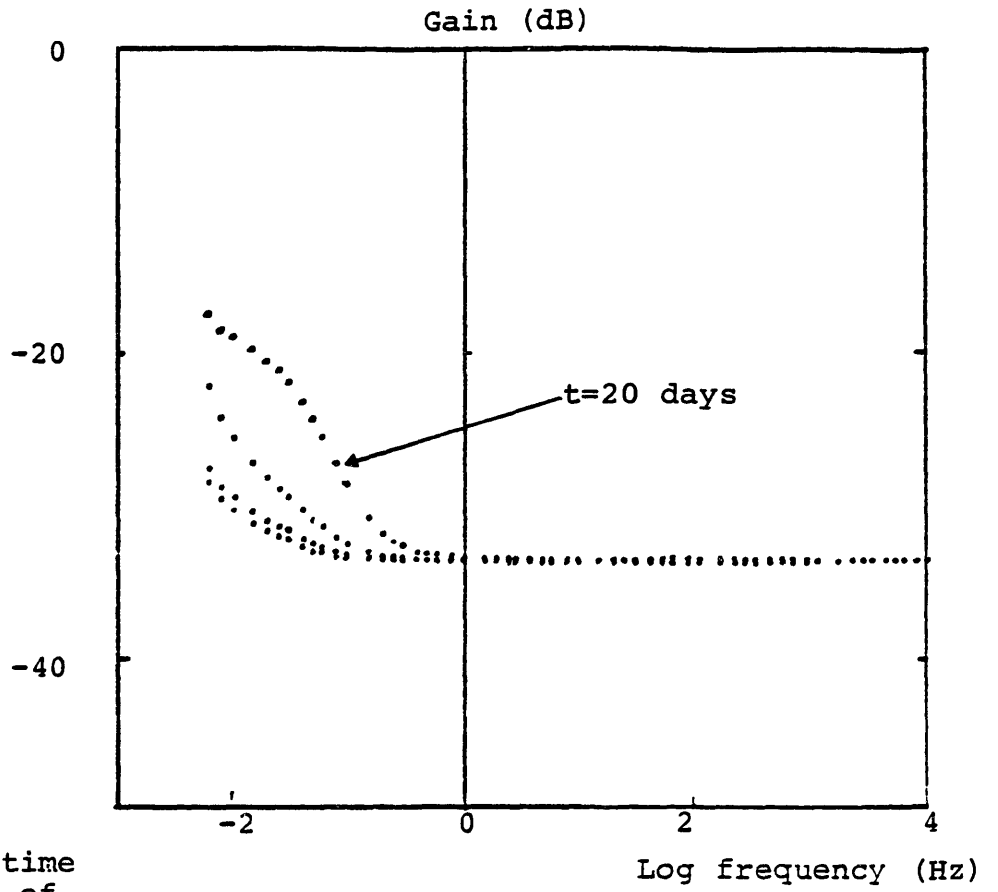
Figure 5.5

Variation with time
of the response of
a clean oil sample
sealed in a nitrogen
ambient.

Figure 5.5b

Phase

Figure 5.5c

Gain (dB)

t=20 days

Phase

Log ε´´

Figure 5.5d

t=20 days

Log frequency (Hz)

78
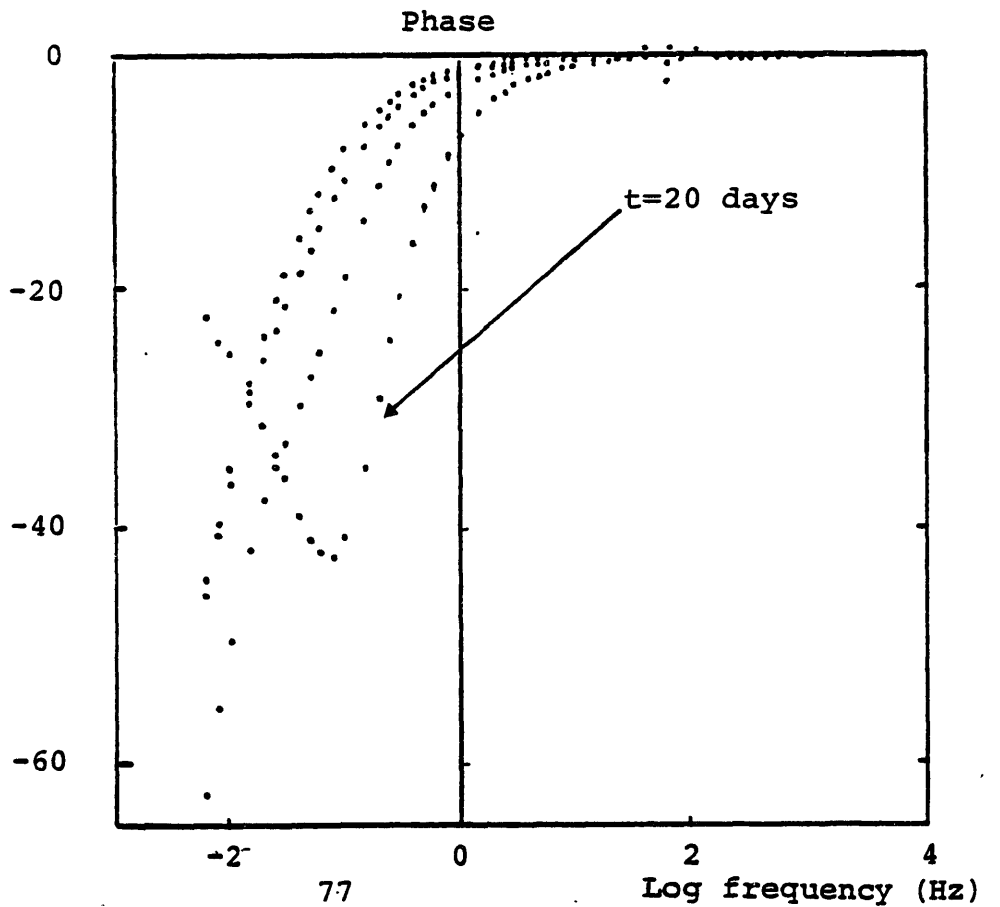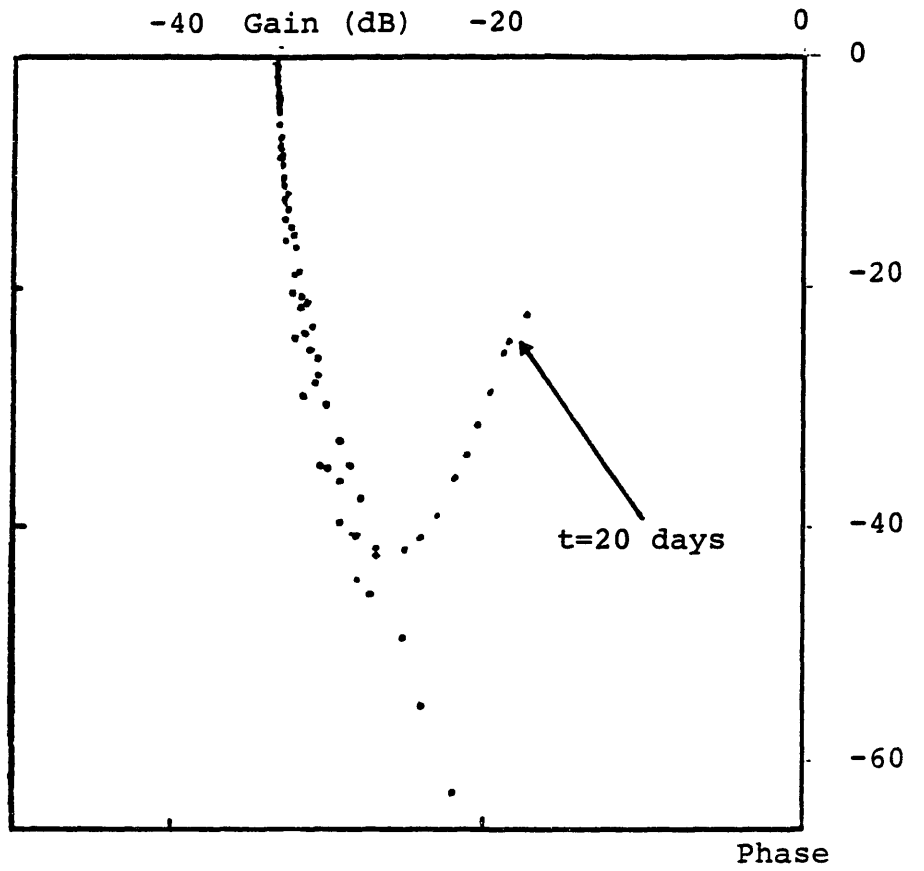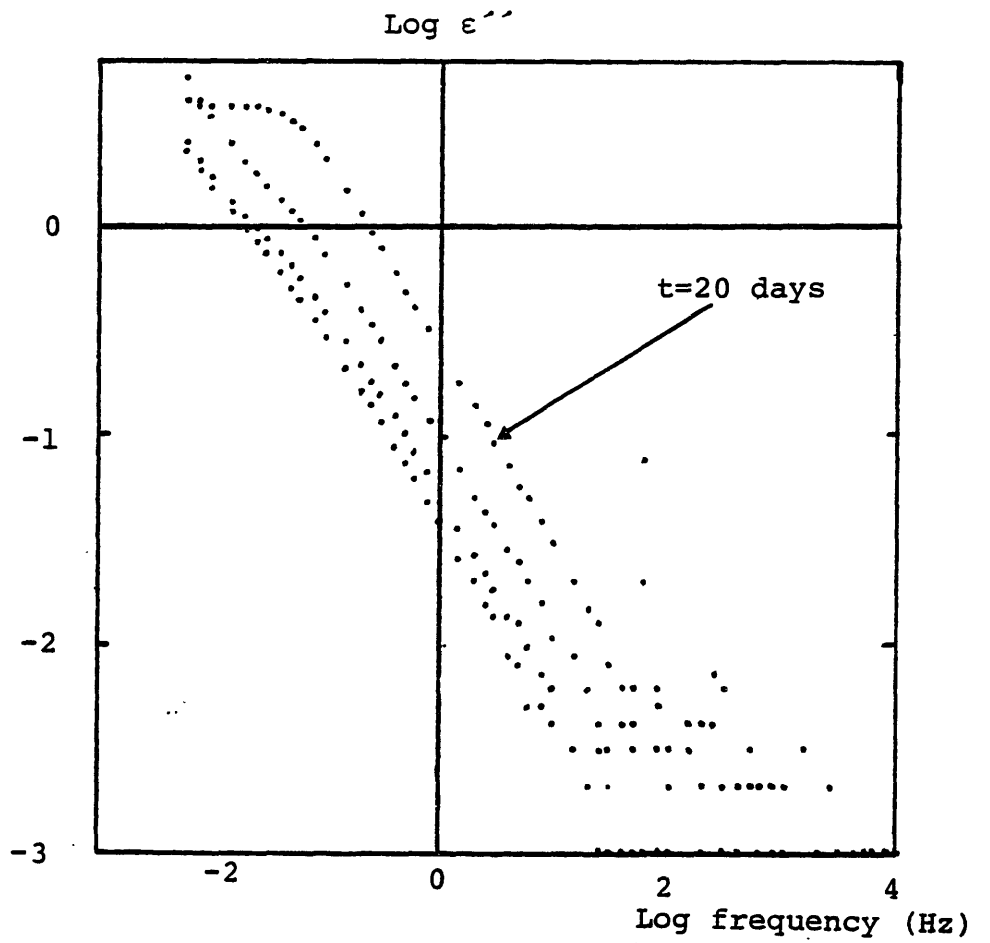
Figure 5.5e

Figure 5.5f

79
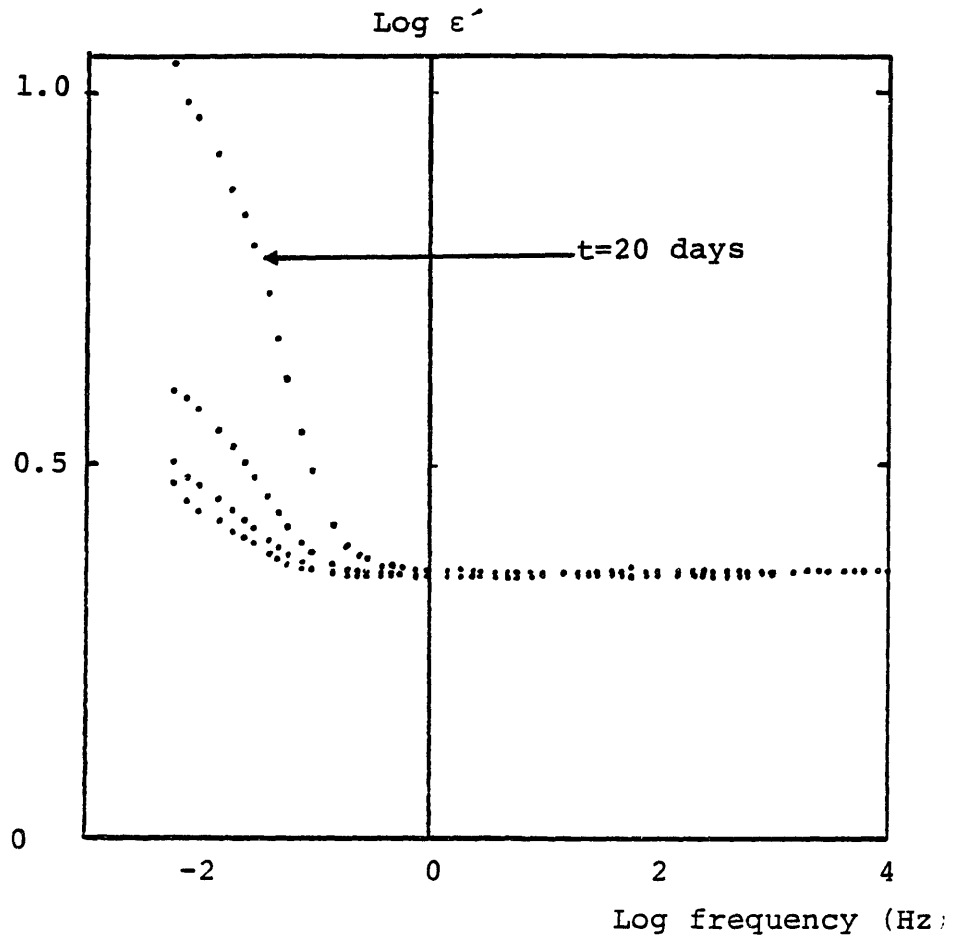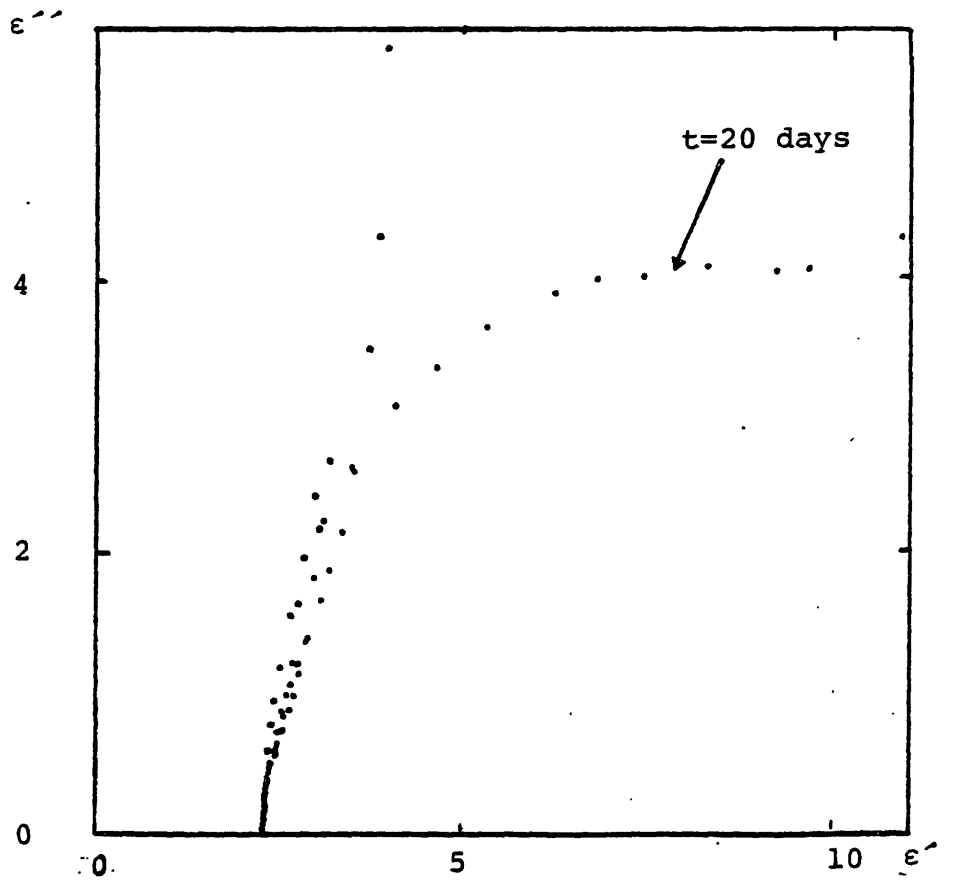
phase-plot decreased to -31 as shown in figure 5.6c. The radius of the semihalf circle also decreased drastically. Based on other experiments described later in this chapter and based on the explanations provided in chapter six, the gain-phase plot for the nonstirred sample is expected to follow also a secondary hump, and the loss is expected to rise after the semihalf circle. So the frequency breakpoint at which the gain phase plot follows the secondary hump on the gain phase plot is less than .006 Hz, and may be very close to this frequency because the phase seems to be approaching its local maxima. For the stirred sample the frequency breakpoint is $\simeq$ .3 Hz.

Stirring was investigated further in a freshly immersed sample. A sensor was placed in a fresh sample of clean oil. The response at .01 Hz was observed as stirring was turned on and off during a period of 130 hours. Figure 5.7 shows the response as a function of time for two consecutive alternating periods of stirring and nonstirring. Both the equivalent permittivity and loss at this frequency were reduced under stirring. The permittivity at .01 Hz with stirring is $\simeq$ 2.1 while with nonstirring it is $\simeq$ 2.5. The permittivity at high frequencies both with stirring and nonstirring was found to be 2.1 as shown in figure 5.8d. Figure 5.8 shows some differences which were typically observed between frequency scans with and without stirring. The high frequency semicircle on the Cole-Cole plot as shown in figure 5.8f is more apparent in the case of stirring and

Figure 5.6a
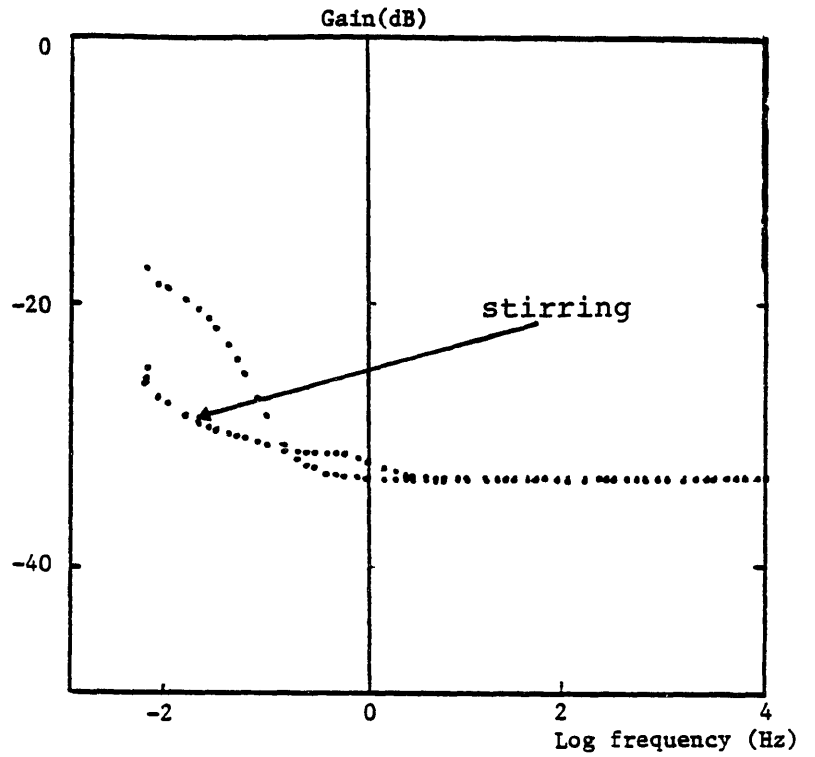
Figure 5.6

Effect of stirring for an oil sample left sealed under a nitrogen ambient for more than 20 days.

Figure 5.6b
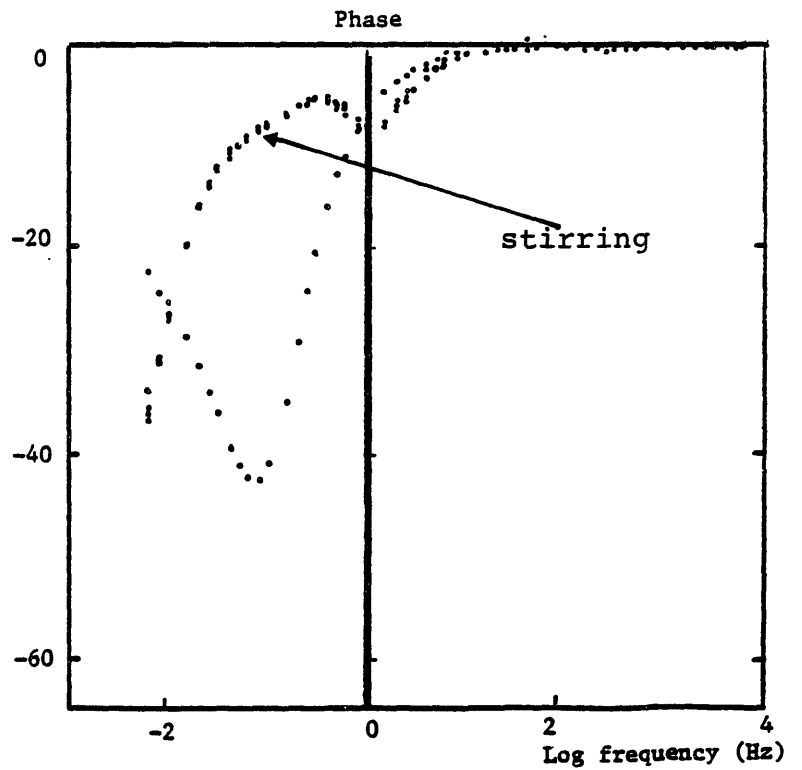
Figure 5.6c
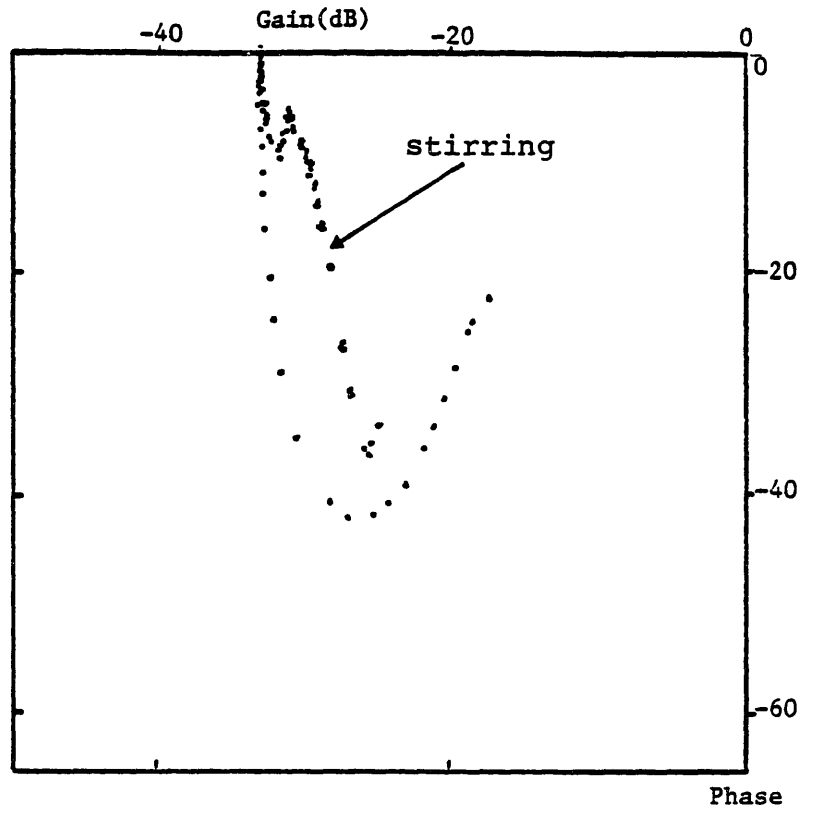
Figure 5.6d
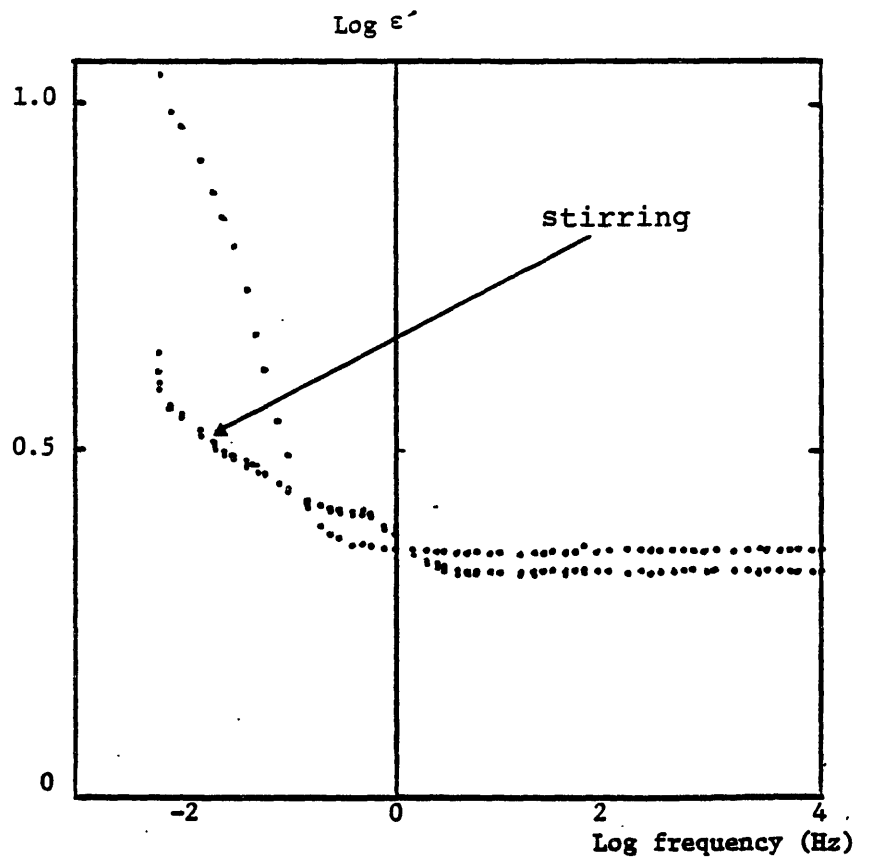
Figure 5.6e

Figure 5.6f

Gain(dB)
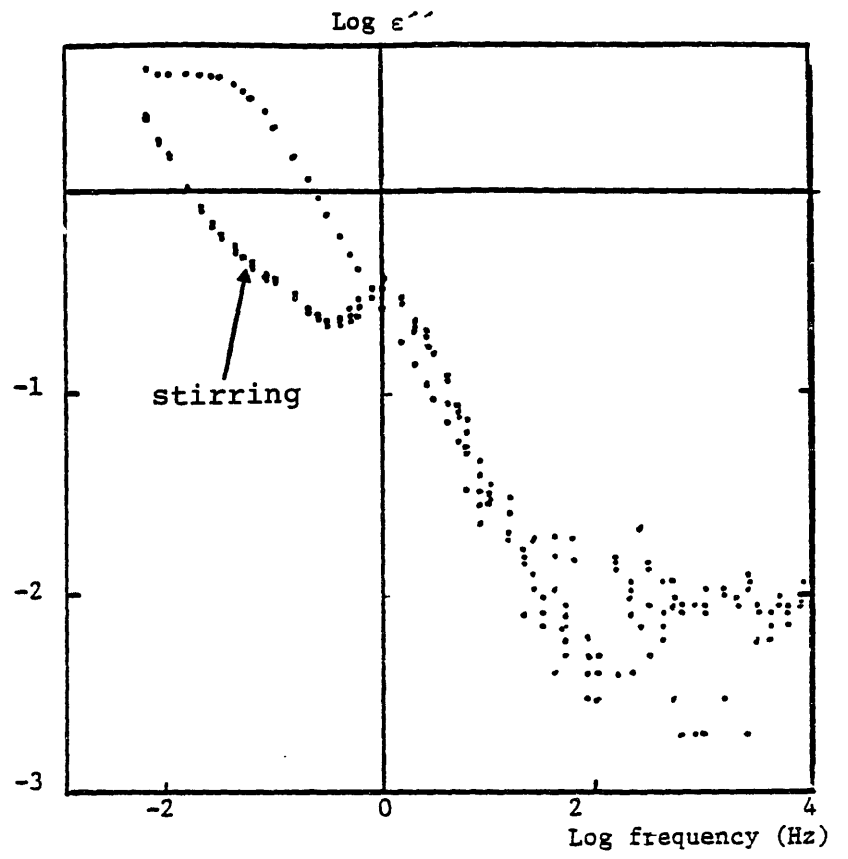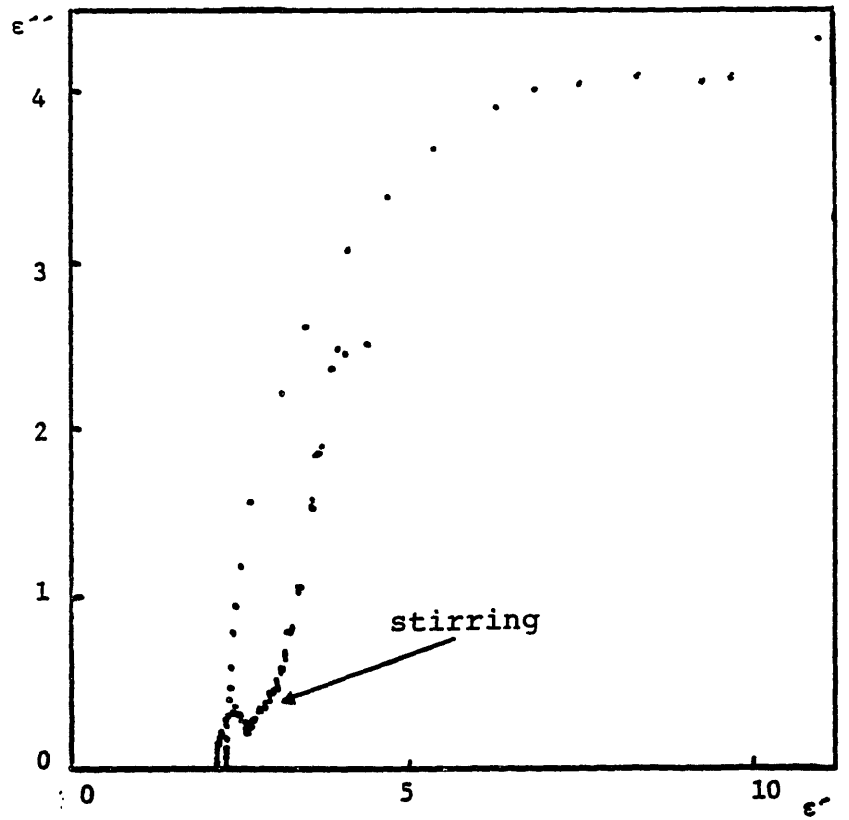
Figure 5.7a

● stirring

* non stirring
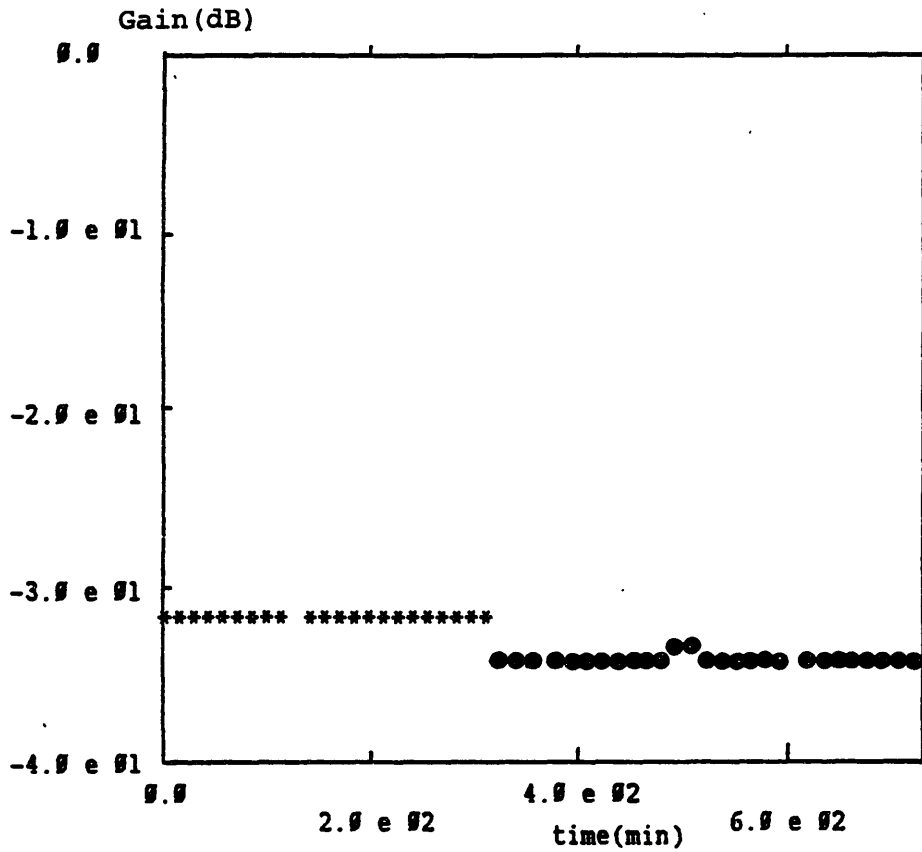
Figure 5.7
Response of clean oil at .01 Hz as a function
of time in two consecutive nonstirring and
stirring periods

Phase

Figure 5.7b

84
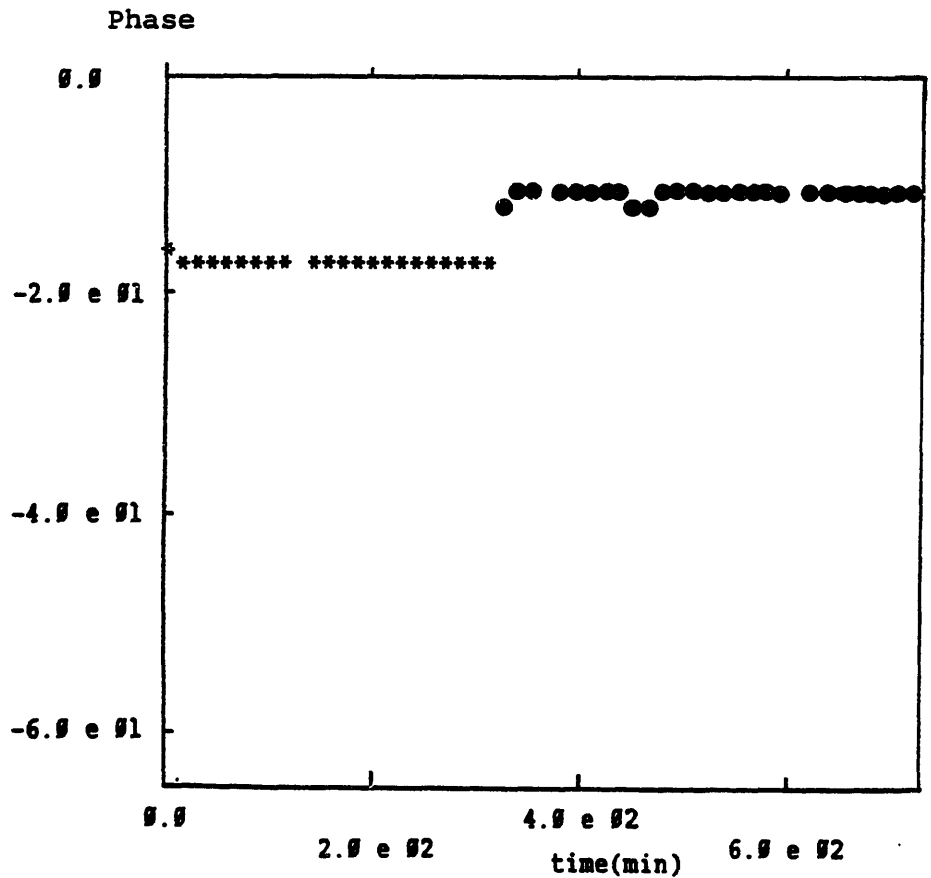
Figure 5.7c

Figure 5.7d

Gain (dB)
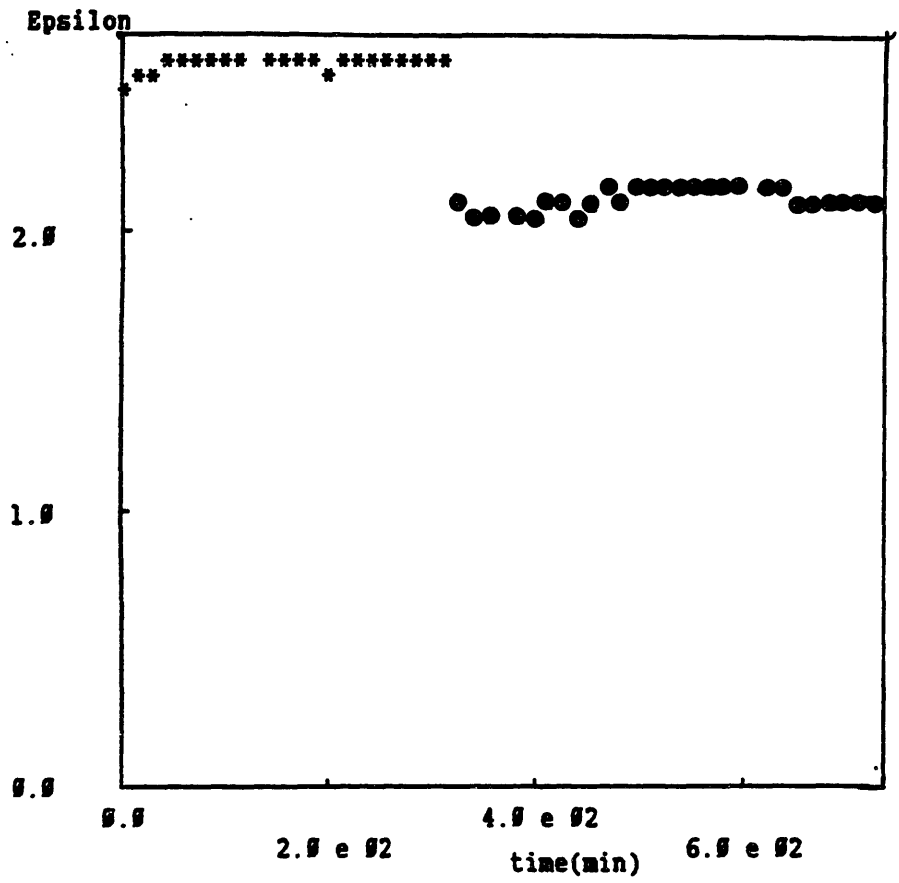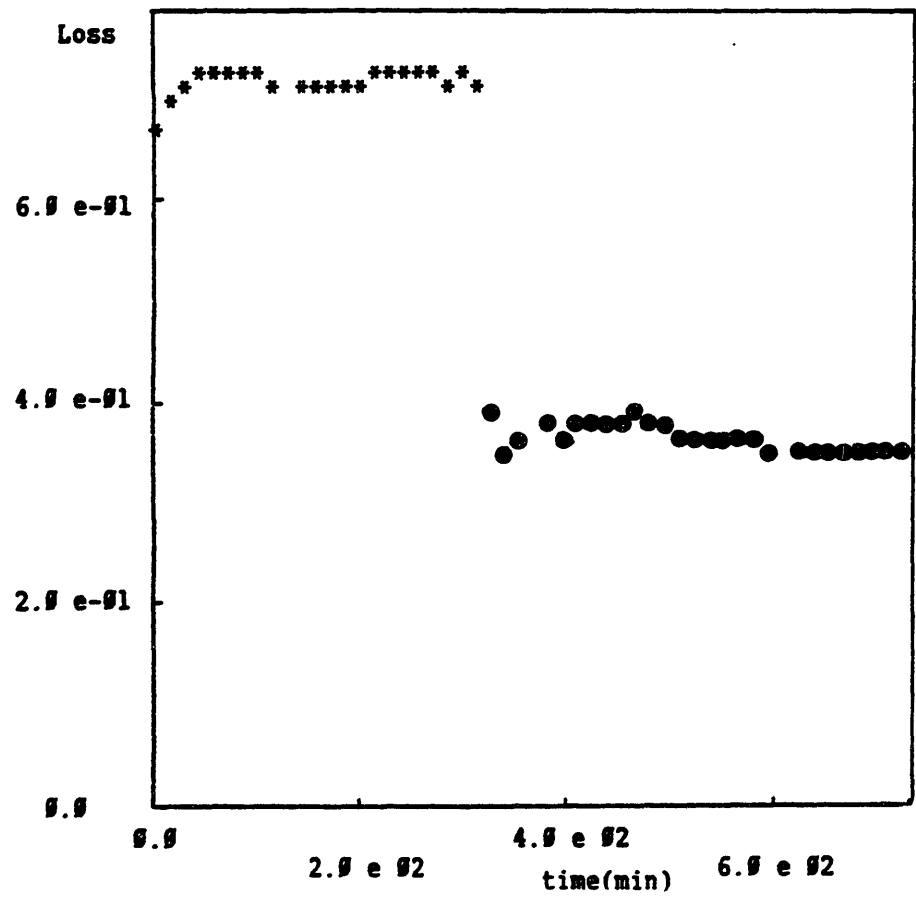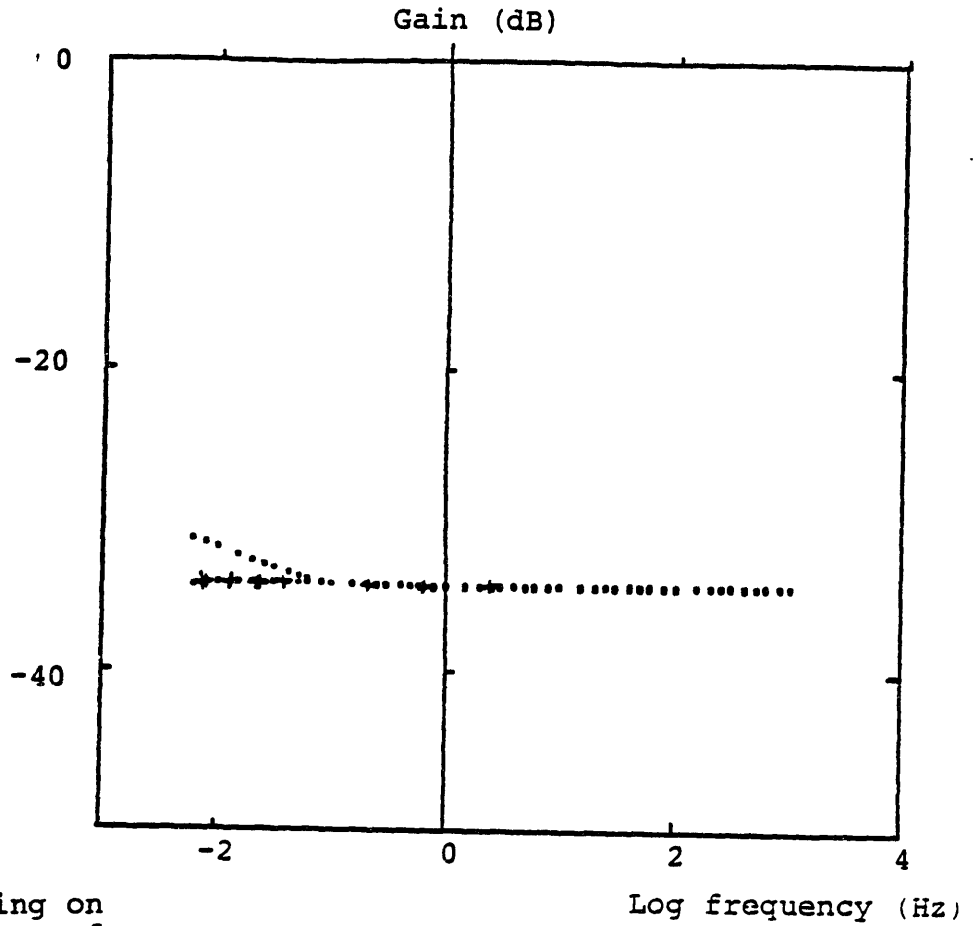
Figure 5.8a

Figure 5.8

Effect of stirring on
frequency response of
a clean oil sample.

+ indicate
    stirring

Figure 5.8b

Phase
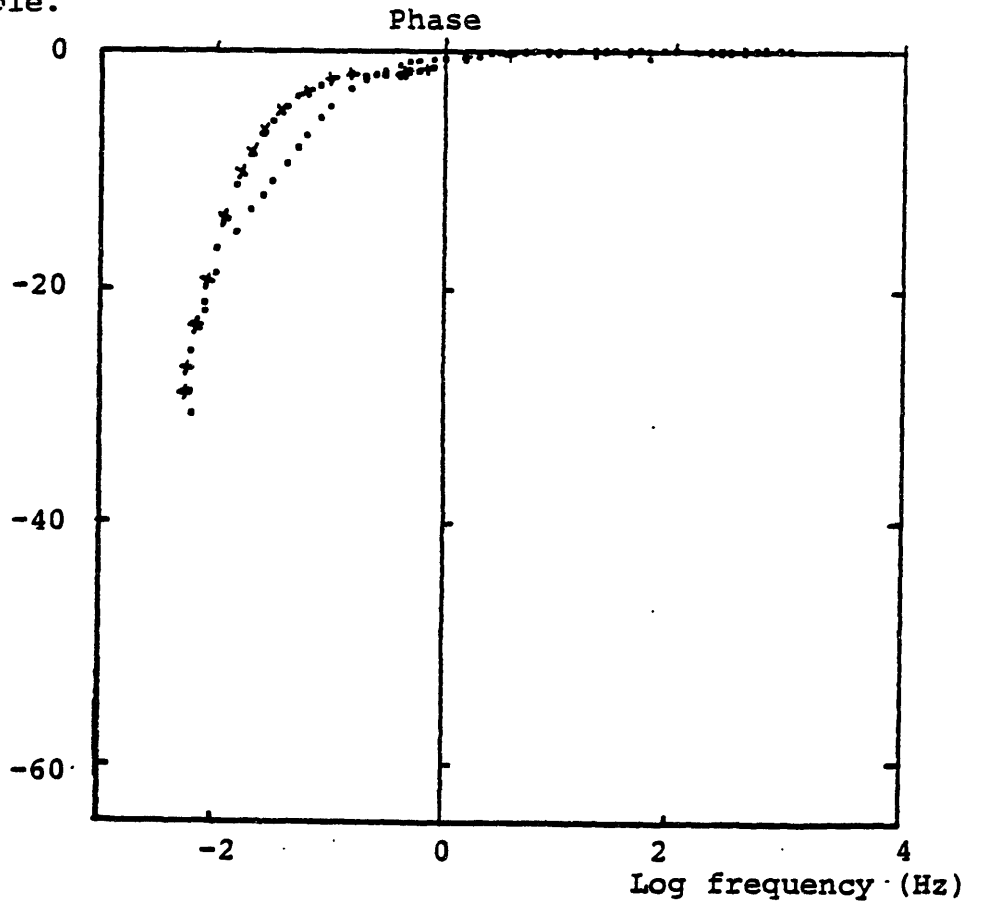
Log frequency (Hz)
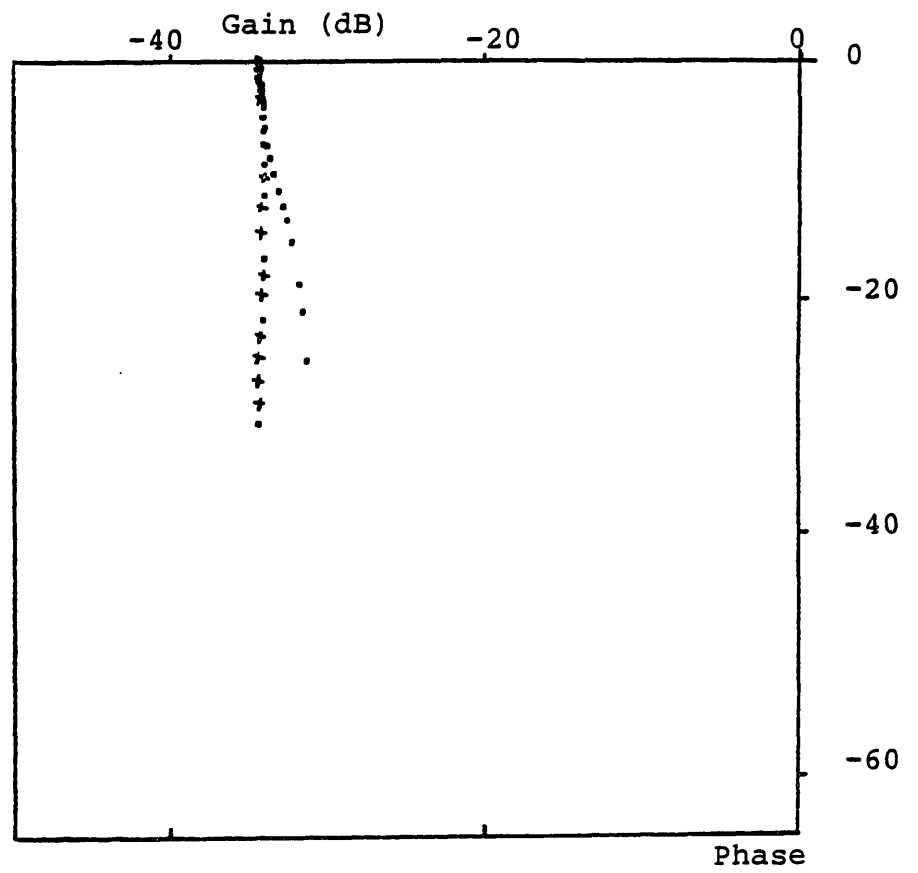
Figure 5.8c

Figure 5.8d
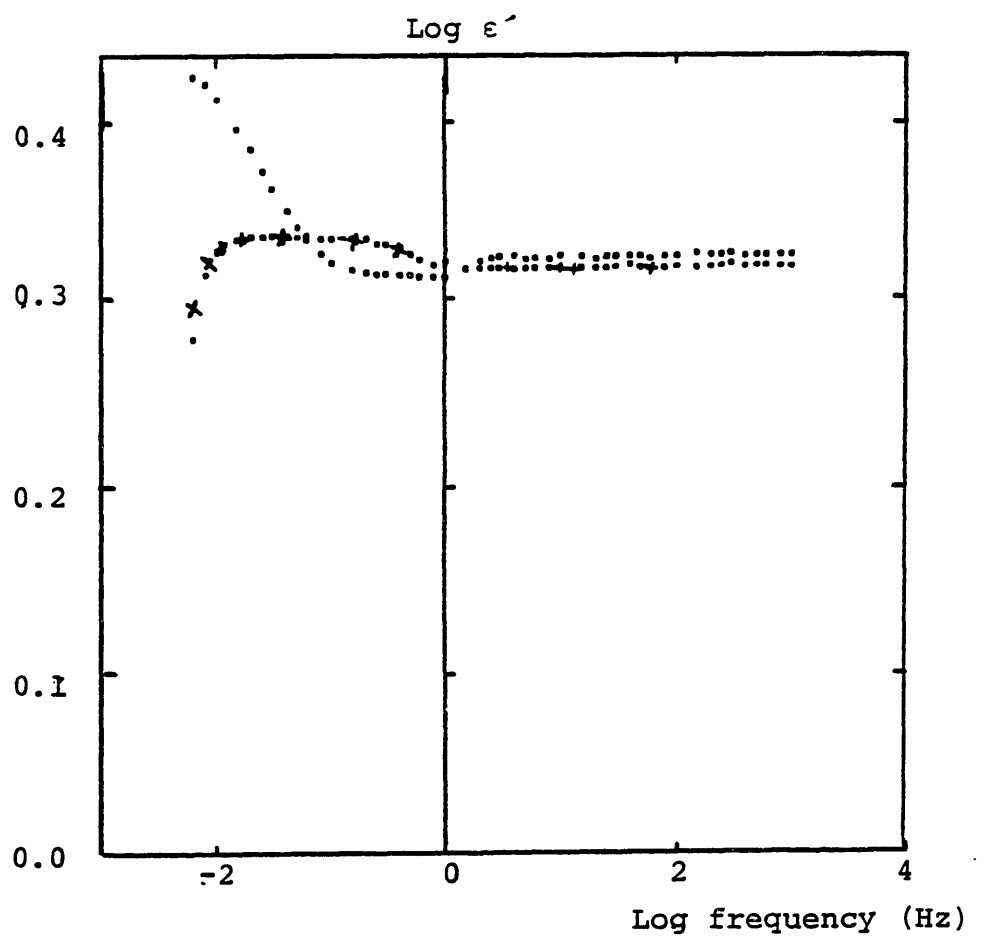
Figure 5.8e
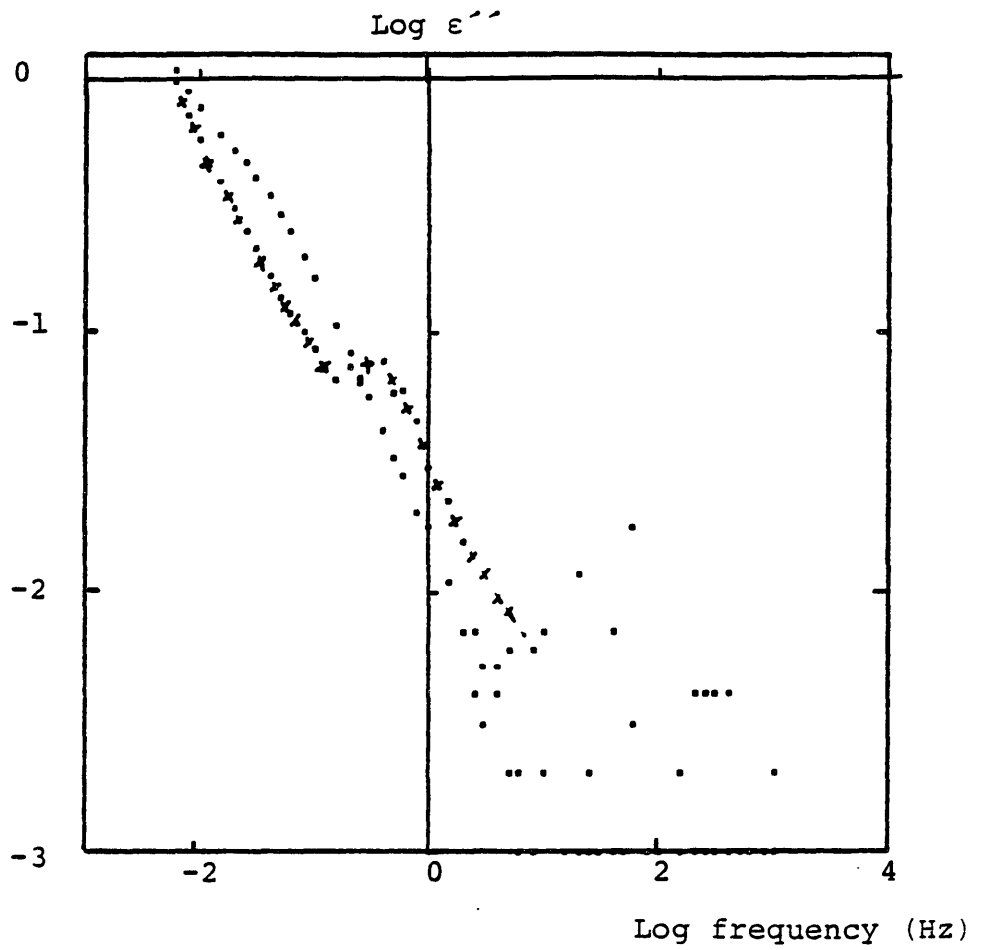
Figure 5.8f
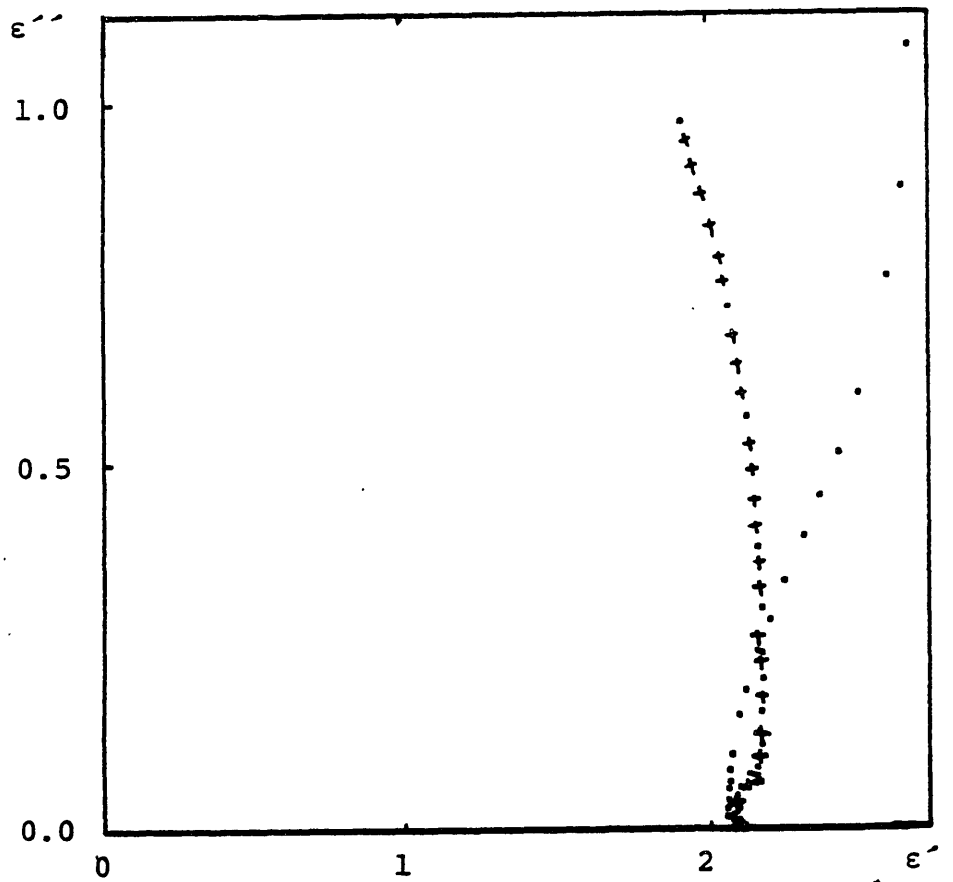
has a smaller radius.

The high frequency hump on the gain-phase plot is not apparent in figure 5.8c, but if the low gain tip is enlarged, a small hump appears for the stirred sample as shown in figure 5.9. No distinct hump was clear for the nonstirred sample.

The basic results presented in this section can be summerized as follows:

1) Fresh and reclaimed oil samples show similar response and close values of permittivity and loss.

2) The equivalent permittivity shows an increase at low frequencies, accompanied by a departure of the loss from the $\frac{1}{\omega}$ dependence. The high frequency permittivity agrees with a bridge measurement at 200 Hz.

3) The equivalent loss rises appreciably with time after the initial preparation of a sample.

4) The Cole-Cole plot has a two lobed shape, one with a smaller radius corresponding to the higher frequencies, and the second with the larger curvature corresponding to the lower frequencies. The radius of curvature of the high frequency semihalf circle decreases under the effect of stirring.

5) The gain-phase plot also has a general shape with

Gain(dB)

-35   -34   -33

Phase
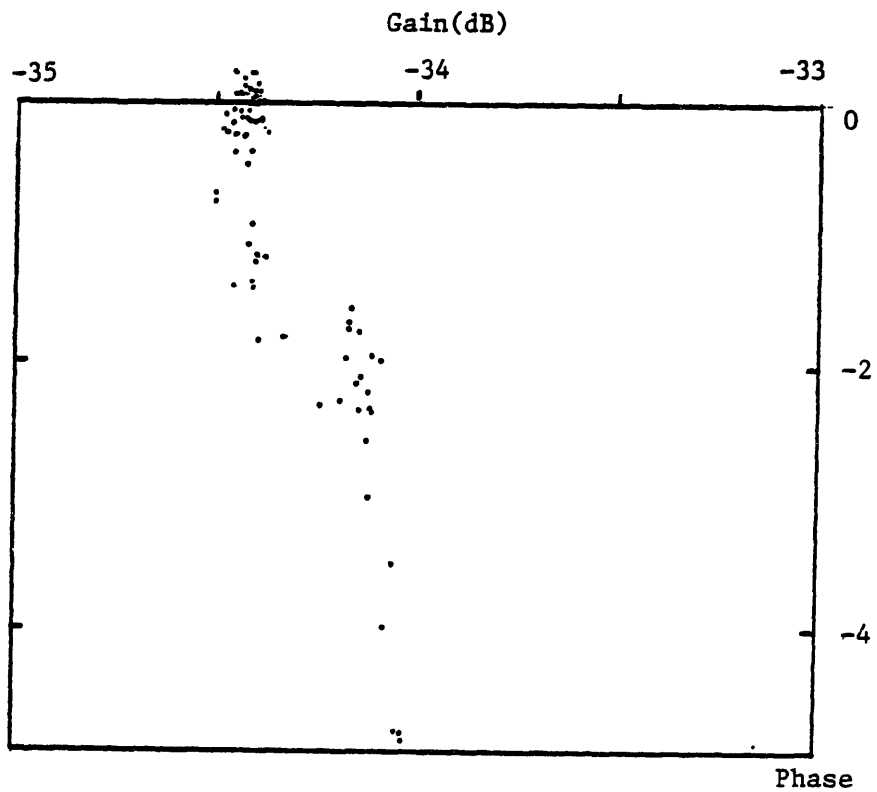
Figure 5.9

A magnified view of the high frequency response
of the stirred clean oil sample of figure 5.8

90

two humps. The transition between the two humps for measurements done while stirring the sample occurs at a higher frequency than for nonstirred measurements. The asymptotic value that the high frequency hump approaches before it follows the low frequency hump increases with an increase of the loss (measured at 1 Hz and higher frequencies). This asymptotic value decreases under the effect of stirring.

These findings combined with the results of experiments done on contaminated oil and described in the next section, are used to form a picture of the mechanisms causing dispertion in the equivalent permittivity and conductivity of the sample.

5.3 Contaminated Oil

The word contaminated is used to indicate both oil naturally contaminated from use in a failed transformer, and oil which has been contaminated with industrial additives to increase its conductivity. Samples of both types are studied. Using oil with an increased conductivity gives the opportunity to observe a more complete section of the gain phase curve, compared to oil with low conductivity. In the latter, even at the lowest frequency of .005, the ionic loss is small, and the corresponding gain is small as well.

5.3.1 Oil With High Water Content

An oil sample from a failed transformer and with a
water contents of 250 ppm was studied. The immediate
response at 1 Hz after the sensor is immersed in oil is
shown in figure 5.10. The initial slope of the equivalent
loss is .612/min (equivalent to 5.6 10^{-13} mho/m/sec). The
sample was sealed under a nitrogen ambient. Three frequency
scans within the first 48 hours are shown in figure 5.11.
The sample was not stirred during the measurements shown in
this figure. The response shows little stability with time.
The dual hump plot is apparent in two of the gain-phase
curves. The response at t=26 hours has an asymptote heading
towards a gain of -5 before the second hump of the
gain-phase plot starts. The breakpoint frequency is .03 Hz.
The response at t=30 min has a local maximum of the phase at
$\simeq$ 20 Hz, but the asymptote is not clear on the gain phase
curve. In the Cole-Cole plot shown in figure 5.11f the
details of the high frequency semihalf circle are not clear
because of the dimensions of the plot, the high frequency
portion of the plot is shown alone in figure 5.12, and the
small semihalf circle is more apparent. The permittivity was
still decreasing even at frequencies above 1 kHz, and the
permittivity at the highest available frequency of 10 kHz
varied between 2.86 at t=30 min and 3.13 at t=26 hrs, and
had a negative derivative with frequency. The equivalent
conductivity at 1 Hz varied between 1.6×10^{-10} mho/m at t=14
hrs and 8.3×10^{-10} mho/m at t=26 hrs. Clearly these values
for the equivalent conductivities are much larger than the
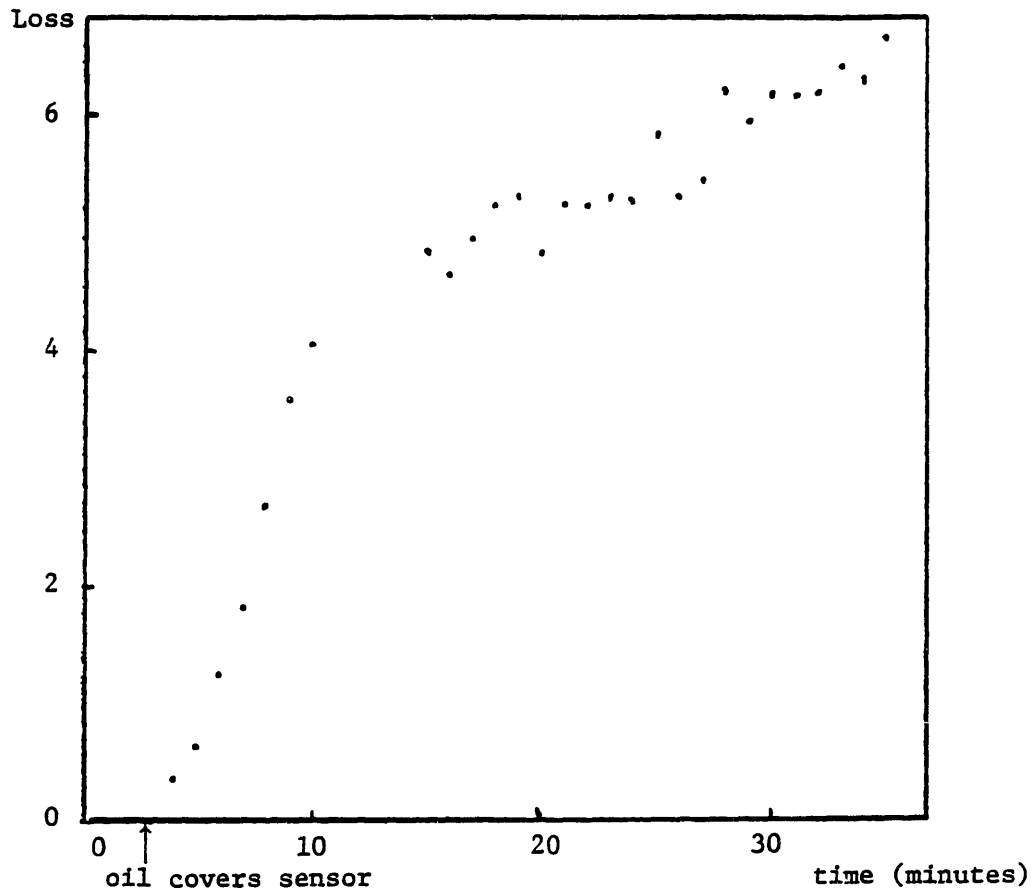
Figure 5.10

Initial equivalent loss at 1 Hz
of oil with a high water content.

Gain(dB)
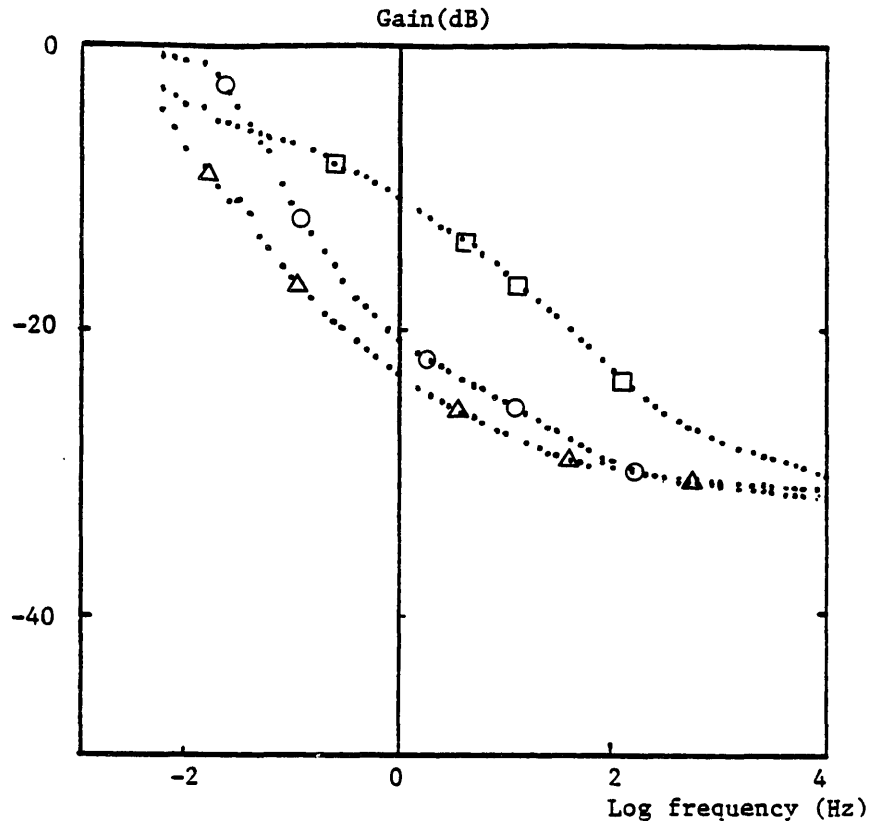
Figure 5.11a

Figure 5.11

Response of used oil
sample with a high
water content.

○ t= 30 minutes

△ t= 14 hours

□ t= 26 hours

Log frequency (Hz)

Phase

Figure 5.11b

Log frequency (Hz)

94

Figure 5.11c

Gain(dB)

Phase

Figure 5.11d

Log ε

Log frequency (Hz)

95
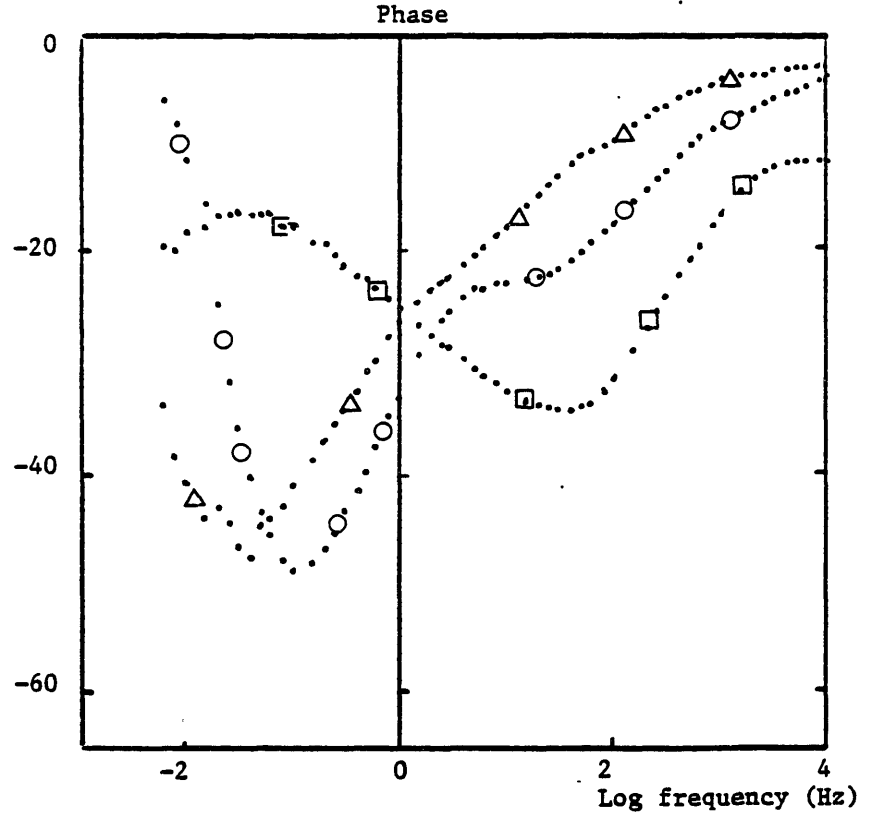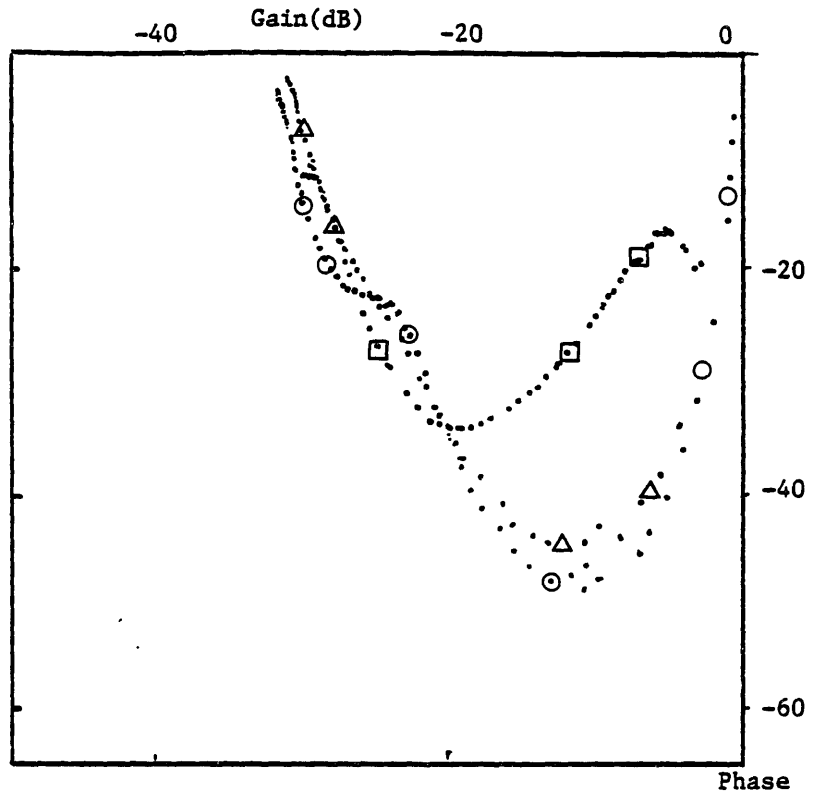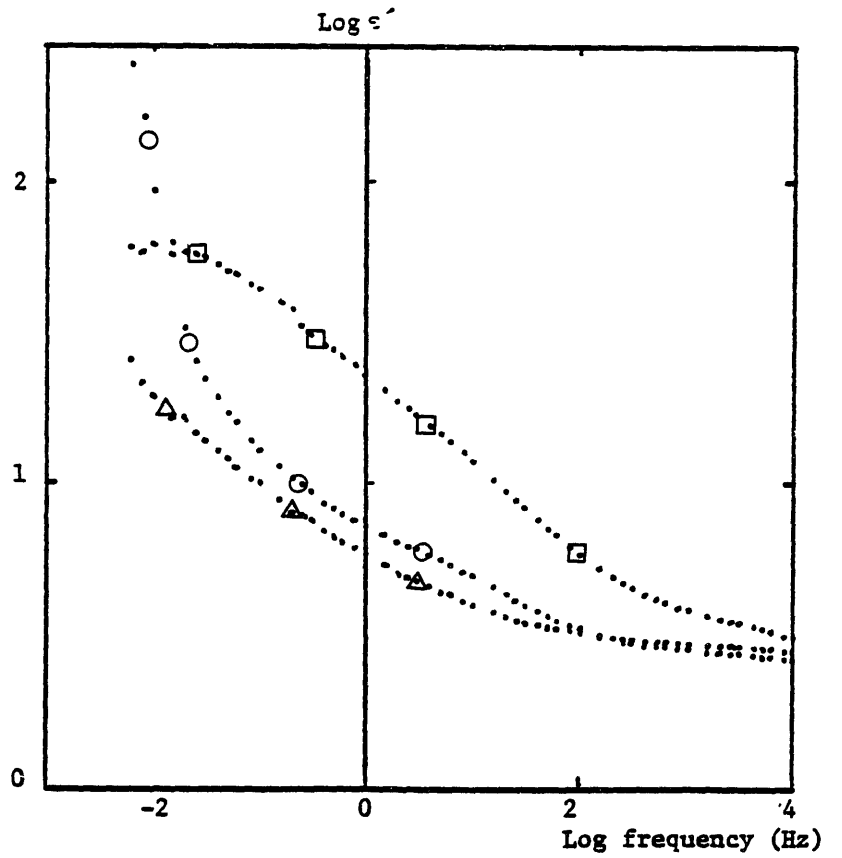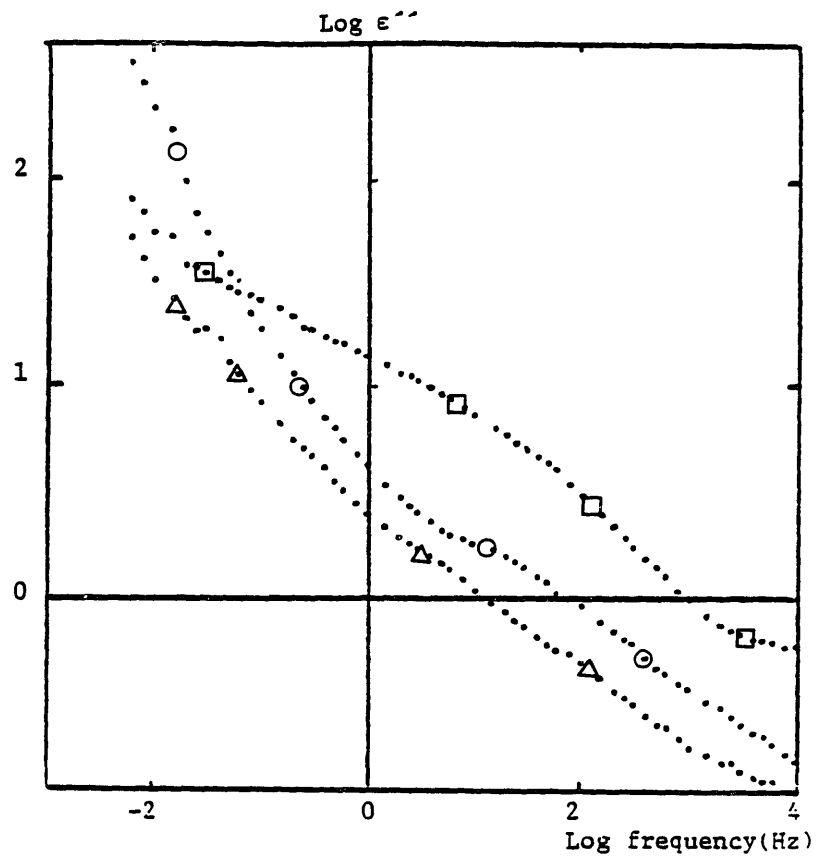
Figure 5.11e
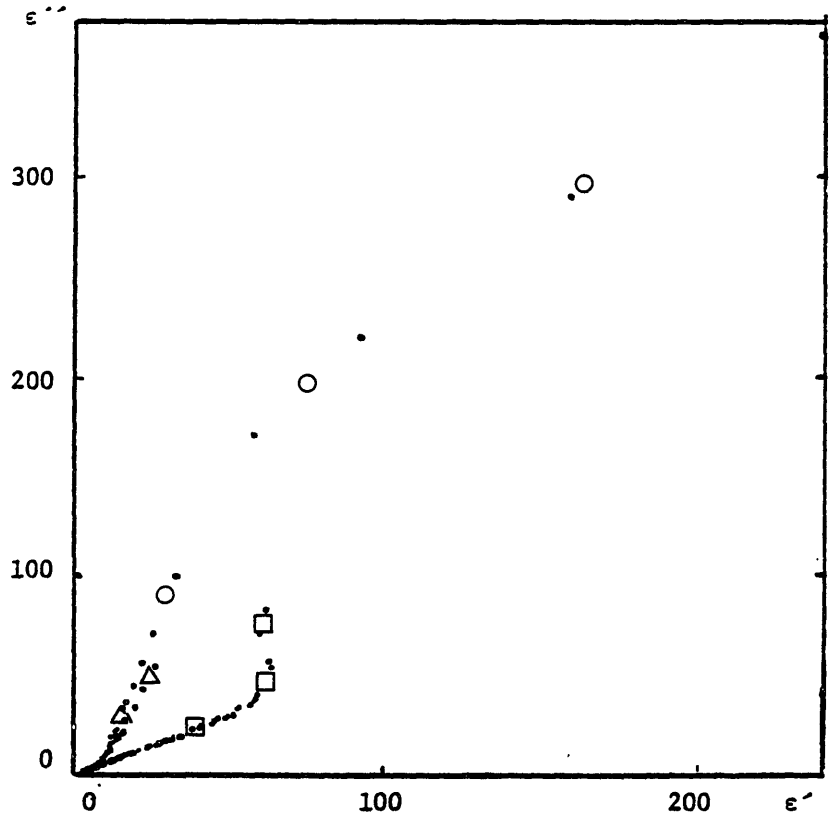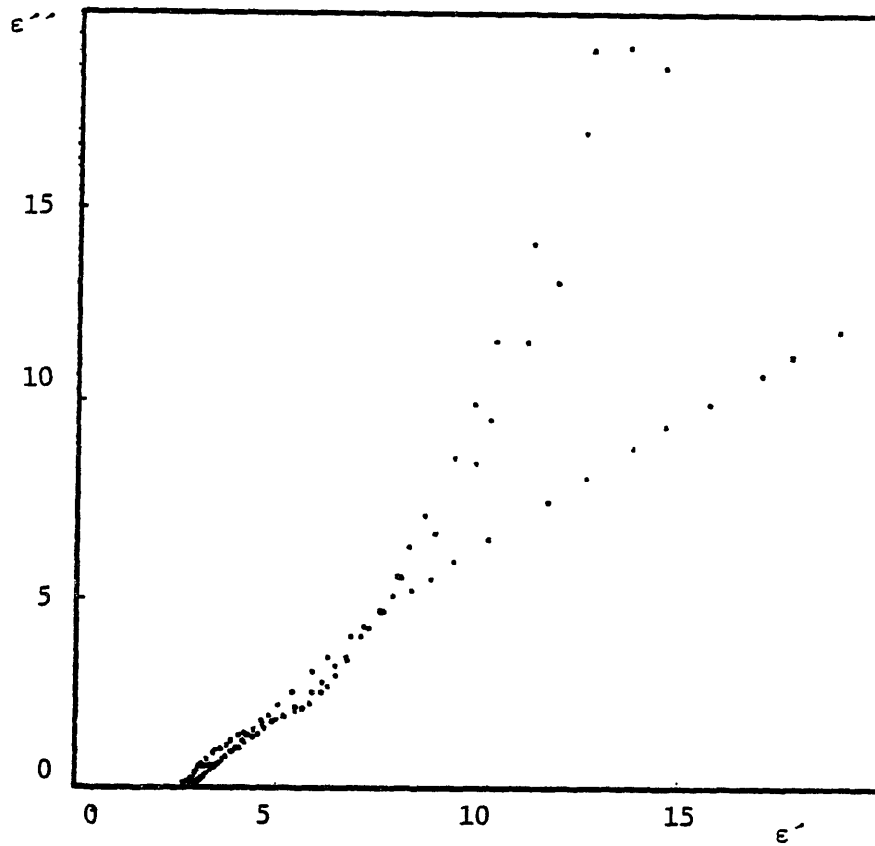
Figure 5.11f

Figure 5.12

High frequency end of the Cole-Cole plot
for oil sample with a high water content.

equivalent conductivities measured for clean oil under all the various situations. The large conductivity detected is attributed mostly to the high water contents in the oil.

A sample of the same contaminated oil was dried by bubbling dry nitrogen through it for few hours. Measurements were done on the dried sample, and results are shown in figure 5.13. The loss measured has decreased for all frequencies, and the equivalent conductivity at 1 Hz is 9.3×10^{-12} mho/m. The permittivity for the dried sample reaches its high frequency limit of 2.0 for frequencies higher than .5 Hz. The local maxima of the phase occurs around .02 Hz. The radius of the high frequency semihalf circle is smaller for the dried sample than for the sample with high water contents.

Basic results of experiments on oil with high water contents are summerized below:

1) Measurements are unstable, but show loss values much larger than those observed for pure and reclaimed oil.

2) Water plays an essential role in increasing the measured loss values, as was demonstrated by drying the sample.

5.3.2 Oil With Additives

An antistatic agent is added to oil of commercial purity. The additive used is ASA-3 [37], a product of Shell.

Figure 5.13a

Gain(dB)
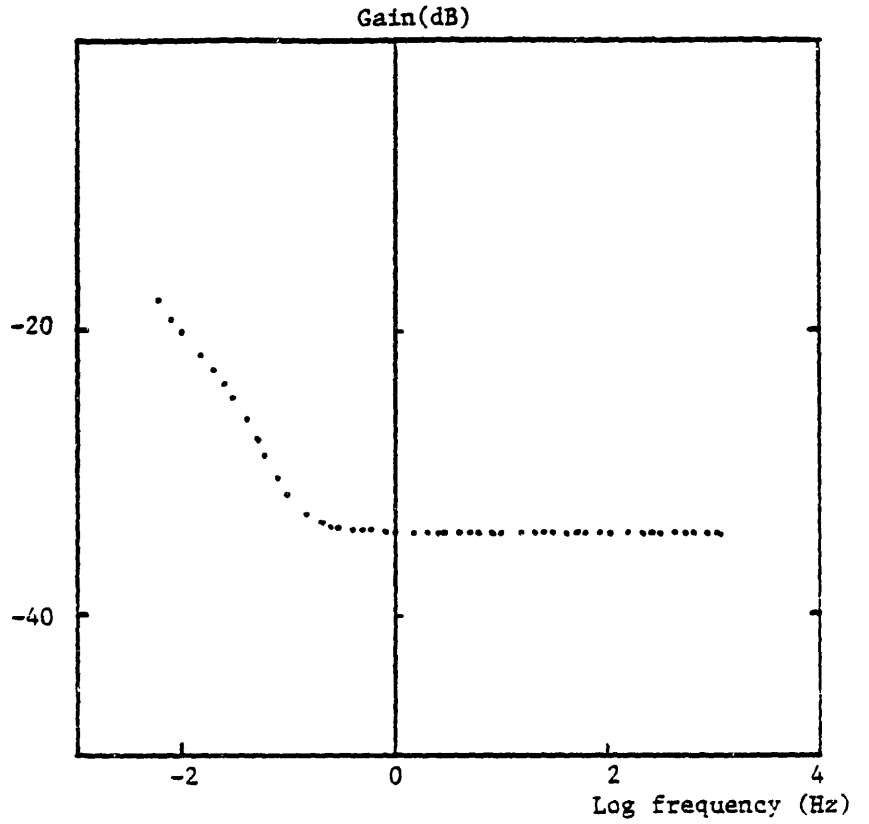
Figure 5.13

Response of a used
oil sample after it was
dried in nitrogen flow.

Log frequency (Hz)

Figure 5.13b

Phase

Log frequency (Hz)
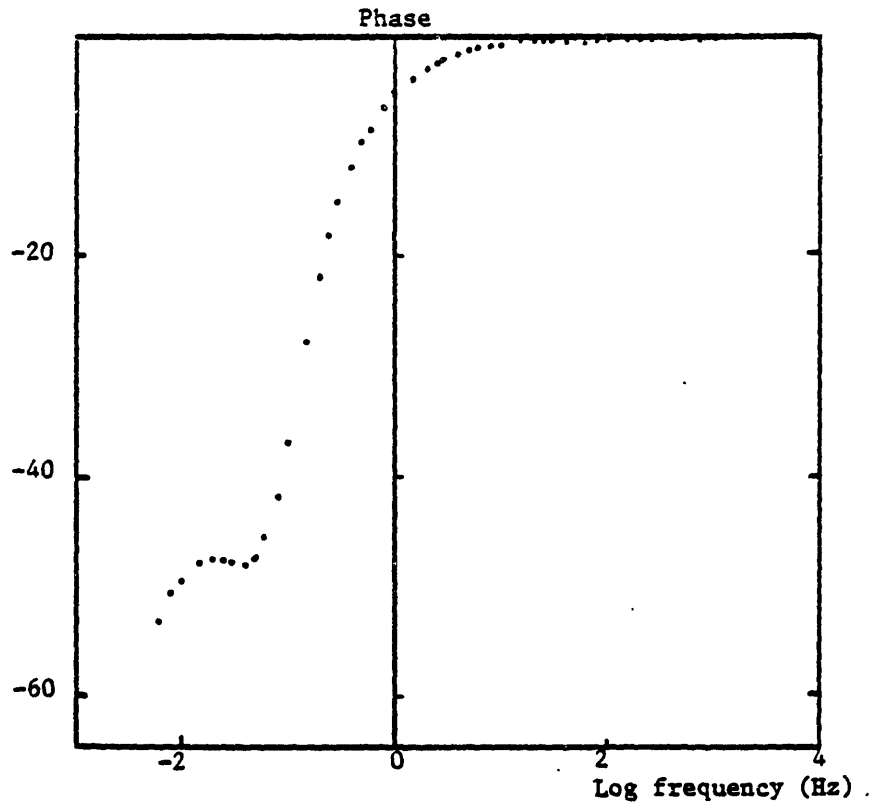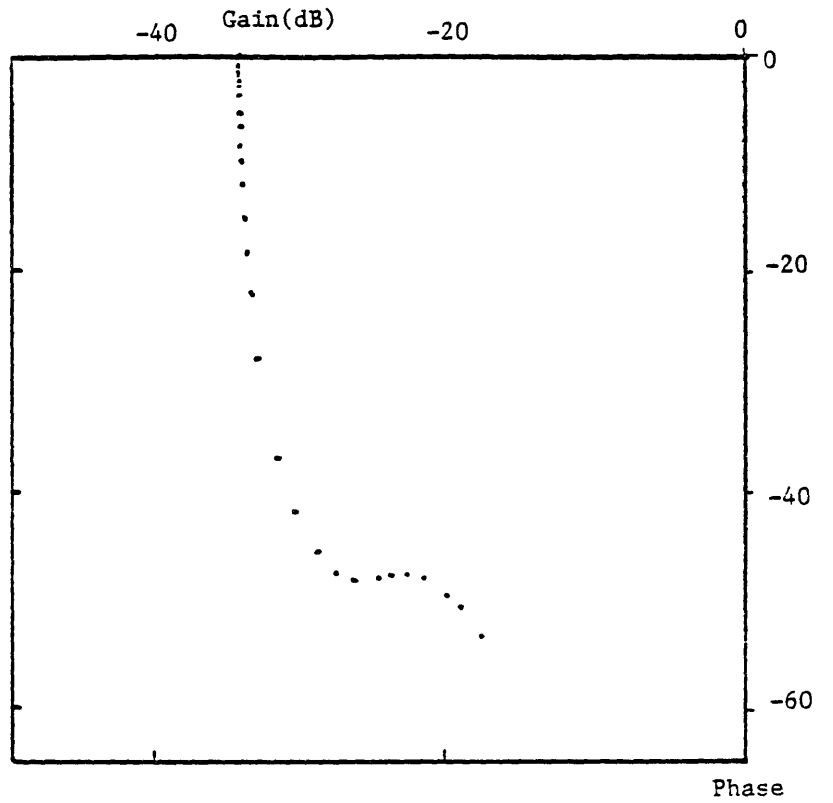
Figure 5.13c

Figure 5.13d

Figure 5.13e

Log ε´´

Log frequency (Hz)

Figure 5.13f

ε´´

ε´
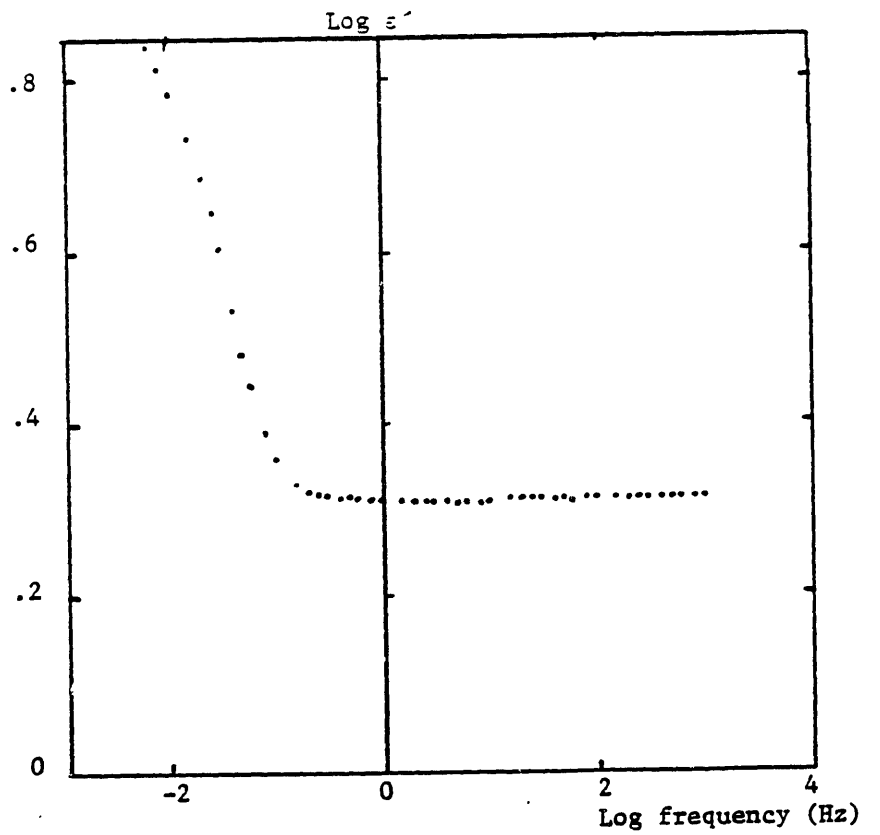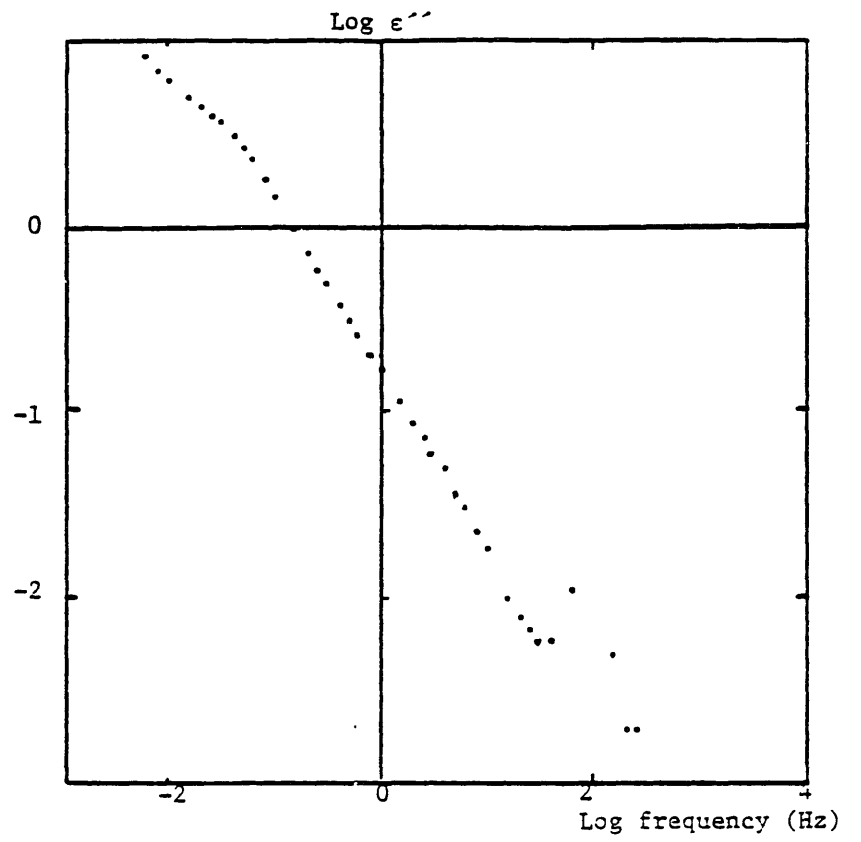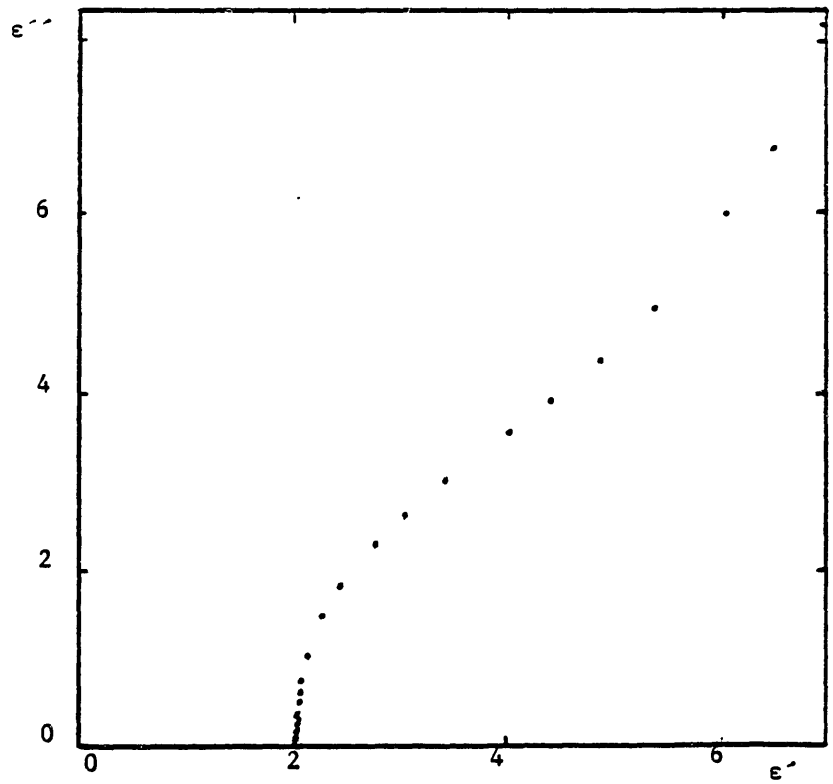
Two samples with different concentrations of ASA-3 were studied.

One sample was prepared with a concentration of .5 ppm. The permittivity of the sample using the radio bridge measurement was found to be 2.26 at 200 Hz. The conductivity was on the edge of the sensitivity of the bridge and was found to be $\simeq 4 \times 10^{-11}$ mho/m. The immediate response at 1 Hz after the sensor is immersed in oil is shown in figure 5.14. The initial slope of the loss is .014/min, or an equivalent slope for the apparent conductivity of 1.3×10^{-14} mho/m-sec. Figure 5.15 shows the response of this sample with and without stirring. The high frequency permittivity for both stirring and non stirring is 2.3 and is in good agreement with the bridge measurement. The conductivity at 1 Hz is $\simeq 10^{-10}$, about twice the conductivity measured by the bridge. The loss vs frequency as shown in figure 5.15e has a slope of -1 for frequencies above above 1 Hz. and below 10 Hz. The higher frequency departure from the ideal slope is caused by the increase of the level of the noise relative to the response signal as was mentioned in section 5.2. For the stirred sample, deviation starts at about 1 Hz, while the -1 slope continues for the nonstirred sample till .15 Hz. The radius of the high frequency semihalf circle is again smaller for measurements done with stirring.

A second sample was prepared with a concentration of 50 ppm of ASA-3. The bridge measurements of the conductivity and permittivity of the sample at 200 Hz were respectively
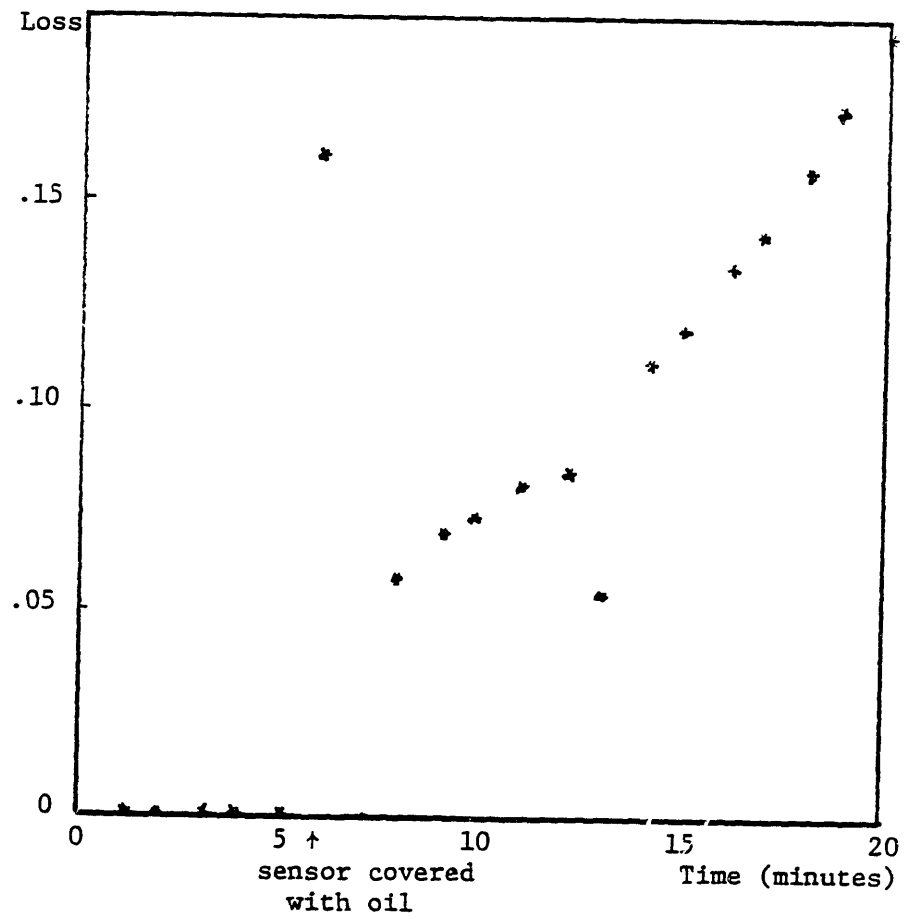
Figure 5.14

Initial equivalent loss at 1 Hz
of oil sample with 0.5 ppm of ASA-3.

Figure 5.15a
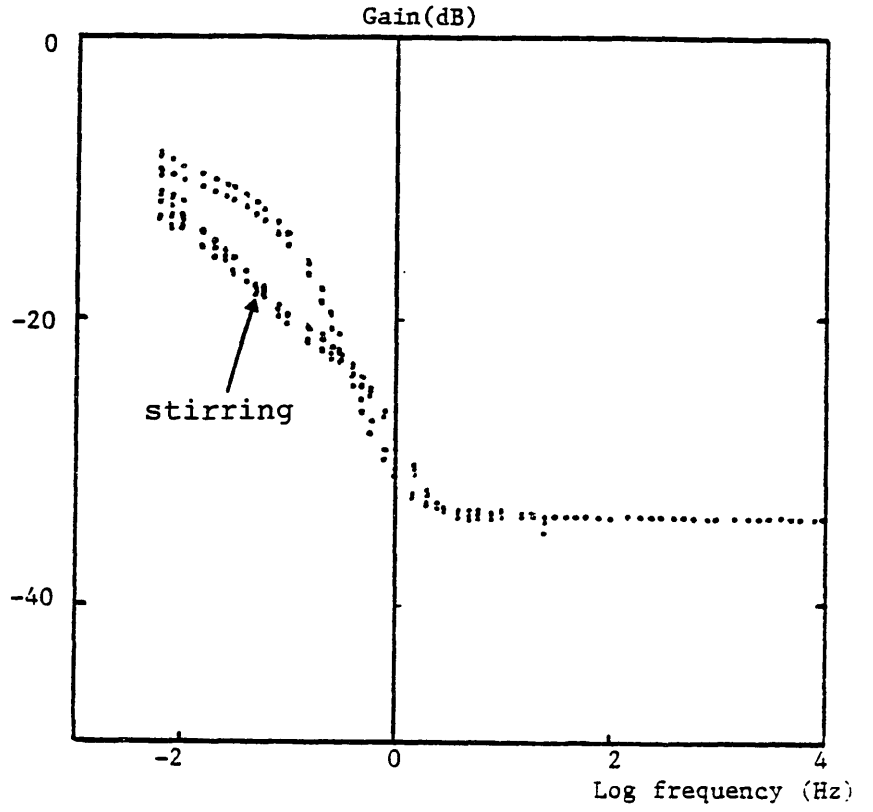
Figure 5.15

Response of oil with
0.5 ppm of ASA-3.

Gain(dB)

stirring

Log frequency (Hz)

Figure 5.15b

Phase

stirring

Log frequency (Hz)

104
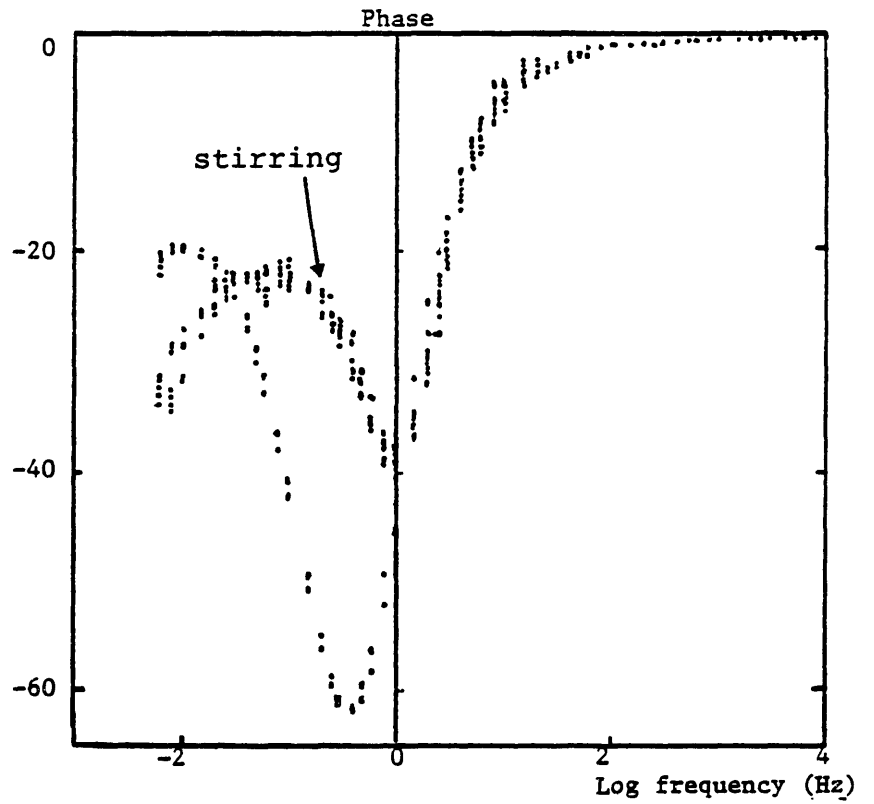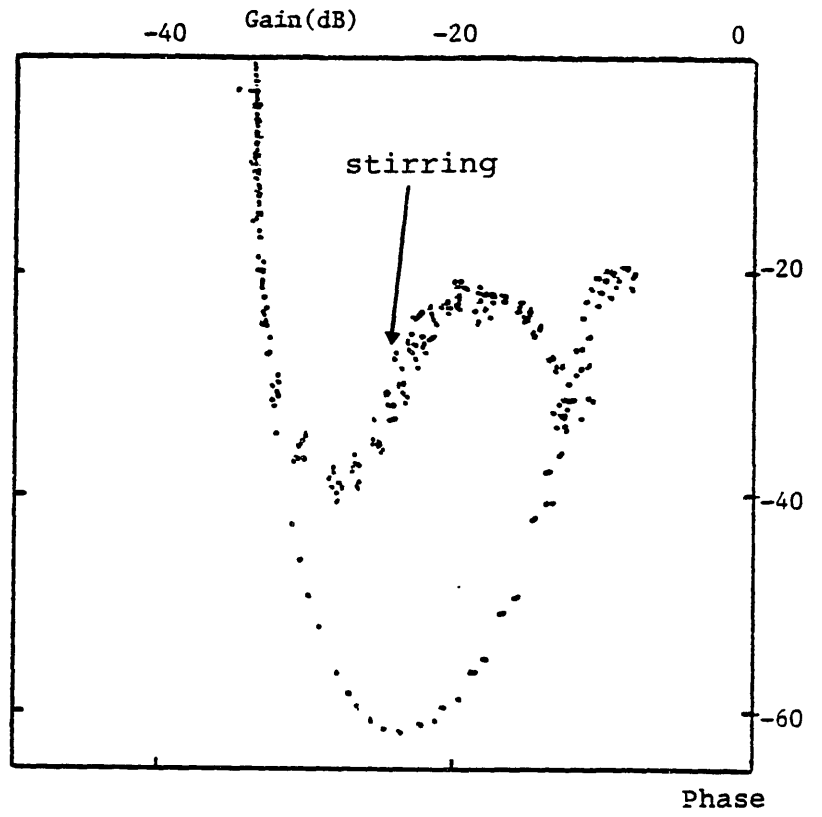
Figure 5.15c
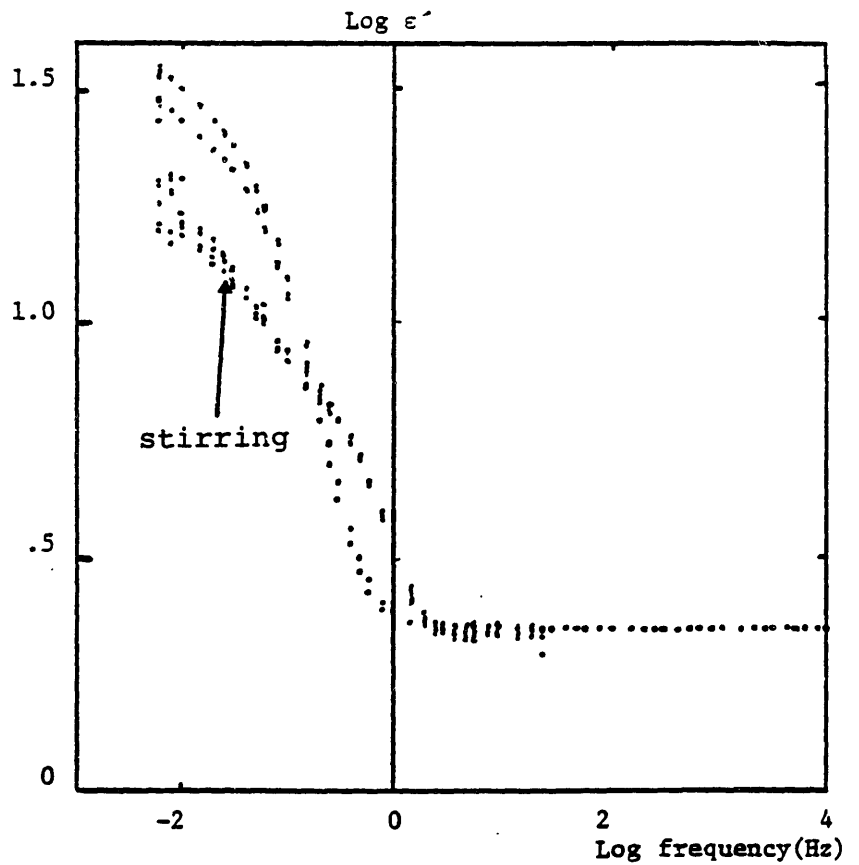
Figure 5.15d

Figure 5.15e
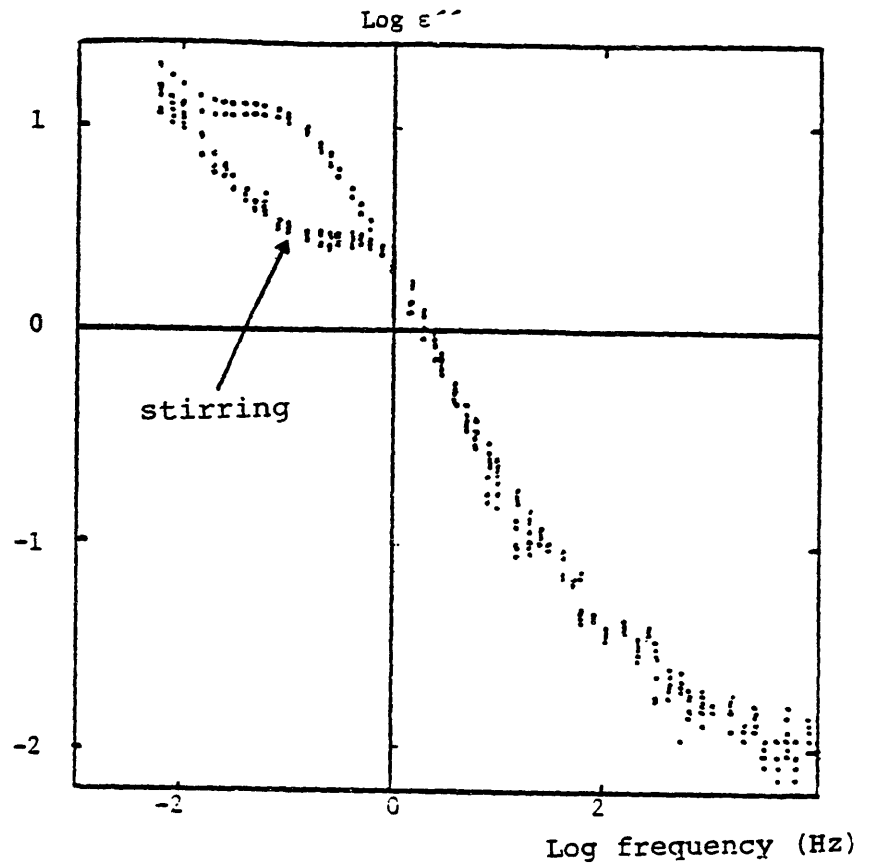
Figure 5.15f
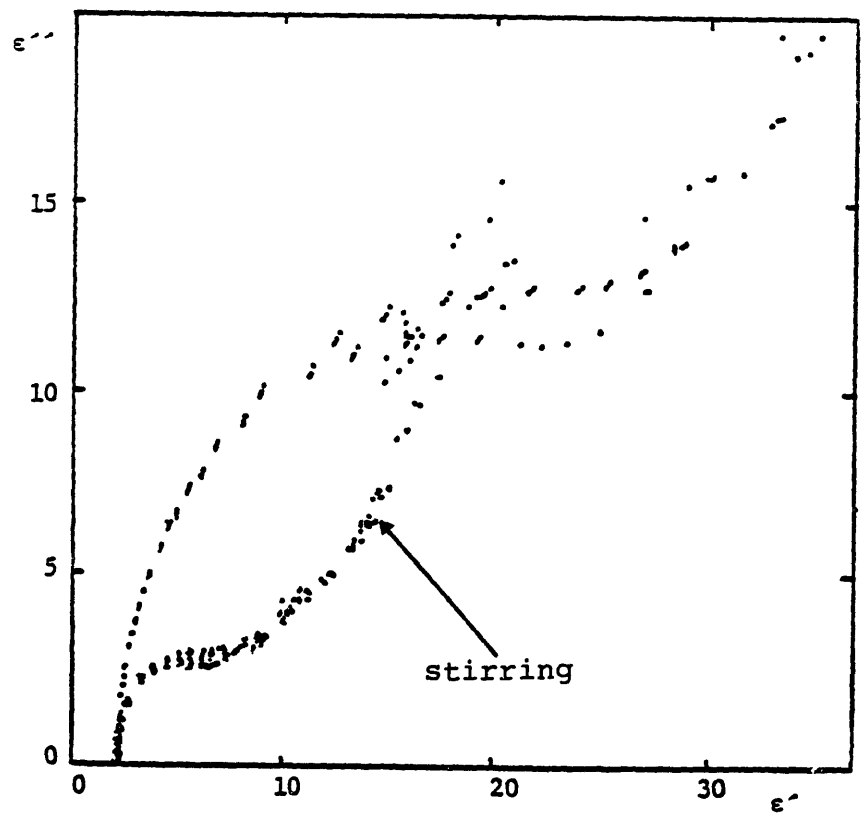
10^{-9} mho/m and 2.25. The initial response as the sensor is immersed in oil is shown in figure 5.16. The initial slope of the loss at 1 Hz is 1.5/min , or equivalently 1.4×10^{-12} mho/m/sec. The frequency response under stirring and non stirring conditions is shown in figure 5.17. The high frequency permittivity is 2.2 for both cases, and the conductivity at 1 Hz is $\simeq 2 \times 10^{-9}$ mho/m. The Cole-Cole plot again shows a smaller semihalf circle for measurements done with stirring. The gain-phase plot does not show clearly the difference between the stirred and nonstirred case, but a close look at the low frequency end with very small gains as shown in figure 5.18 demonstrates the difference. The asymptotic gains for the stirred and nonstirred measurements are -2.2 and -1.9 respectively.

The experimental results in this section can be summerized as follows:

1) The sample with higher concentration has a larger high frequency semi half circle and larger asymptotic gain value.

2) Stirring reduces the radius of the semihalf circle and the asymptotic gain values.

The stirring trends are the same as noted for the pure oil in section 5.2. This similarity points to a common cause for the low frequency dispersion of the measured permittivity and conductivity.
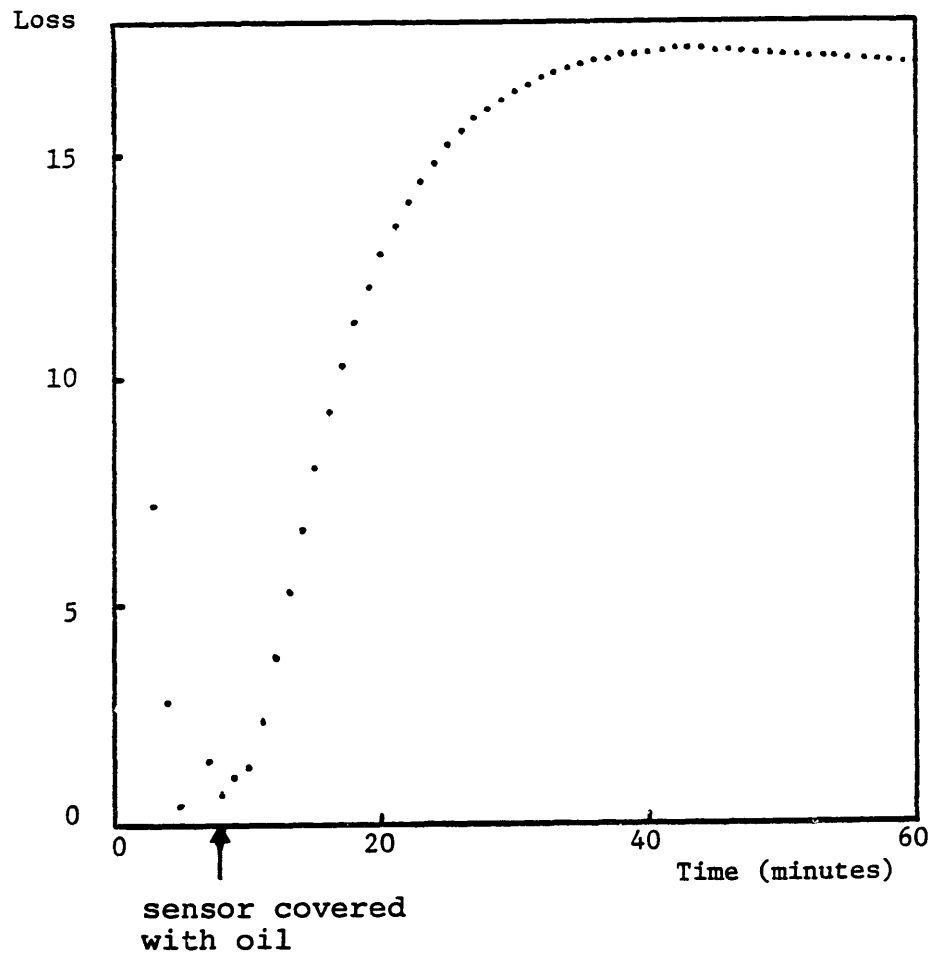
Figure 5.16

Initial equivalent loss at 1 Hz
for oil sample with 50 ppm ASA-3.

Gain(dB)

Figure 5.17a

Figure 5.17

Response of oil
sample with 50 ppm
ASA - 3

Figure 5.17b

Phase

Gain(dB)

Figure 5.17c

Phase

Log ε´

Figure 5.17d

stirring

Log frequency (Hz)

110
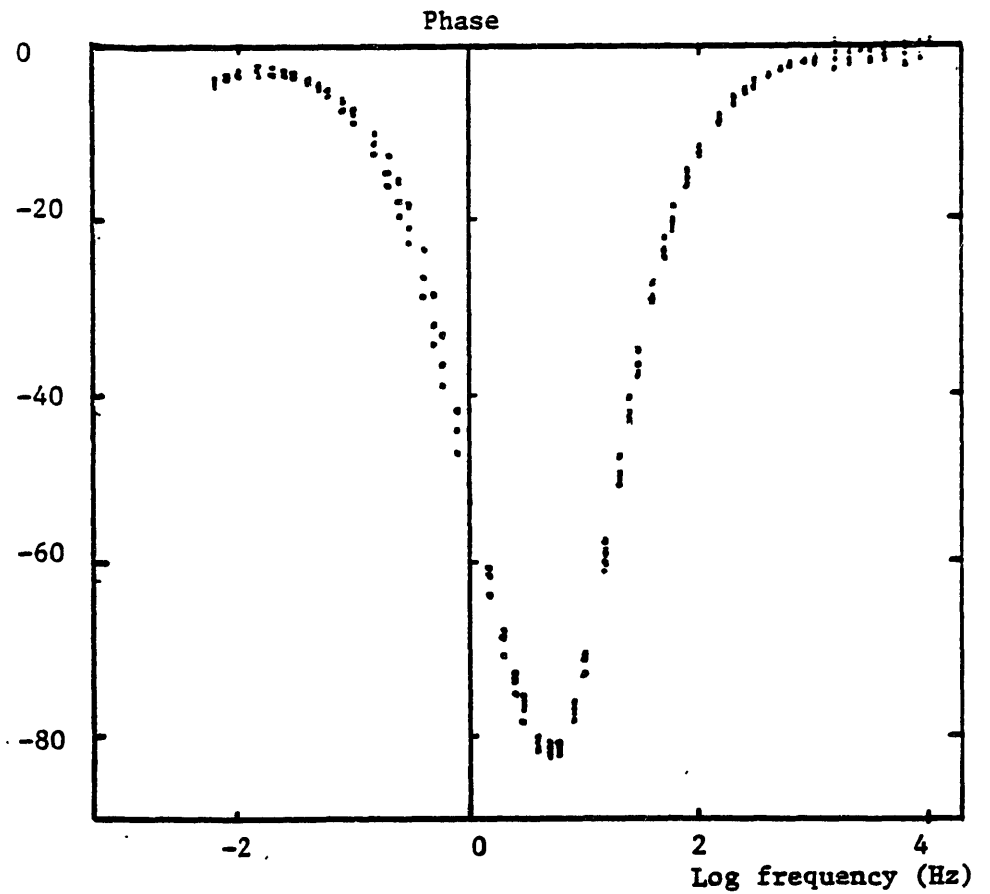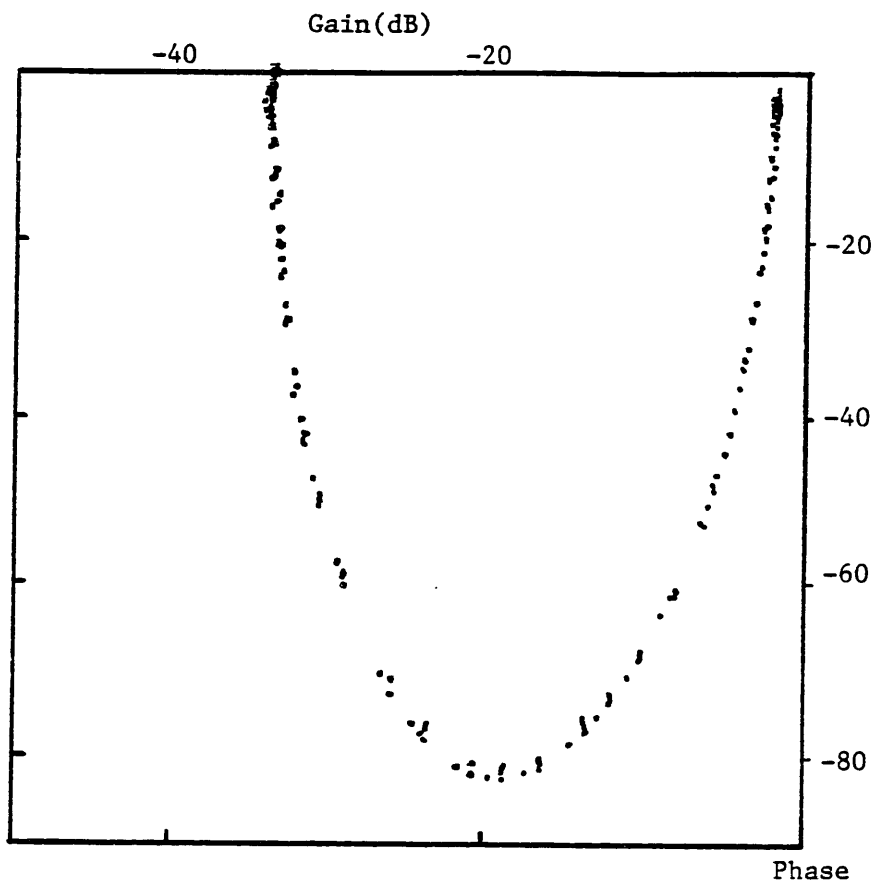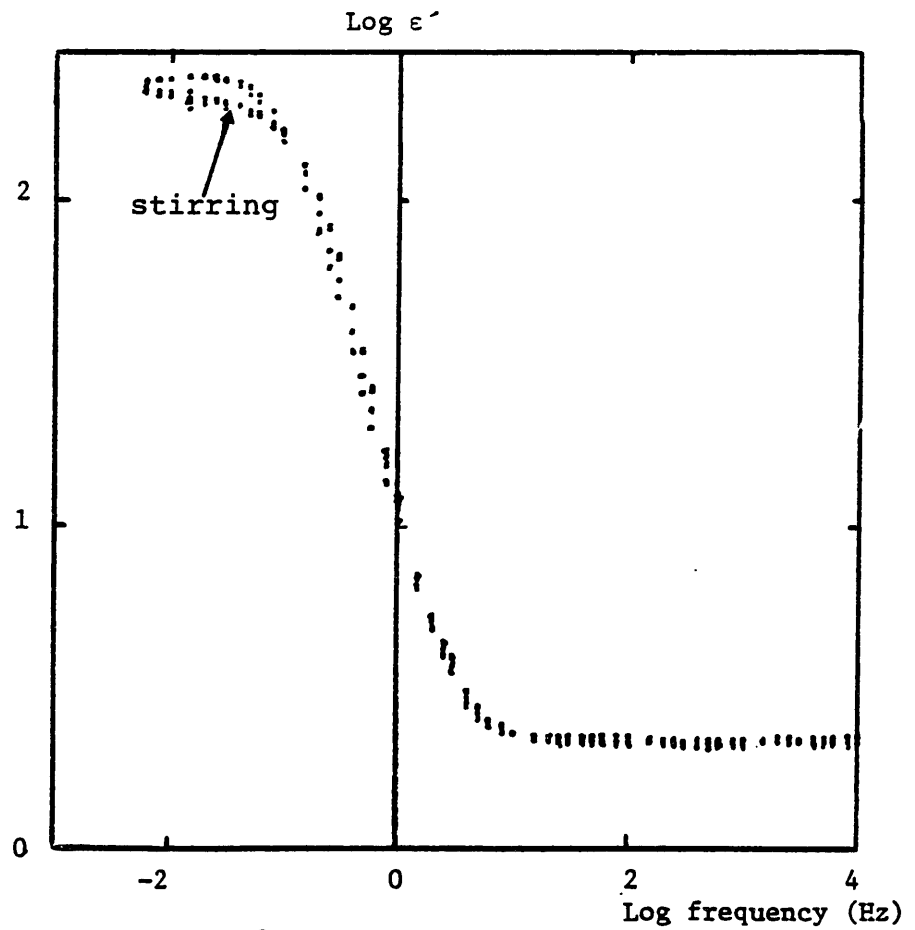
Figure 5.17e

Figure 5.17f

111
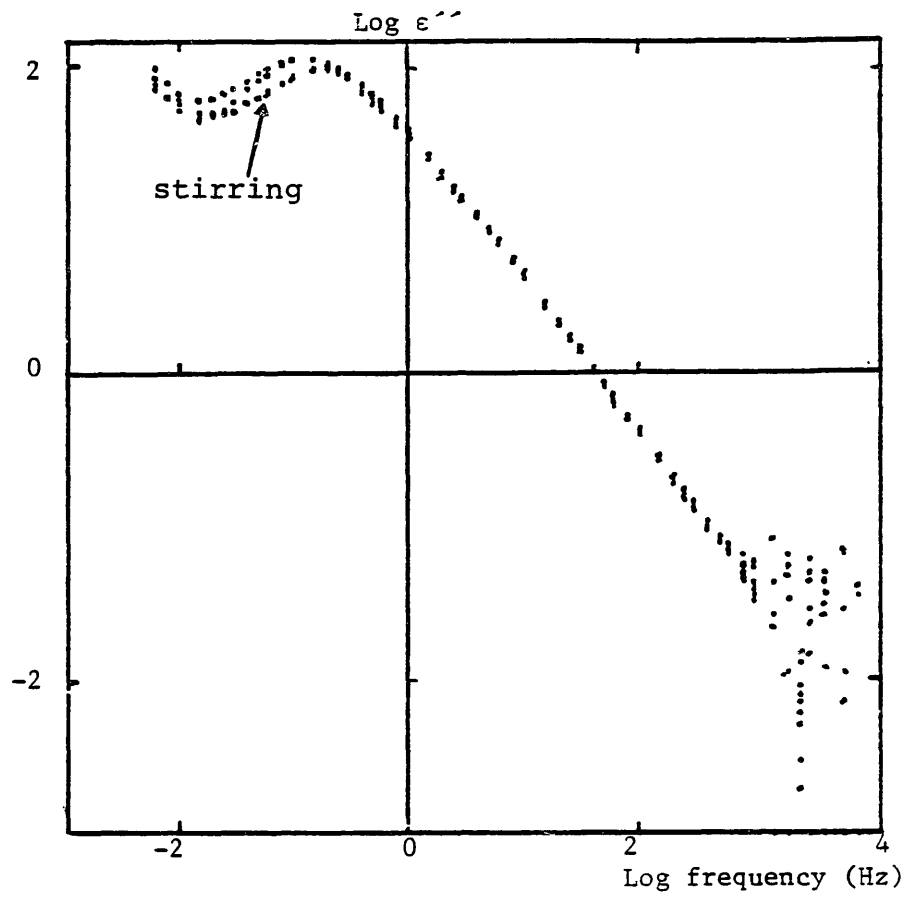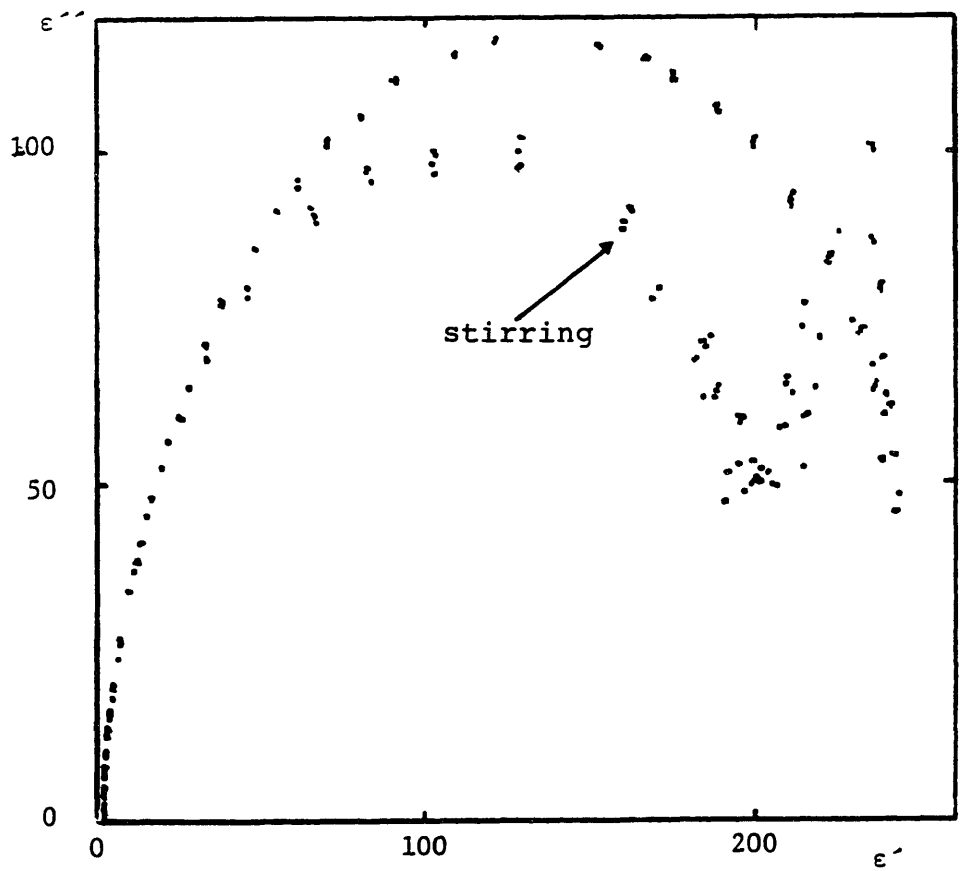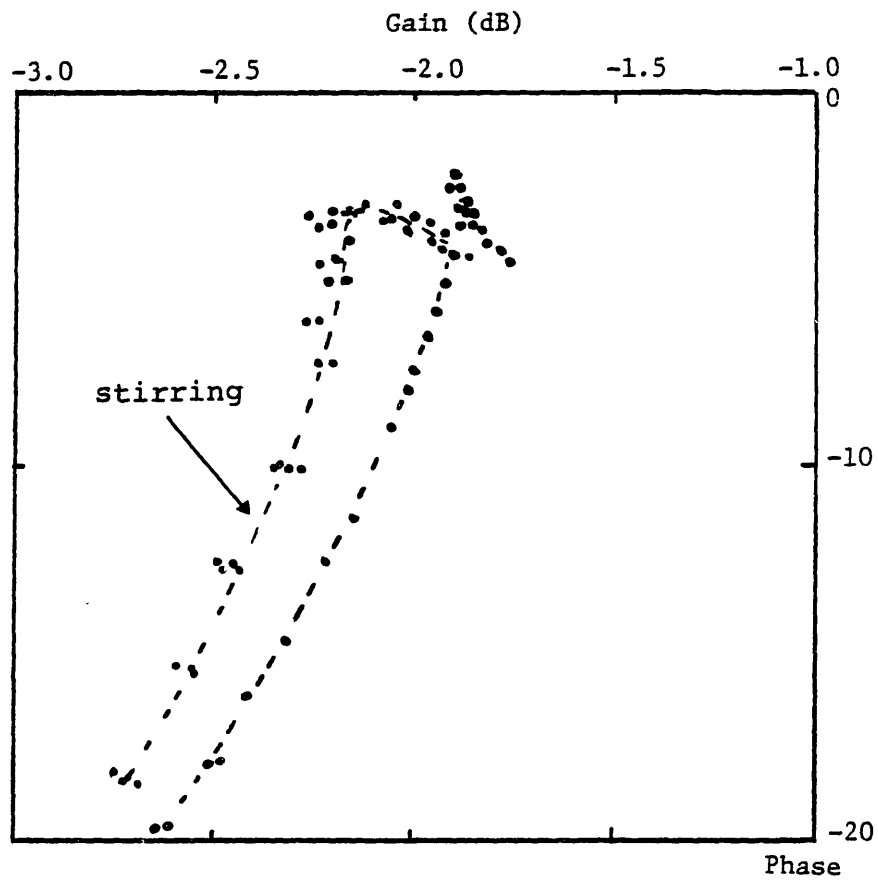
Figure 5.18

Magnified view of the low frequency end of
the response of oil sample with 50 ppm ASA-3
shown in figure 5.17

Chapter VI

Analysis of Results

Experimental results from the previous chapter show that the response of the sensor does not correspond to a uniform ohmic medium above the sensor. Dispersion of the bulk parameters as caused by hindered molecular rotation is eliminated as possible cause of the dispersion because of the frequencies involved. As was discussed in chapter two, the time constants in hindered rotations are on the order of 10^{-7} sec.

Surface phenomena at the sensor/liquid interface are the cause of this dispersion. As was discussed in chapter two, space charge accumulates at solid/liquid interfaces, and polarizes such interfaces at low frequencies.

Surface phenomena are often described in terms of equivalent circuit parameters [38]. The equivalent circuit can be quite complex depending on the variety of phenomena involved. These can include space charge polarization, as well as other phenomena such as crystallization, or electrochemical reaction [39]. The equivalent parameters help in identifying the surface phenomena involved.

In this chapter, lumped parameters are used to analyze experimental results described in chapter five. Variations of the parameters with conductivity, motion, and frequency is discussed. The surface phenomena affecting the experimental measurements are identified.

6.1 Surface Effects Charaterized by Lumped Elements

The observed Cole-Cole plots presented in the previous chapter suggest an equivalent circuit between the two electrodes as shown in figure 6.1. The elements C_{12} and G_{12} are assumed to be the bulk conductance and capacitance. The series capacitance C_s can explain the half circle on the Cole-Cole plot. However, the departure from this half circle to follow a secondary path (assumed to be perpendicular to the permittivity axis) indicates a parallel conductance path through G_p.

Measuring in essence an equivalent impedance, the sensor measures an effective permittivity and loss as defined below.

$$\varepsilon' = \frac{1}{\omega} \, \text{Real}\{Y_{eq}\}$$

$$\varepsilon'' = \frac{1}{\omega} \, \text{Imag}\{-Y_{eq}\} \tag{37}$$

Relating ε' and ε'' to the circuit elements, we get:

$$\varepsilon' = C_s \frac{(C_{12}C_s + C_{12}^2)\omega^2 + G_{12}}{(C_s + C_{12})^2 \omega^2 + G_{12}^2}$$

$$\varepsilon'' = \frac{1}{\omega} \left[\frac{\omega^2 (G_{12}C_s^2 + G_p(C_s + C_{12})^2) + G_p G_{12}}{(C_s + C_{12})^2 \omega^2 + G_{12}^2} \right]$$

This model predicts the general shape of observed Cole-Cole plots. Figure 6.2 shows the fitted Cole-Cole plot for the response of oil with 50ppm of antistatic agent (presented earlier in figure 5.7.f).
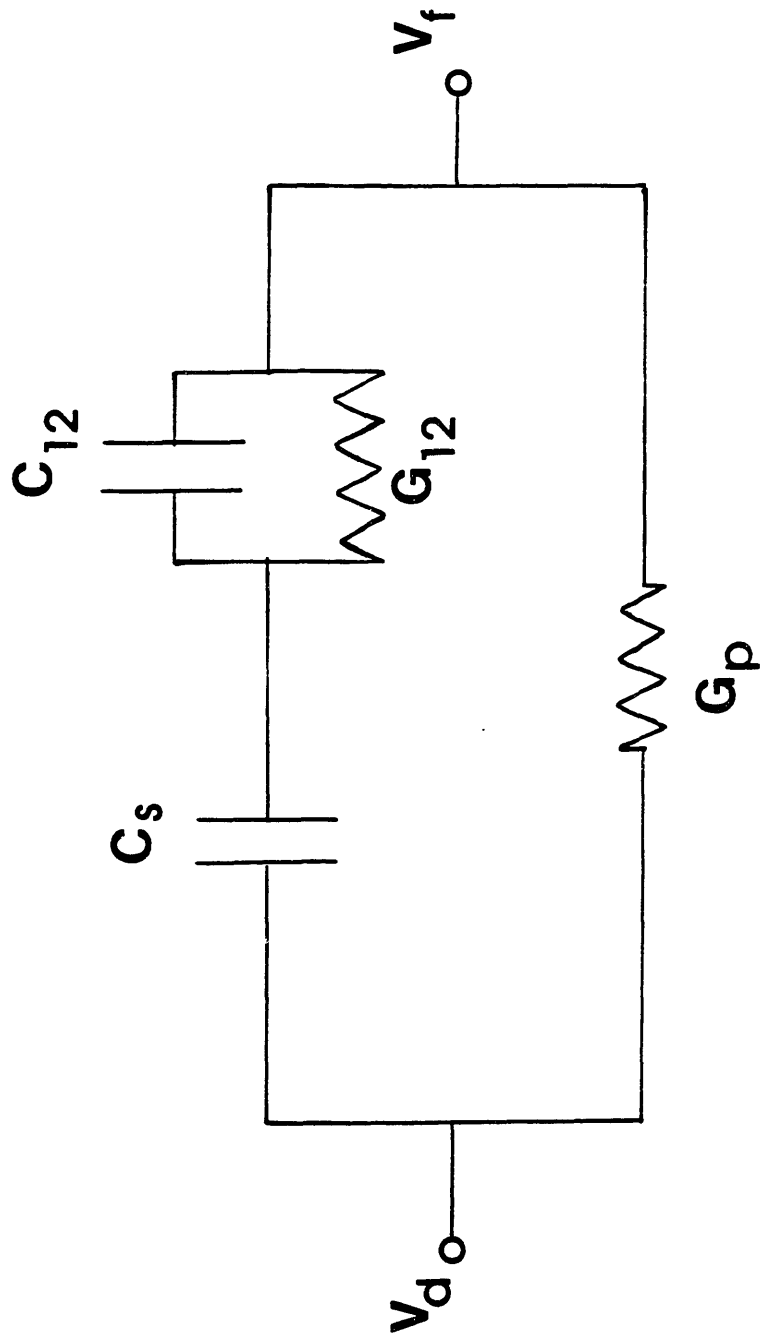
Figure 6.1

The lumped elements model used to get a first account of the
surface effects
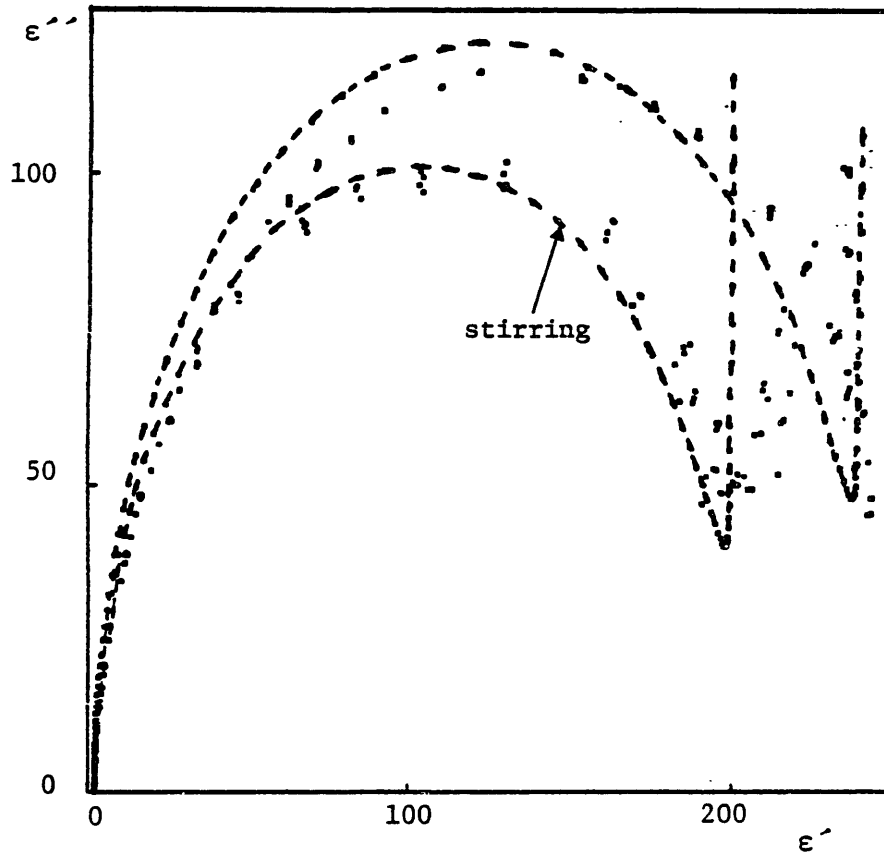
Figure 6.2

Cole-Cole plot for oil with 50ppm ASA-3 fitted to
the lumped model

$$C_{12} = 2 \; , \; \frac{G}{G^p_{12}} = .01$$

nonstirring $C_s = 240$

stirring $\quad C_s = 200$

Other data curves do not necessarily show the local minima and maxima of loss shown in figure 6.2. This can be explained in terms of the frequency breakpoints associated with the equivalent circuit. The three frequency breakpoints are:

$$\omega_1 = \frac{G_{12}}{(C_{12}C_s + C_{12}{}^2)^{\frac{1}{2}}}$$

$$\omega_2 = \frac{G_{12}}{C_s + C_{12}}$$

$$\omega_3 = \left(\frac{G_p G_{12}{}^2}{G_{12}C_s{}^2 + G_p(C_s + C_{12})^2}\right)^{\frac{1}{2}} \tag{38}$$

If ω_3 is considerably smaller than ω_2, the loss will exhibit a clear local maxima at ω_2, and a local minima at ω_3. With an increase in the parallel conductance G_p with respect to the bulk G_{12}, the two frequency breakpoints become closer to each other. Figure 6.3 shows the effect of increasing $\frac{G_p}{G_{12}}$ on the shape of the Cole-Cole plot, and the frequency dependence of the loss. For large $\frac{G_p}{G_{12}}$ the half circle is not clear on the Cole-Cole plot, and the deviation of the loss appears as a change of slope around the breakpoint frequencies. At very low frequencies (i.e. $\omega \ll \omega_2$) ε' reaches C_p. As shown in figure 6.4, the size of the half circle is determined by C_p.

Not all data fit this simple model as well as did the sample with 50ppm of antistatic agent. The Cole-Cole plot of the sample with .5ppm antistatic agent is shown in figure
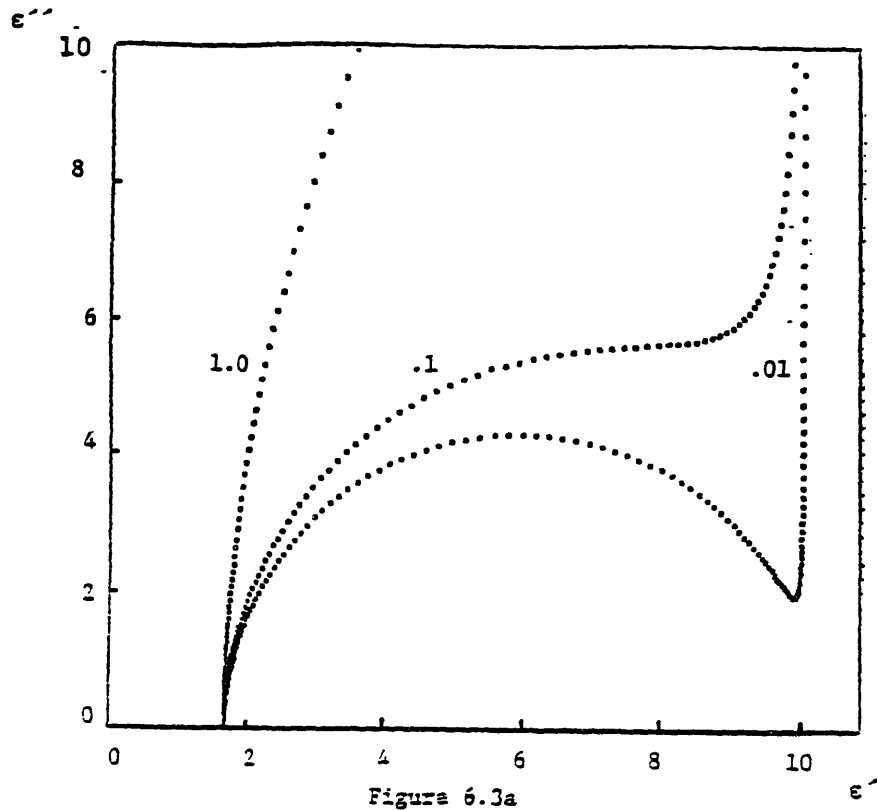
Figure 6.3a
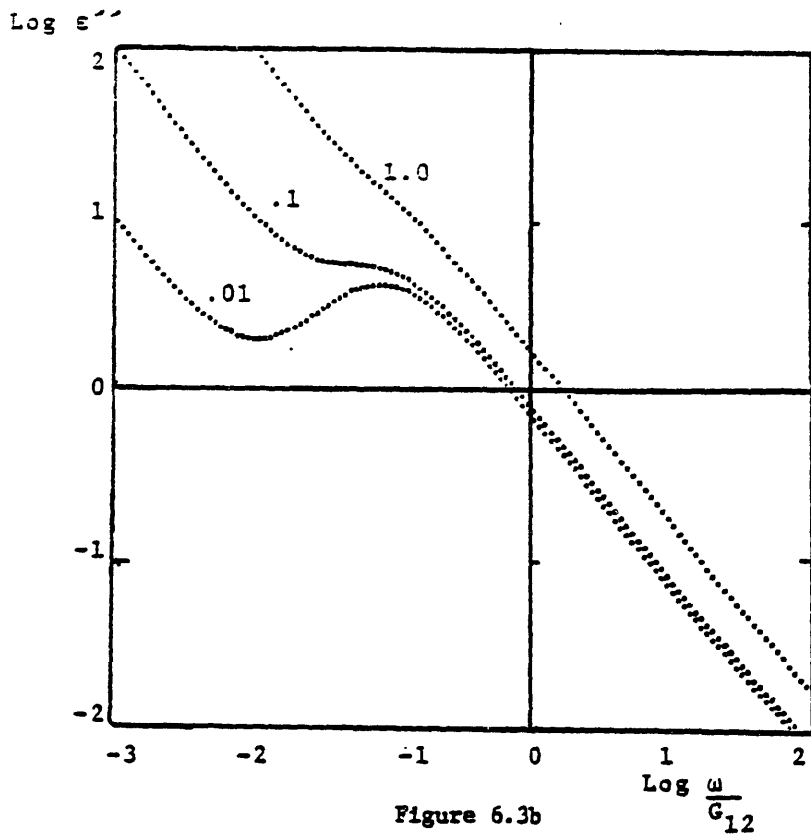
Figure 6.3b

Figure 6.3

The effect of varying $\frac{G_p}{G_{12}}$ on the lumped model response

$C_{12}=2$, $C_s=10$, and $\frac{G_p}{G_{12}}$ is shown on each of the three curves
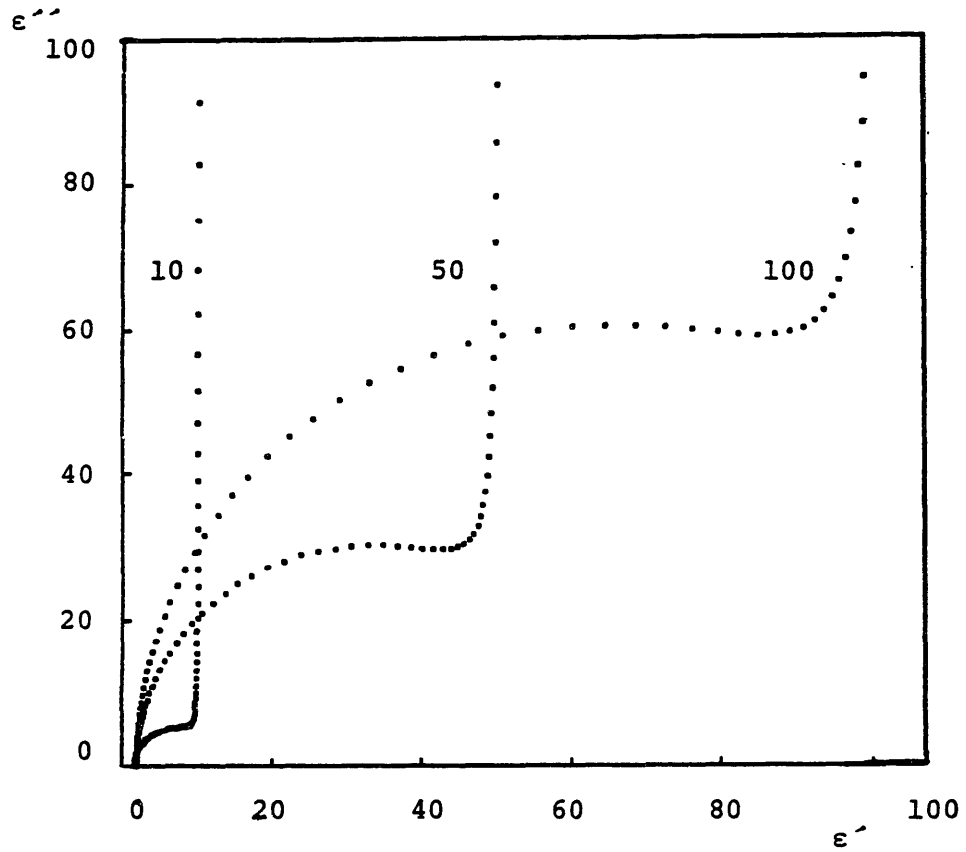
Figure 6.4

Effect of varying C_s on the radius of the semihalf circle of the Cole-Cole plot.

$$C_{12} = 2, \quad \frac{G_p}{G_{12}} = .1$$

6.5 with the calculated values based on the lumped element model. One clear reason for the discrepancy is the frequency dependence of C_{12} and G_{12} as was discussed in section 4.1. Combining the calculated frequency dependent C_{12} & G_{12} with constant C_s and G_p, the gain and phase can be calculated at various frequencies. The gain phase response shows the "two-humps", shape as shown in figure 6.6, but can not be fitted well to the actual data, because frequency independent values are not adequate to predict the response. Shown in figure 6.7 are the $\underline{C}_s$ and $\underline{G}_p$ needed to predict the observed gain and phase at various frequencies for oil sample with .5ppm ASA-3.

There are three aspects to the frequency dependence of C_s and G_p. One is the result of assuming that C_{12} and G_{12} are the same as calculated with no surface effects. In reality, they are influenced by the effect of surface phenomena on the field distribution. The second is due to the effect of geometry in making the equivalent surface parameters frequency dependent. The third aspect is the possibility that the surface phenomena depend on the frequency of excitation. A combination of the three aspects produces the dependence observed in figure 6.7.

6.2 The Series Capacitance

The higher measured ε' at low frequency indicates an increase of stored energy. A double layer can account for this increase of stored energy. An approximate value for the
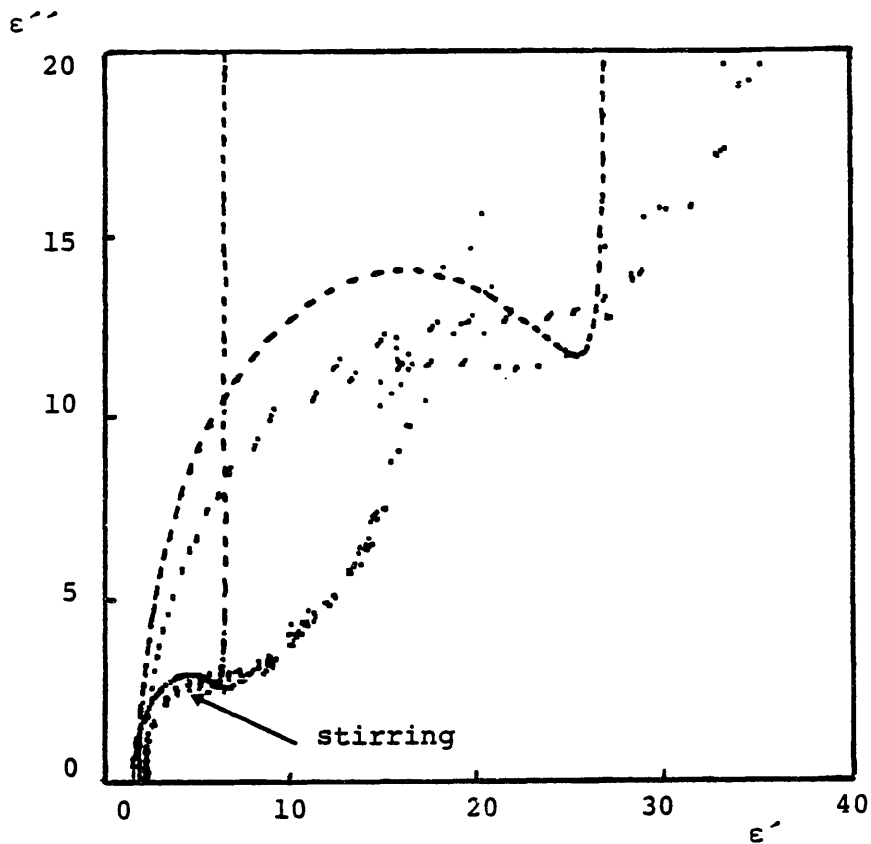
Figure 6.5
Cole-Cole plot for oil with .5ppm ASA-3 fitted to
the lumped model

$$C_{12} = 2 \quad , \quad \frac{G}{G_{12}}p = .05$$

nonstirring $C_s = 27$

stirring $\quad C_s = 6.5$
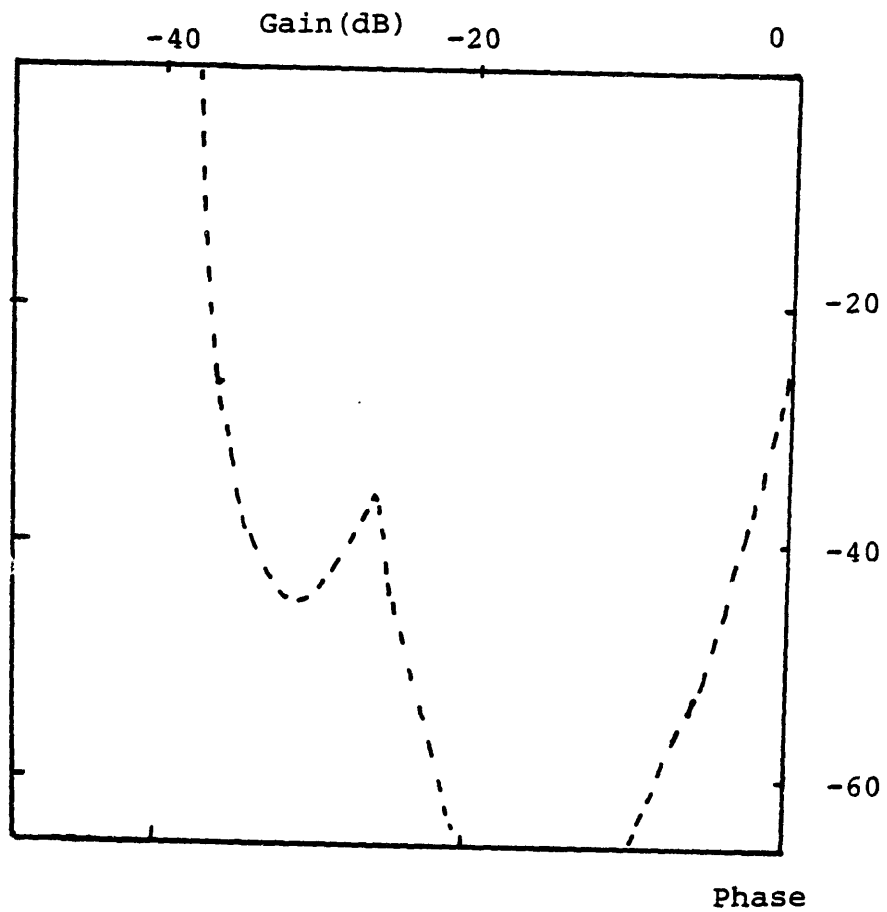
Figure 6.6

Gain-phase plot for lumped model showing clear "dual-hump" shape.

$$\frac{G_p}{Nd\sigma_\ell} = .15, \frac{C_s}{Nd\varepsilon_{ox}} = .4$$

$$\frac{\varepsilon_\ell}{\varepsilon_o} = 2.0$$

Normalized surface admittance
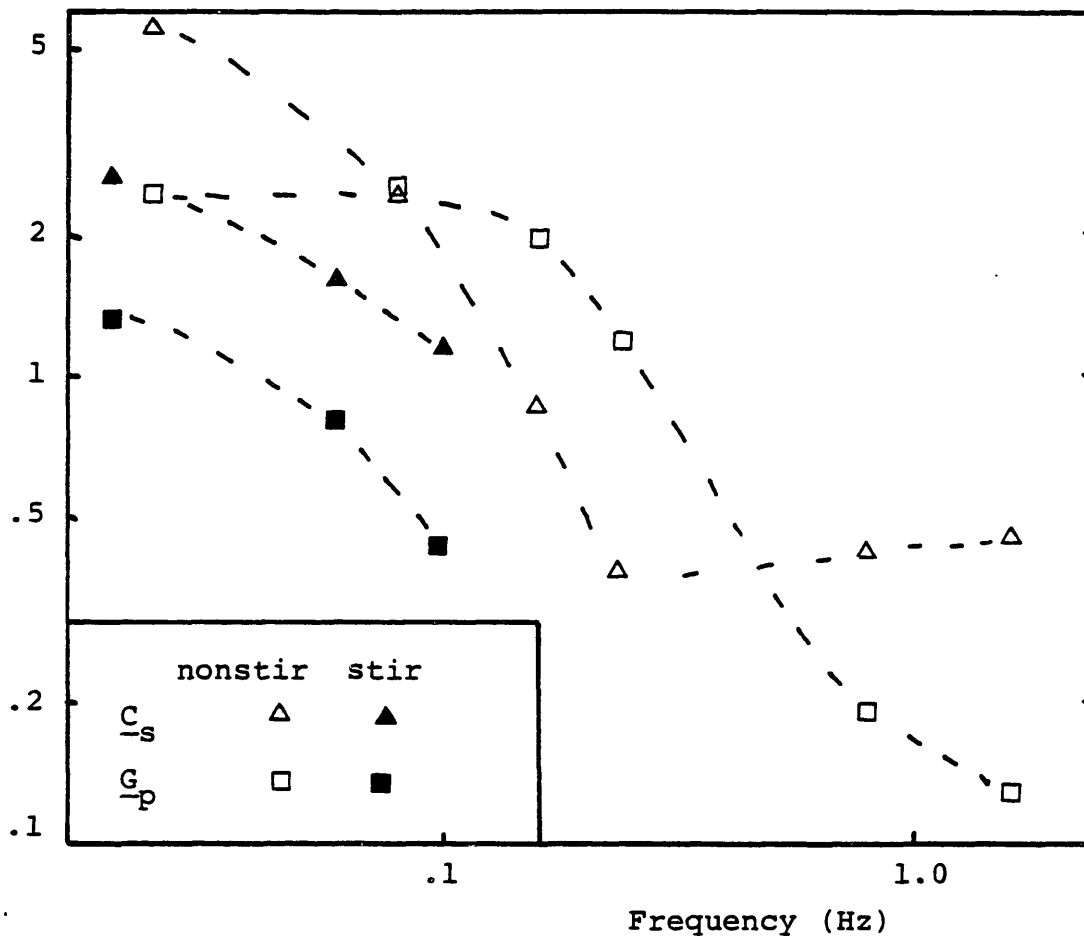
Figure 6.7

Value of lumped parameters obtained from the response
of oil sample with .5ppm ASA-3 as a function of frequency.

capacitance involved can be obtained from the asymptotic value of the gain hump on the gain phase plot. For the various experiments described in the previous chapter, the equivalent normalized capacitance is shown in figure 6.8 as a function of the conductivity. Assuming the equivalent double layer capacitance to be* $\frac{W\varepsilon_\ell}{2\ell_d}$, the effective Debye length for each case can be obtained. As figure 6.8 shows, the calculated values are of the expected order of magnitude $(\frac{\varepsilon_0 D}{\sigma_\ell})^{\frac{1}{2}}$ where D is the diffusion coefficient. For an oil sample with conductivity of 10^{-10} mho/m, and assuming an ion mobility of 10^{-9} $\frac{m^2}{V-sec}$ as was discussed in section 2.2, the calculated Debye length is $\simeq 2.2$ μm.

Stirring shows an effect on the equivalent capacitance. The decrease in capacitance is implied by three observations: a smaller half circle on the Cole-Cole plot, a lower asymptotic value on the gain-phase plot, and an increase of the breakpoint frequency ω_2. The increase of the capacitance reflects larger diffused layer thickness for the stirred sample. For our case, the decrease of capacitance may be due to an increase of spatial decay rate of the charge due to turbulence enhanced diffusion. Diffused layers in electrolytes show a sensitivity to fluid motion [40], but the tendency of motion is to thin down the diffusion layer thickness.

Since the Debye length (based on molecular diffusion)

---

*The factor of two is due to having a double layer at each of the two electrodes.
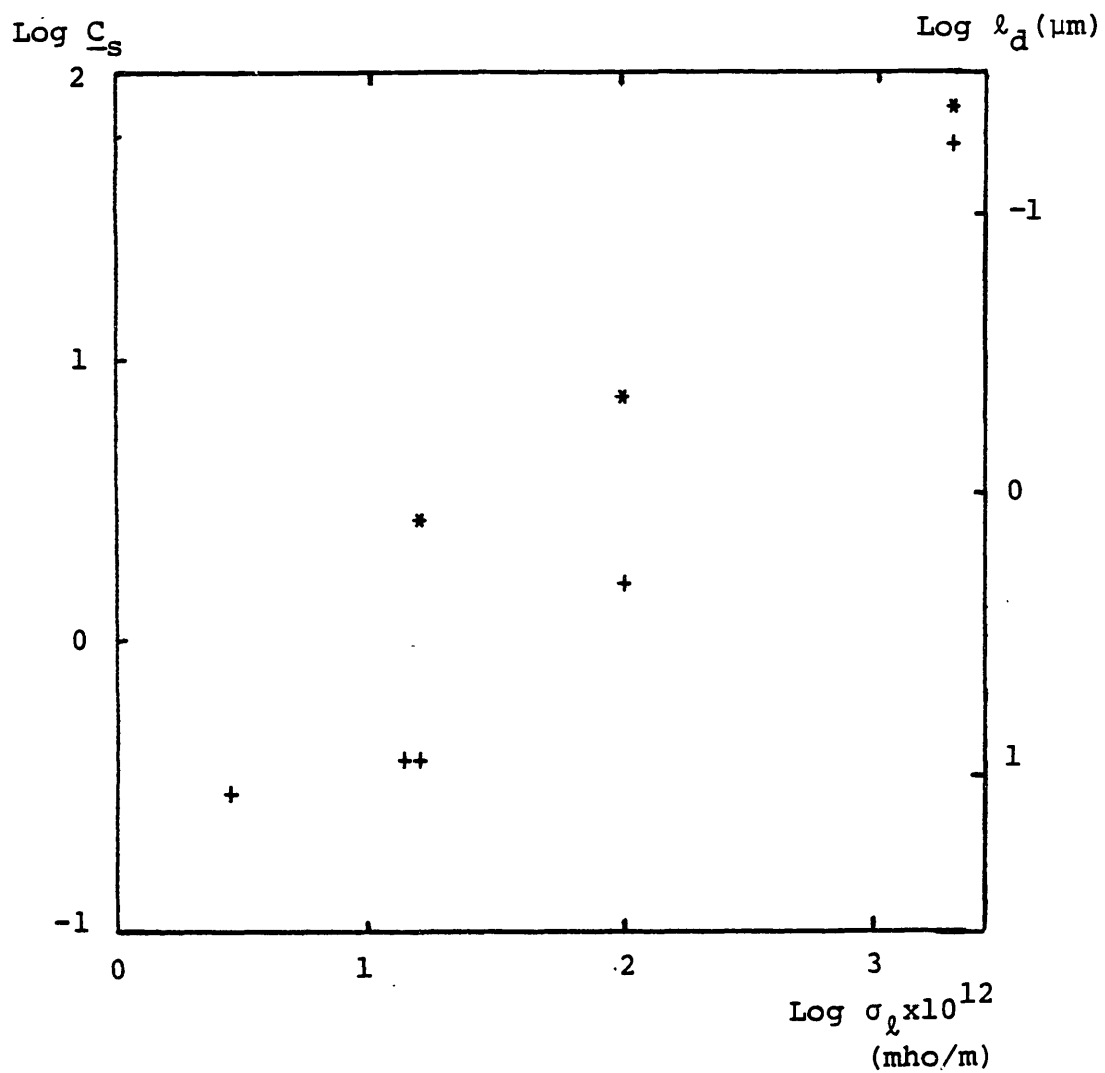
Figure 6.8
Normalized series capacitance and equivalent Debye
length as a function of the high frequency conductivity
of various oil samples.

* nonstirring
+ stirring

for low conductivity samples is on the order of microns, and since the separation between the electrodes themselves is 12.5 μm, the capacitance of the surface layer can be of the same order as the capacitance of the bulk. Such a small capacitance should cause a change of high frequency gain. But the measured gain in the high frequency limit agrees well with the expected value corresponding to the bridge measured permittivity. A large capacitance at high frequencies can explain the lack of deviation in the high frequency gain. A diffusion skin depth of $(\frac{2D}{\omega})^{\frac{1}{2}}$ [41] causes the increase of capacitance at high frequency. A diffusion impedance is frequency dependent due to the diffusion skin depth [42], and such dependence can account for part of the frequency dispersion apparent in figure 6.6. However, no conclusion can be made unless the frequency dependence introduced by geometrical factors is accounted for.

6.3 The Parallel Conductance

A surface conduction can occur at the insulation/fluid interface due to adsorption of ions [43]. Silicon dioxide shows a surface conductivity in humid atmosphere [44] , and thus the oil's water content can affect the surface conductivity on the sensor.

The time trends observed in figures 5.10, 5.14, and 5.16 indicate a slow adsorption process causing the increase of equivalent loss.

Unless the polarization of the electrodes is taken into

account in the continuum model, the surface conductivity can not be calculated. However, using the lumped model, an estimate for its order of magnitude can be obtained from the value of parallel conduction G_p. The surface conductivity for data obtained with pure oil is $\approx 10^{-17}$ mhos. For oil with .5ppm and 50ppm ASA-3, the estimated surface conductivities are on the order of 10^{-16} and 10^{-15} mhos respectively.

6.4 Additional Effects

The proposed lumped model indicates a perpendicular line at low frequencies on the Cole-Cole plot. However, the observed data shows curvature at the low frequency limit. An additional capacitance in series with G_p can account for this curvature. In terms of physical phenomena, such a capacitance indicates a contact effect similar to what is described in section 4.3.

Chapter VII
Suggestions for Further Research

Further work is needed in three aspects. The first concerns the numerical method used. The second is further investigation of the surface phenomena involved. The third aspect concerns the additional work needed to use the sensors in an on-line monitoring system.

7.1 Improvement of the Numerical Technique

Further work is needed to improve the numerical technique described in this thesis. The choice of the collocation points at equal distances as described in section 3.3 is not optimum. The high field at the edge of the electrode is critical in determining the number of collocation points needed at the interface. Using a dense distribution of points near the electrodes and a sparse one away from them can reduce the total number of points needed, and improve the efficiency of computation. Placing the k collocation points at $x_j = \frac{\lambda}{4} - \frac{\lambda}{8} \cos(\frac{j\pi}{k+1})$ reduces the number of points required to achieve the same accuracy from k for equally spaced collocation points to $\sqrt{k}$ [45].

The numerical technique needs to be used to account for the polarization of the electrodes in a continuum fashion. This can be done by deriving the transfer relations of a medium with space charge polarization in case of a small applied field where the system can be linearized. It is

essential to deal with a linear system to use the transfer relation approach. An approximate solution derived from assuming a thin insulating layer at the electrodes surface might prove adequate in accounting for the space charge effect when combined with a surface conductivity.

7.2 Further Studies on the Interface

Further work is needed to characterise the surface phenomena appearing at the sensor/oil interface. The correlation between the observed capacitance of the double layer and the conductivity of the sample needs to be studied. This may be accomplished by adding various concentrations of the additive discussed in this thesis (i.e. ASA-3), as well as other types of additives. The equivalent capacitance can be further investigated by varying the magnitude of the potential applied to the electrodes.

Applying a DC field in the vicinity of the sensor can help in understanding the nature of the conduction path between the electrodes. An electrically induced adsorption process will be accelerated by the applied field. The effect of the applied field and its intensity on the time constants observed when the sensor is initially immersed in oil, can provide useful information about the adsorption mechanism causing the conduction path.

A well defined flow with a controlled flow rate need to be used in investigating the effects of motion further. The

dependence of the response on the flow rate can lead to identifications of critical velocities (if any exists).

Temperature effects can shed further light on the interface. The balance between the bulk and surface concentrations of ions will vary with temperature, and thus the ratio of the surface conduction path (normalized) to the bulk conductivity would change.

7.3 Further Research on the Practicality of Using Microdielectric Sensors to Monitor Transformers

The ability of sensors to detect degradation processes needs to be investigated. Oxidation of oil will probably be detectable with bare sensors. The response at various concentrations of dissolved water needs to be studied further. A good correlation can make the sensors valuable in measuring water contents in oil. Coatings which can increase the sensor's sensitivity to water, or sensitize it to some gasses, need to be determined.

An essential factor in determining the practicality of using the sensors is their ability to function in the rugged environment of a transformer. The noise level in the transformer might prove to be too high, or some floating pieces of insulation or metal might get deposited on the electrodes impeding the operation of the sensor. Protection mechanisms such as shielding the sensors from the noise, and preventing stray pieces from floating into its vicinity should be considered. The obvious test of the ability of the

sensor to function under rugged conditions is to try using
it in an operating transformer.

Appendix A

The set of k equations obtained from evaluating equation (25) for each of the k segments is of the form $\bar{\bar{A}} \cdot \bar{V} = \bar{X}$, where $\bar{V}$ is the vector of unknown V_j ' s. The matrix $\bar{\bar{A}}$ can be written as a sum of four elementary matrices.

$$\bar{\bar{A}} = \bar{\bar{A}}1 + (\varepsilon_\ell - j\sigma_\ell)\bar{\bar{A}}2 + \bar{\bar{A}}3 + (\varepsilon_s - j\sigma_s)\bar{\bar{A}}4 \tag{A1}$$

The vector $\bar{X}$ can be written as a sum of four elementary vectors.

$$\bar{X} = \bar{X}1 + (\varepsilon_\ell - j\sigma_\ell)\bar{X}2 + \bar{X}3 + (\varepsilon_s - j\sigma_s)\bar{X}4 \tag{A2}$$

The definitions of these elementary matrices and vectors are shown on the following page. The only matrices requiring summation of the Fourier components are $\bar{\bar{A}}1$ and $\bar{\bar{A}}2$, and the only vectors involving such summation are $\bar{X}1$ and $\bar{X}2$. The program "mkcoef.c" calculates these vectors and matrices for a given $\frac{\lambda}{h}$.

The code of the program used in the simulation is provided. The program "simulate.c" generates $\bar{\bar{A}}$ and $\bar{X}$ from their elementary components according to equation (A1). The generation of the coefficients was divided into the two programs "mkcoef.c" and "simulate.c" so that the Fourier summation does not need to be repeated for changing the surface or bulk conductivity or permittivity. Once the dimensions of the sensor are set, "mkcoef.c" needs to be used only once, then "simulate.c" can be used to calculate

the response under varying bulk and surface properties.

Solving the set of linear equations with complex coefficients requires complex numbers arithmetic subroutines which are provided in the file "convert.c". The equivalent circuit elements of the sensor are generated using the subroutine provided by "cap.c", and the gain-phase response is calculated by the subroutine in "bode.c".

Elementary Matrices of $\bar{\bar{A}}$

$$\bar{\bar{A}}_1[r,c] = \frac{4k}{\pi^2} \sum_1^\infty \frac{1}{n^2} \coth(\frac{2\pi nh}{\lambda}) \; \bar{\bar{D}}[r,c]$$

$$\bar{\bar{A}}_2[r,c] = \frac{4k}{\pi^2} \sum_1^\infty \frac{1}{n^2} \; \bar{\bar{D}}[r,c]$$

$$\bar{\bar{D}}[r,c] = \left(\sin(\frac{n\pi}{4k}(k+2r)) - \sin(\frac{n\pi}{4k}(k+2r-2)) \right)$$

$$\left(2\cos(\frac{n\pi}{4k}(k+2c-1)) - \cos(\frac{n\pi}{4k}(k+2c+1)) \right.$$

$$\left. -\cos(\frac{n\pi}{4k}(k+2c-3)) \right)$$

for c ≠ 1, k

$$\bar{\bar{D}}[r,1] = \left(\sin(\frac{n\pi}{4k}(k+2r)) - \sin(\frac{n\pi}{4k}(k+2r-2)) \right)$$

$$\left(3\cos(\frac{n\pi}{4k}(k+1)) - \cos(\frac{n\pi}{4k}(k+3)) - 2\cos(\frac{n\pi}{4}) \right)$$

$$\bar{\bar{D}}[r,k] = \left(\sin(\frac{n\pi}{4k}(k+2r)) - \sin(\frac{n\pi}{4k}(k+2r-2)) \right)$$

$$\left(3\cos(\frac{n\pi}{4k}(3k-1)) - \cos(\frac{n\pi}{4k}(3k-3)) - 2\cos(\frac{3n\pi}{4}) \right)$$

$$\bar{\bar{A}}_3[r,c] = \frac{\lambda}{hk^2} \left(\frac{1}{8} - \frac{1}{32} (\delta(r-1)+\delta(r-k)) \right)$$

$$\bar{\bar{A}}_4[r,c] = 4k \left(2\delta(r-c)-\delta(r-c+1)-\delta(r-c-1)+\delta(r-1)\delta(c-1) \right)$$

$$+\delta(r-k)\delta(c-k)\}$$

Elementary Vectors of $\bar{X}$

$$\bar{X}1[r]=\frac{4k}{\pi^2} \sum_1^\infty \frac{1}{n^2} \coth(\frac{2\pi nh}{\lambda})\ \bar{F}[r]$$

$$\bar{X}2[r]=\frac{4k}{\pi^2} \sum_1^\infty \frac{1}{n^2}\ \bar{F}[r]$$

$$\bar{F}[r]= \left(\ \sin(\frac{n\pi}{4k}(k+2r)) - \sin(\frac{n\pi}{4k}(k+2r-2))\ \right)$$

$$\left(\ 2\cos(\frac{n\pi}{4k}(k+1)) - 2\cos(\frac{n\pi}{4k})\ \right)$$

$$\bar{X}3[r] = -\ \frac{(2k+1)\lambda}{32hk^2}$$

$$\bar{X}4[r] = 8k\ \delta(r-1)$$

```
/************************************************************/
/*                        mkcoefn.c                         */
/*                      date: 11/27/84                      */
/*                                                          */
/* This program calculates the matrices Al and A2,          */
/* and the vectors X1 and X2.                               */
/* The limit on the summation is a maximum t of n           */
/************************************************************/
#include <stdio.h>
#include <math.h>

#define PI 3.141592654
main()
{
double al[40][40],a2[40][40],x1[40],x2[40],d,rw,h,pi,trml,trm2,s1,s2;
int n,k,f,r,c,t;
FILE *fp, *fopen();
fp=fopen("coef.p","w");
printf("input #of points\n");
scanf("%d",&k);
printf("input normalized width\n");
scanf("%f",&rw);
h=1.0/4.0/rw;
printf("input max number of terms\n");
scanf("%t",&t);
pi=PI/4.0/k;
f=0;
r=1;
while (r<=k)
        {
        s1=0;
        s2=0;
        trml=1;
        n=1;
        c=1;
        if(((k%2)==0)&&(r==(k/2+1))) f=1;
        if (f==1)
                {
                al[r-1][c-1]=al[k-r][k-c];
                a2[r-1][c-1]=a2[k-r][k-c];
                }
        else
                {
                while ( n<t)
                        {
                        trm2=1.0/n/n;
                        trml=trm2*(1.0/tanh(2.0*PI*n*h));
                        d=(sin(n*pi*(k+2.0*r))
                          -sin(n*pi*(k+2.0*r-2.0)))
                            *(3.0*cos(n*pi*(k+1.0))
                              -cos(n*pi*(k+3.0))
                              -2.0*cos(n*pi*k));
                        s1+=(trml*d);
                        s2+=(trm2*d);
```

```
                                n++;
                                }
                        al[r-1][0]=4.0*k/PI/PI*s1;
                        a2[r-1][0]=4.0*k/PI/PI*s2;
                        }
        printf("A[%d][0]\tn=%d\n",(r-1),n);
        c=2;
        while(c<k)
                {
                if(((k%2)==1)&&(r==((k+1)/2))&&(c==((k+3)/2))) f=1;
                if (f==1)
                        {
                        al[r-1][c-1]=al[k-r][k-c];
                        a2[r-1][c-1]=a2[k-r][k-c];
                        n=1;
                        }
                else
                        {
                        s1=0;
                        s2=0;
                        trml=1;
                        n=1;
                        while (n<t)
                                {
                                trm2=1.0/n/n;
                                trml=trm2*(1.0/tanh(2.0*PI*n*h));
                                d=(sin(n*pi*(k+2.0*r))
                                  -sin(n*pi*(k+2.0*r-2.0)))

*(2.0*cos(n*pi*(k+2.0*c-1.0))

                                        -cos(n*pi*(k+2.0*c+1.0))
                                        -cos(n*pi*(k+2.0*c-3.0)));
                                s1+=(trml*d);
                                s2+=(trm2*d);
                                n++;
                                }
                        al[r-1][c-1]=4.0*k*s1/PI/PI;
                        a2[r-1][c-1]=4.0*k*s2/PI/PI;
                        }
                printf("A[%d][%d]\tn=%d\n",(r-1),(c-1),n);
                c++;
                }
        if(((k%2)==1)&&(r==((k+1)/2))&&(c==((k+3)/2))) f=1;
        if (f==1)
                {
                al[r-1][c-1]=al[k-r][k-c];
                a2[r-1][c-1]=a2[k-r][k-c];
                }
        else
                {
                s1=0;
                s2=0;
                trml=1;
                n=1;
```

136

```
                while (n<t)
                        {
                        trm2=1.0/n/n;
                        trml=trm2*(1.0/tanh(2.0*PI*n*h));
                        d=(sin(n*pi*(k+2.0*r))
                          -sin(n*pi*(k+2.0*r-2.0)))
                                *(3.0*cos(n*pi*(3.0*k-1.0))
                                    -cos(n*pi*(3.0*k-3.0))
                                    -2.0*cos(n*pi*3.0*k));
                        sl+=(trml*d);
                        s2+=(trm2*d);
                        n++;
                        }
                al[r-1][k-1]=4.0*k/PI/PI*sl;
                a2[r-1][k-1]=4.0*k/PI/PI*s2;
                }
        printf("A[%d][%d]\tn=%d\n",(r-1),(k-1),n);
        sl=0;
        s2=0;
        trml=1;
        n=1;
        while (n<t)
                        {
                        trm2=1.0/n/n;
                        trml=trm2*(1.0/tanh(2.0*PI*n*h));
                        d=(sin(n*pi*(k+2.0*r))-sin(n*pi*(k+2.0*r-2.0)))
                                *(cos(n*pi*(k+1.0))-cos(n*pi*k));
                        sl+=(trml*d);
                        s2+=(trm2*d);
                        n++;
                        }
        xl[r-1]=8.0*k*sl/PI/PI;
        x2[r-1]=8.0*k*s2/PI/PI;
        printf("X[%d]\tn=%d\n",(r-1),n);
        r++;
        }
fprintf(fp,"%d\n",k);
fprintf(fp,"%f\n",h);
for(r=0;r<k;r++)
        {
        for(c=0;c<k;c++)
                {
                fprintf(fp,"%f\n%f\n",al[r][c],a2[r][c]);
                }
        fprintf(fp,"%f\n%f\n",xl[r],x2[r]);
        }
fclose(fp);
}
```

```c
/****************************************************************/
/*                      simulate.c                           */
/*                      date: 8/3/84                         */
/*                                                            */
/* This program generates the matrix A and the vector x.*/
/* Then it calls the appropriate subroutines to find the*/
/* vector V, the eqiuvalent circuit of the sensor, and  */
/* the gain-phase response.                              */
/****************************************************************/
#include <stdio.h>
#include <math.h>
#define PI 3.141592654
#include "convert.c"
#include "solv.c"
#include "cap.c"
#include "bode.c"
float f1(r,c,k)
int r,c,k;
        {
        if((c==0)||(c==(k-1)))
                return(3.0/32.0);
        else
                return(1.0/8.0);
        }
float f2(r,c,k)
int r,c,k;
        {
        if(r==c)
                {
                if((r==0)||(r==(k-1)))
                        return(12.0);
                else
                        return(8.0);
                }
        else if (((r-c)==1)||((c-r)==1))
                return(-4.0);
        else
                return(0.0);
        }
main()
{
int k,r,c;
double a1[30][30],a2[30][30],x1[30],x2[30];
double h,rse,ise,re,rc,ryl,iyl;
char q[5],file_name[30];
struct complex ctemp1,ctemp2,se,e,yl,yl1,yl2;
struct complex a[30][30],x[30],y[30];
struct polar py;
FILE *fpi,*fpo,*fopen();
printf("input coefficient file name\n");
scanf("%s",file_name);
fpo=fopen("simulate.p","w");
fpi=fopen(file_name,"r");
fprintf(fpo,"output of 'sensor/simulate.c'\n\n\n");
```

```
printf("input normalized epsilon\n");
scanf("%f",&re);
printf("input normalized conductivity\n");
scanf("%f",&rc);
printf("input normalized surface epsilon\n");
scanf("%f",&rse);
printf("input normalized surface conductivity\n");
scanf("%f",&ise);
printf("input normalised load capacitance\n");
scanf("%f",&ryl);
printf("input normalised load conductance\n");
scanf("%f",&iyl);
e.real=re;
e.imag=(-rc);
se.real=rse;
se.imag=(-ise);
yl.real=ryl;
yl.imag=(-iyl);
fprintf(fpo,"el/eox=%f\tsigma/weox=%f\n",re,(-rc));
fprintf(fpo,"normalized surface capacitance=%f+j(%f)\n",rse,(-ise));
fprintf(fpo,"load capacitance=%f\tconductance=%f\n",ryl,(-iyl));
fscanf(fpi,"%d",&k);
printf("#of points=%d\n",k);
fprintf(fpo,"#of points=%d\n",k);
fscanf(fpi,"%f",&h);
printf("w/h=%f\n",(1.0/4.0/h));
fprintf(fpo,"w/h=%f\n",(1.0/4.0/h));
for(r=0;r<k;r++)
        {
        for(c=0;c<k;c++)
                {
                fscanf(fpi,"%f",&a1[r][c]);
                fscanf(fpi,"%f",&a2[r][c]);
                real_complex(a1[r][c],&ctemp1);
                real_complex(a2[r][c],&ctemp2);
                cmul(&ctemp2,&e,&ctemp2);
                cadd(&ctemp1,&ctemp2,&ctemp1);
                real_complex(((f1(r,c,k))/h/k/k),&ctemp2);
                cadd(&ctemp1,&ctemp2,&ctemp1);
                real_complex(((f2(r,c,k))*k),&ctemp2);
                cmul(&ctemp2,&se,&ctemp2);
                cadd(&ctemp1,&ctemp2,&a[r][c]);
                printf("a[%d][%d]=%f+j(%f)\n",
                        r,c,a[r][c].real,a[r][c].imag);
                }
        fscanf(fpi,"%f",&x1[r]);
        fscanf(fpi,"%f",&x2[r]);
        real_complex(x1[r],&ctemp1);
        real_complex(x2[r],&ctemp2);
        cmul(&ctemp2,&e,&ctemp2);
        cadd(&ctemp1,&ctemp2,&ctemp1);
        real_complex((-(2.0*k+1.0)/32.0/h/k/k),&ctemp2);
        cadd(&ctemp1,&ctemp2,&x[r]);
        if (r==0)
```

139

```c
                        {
                        real_complex((8.0*k),&ctempl);
                        cmul(&se,&ctempl,&ctempl);
                        cadd(&x[r],&ctempl,&x[r]);
                        }
                printf("x[%d]=%f+j(%f)\n",r,x[r].real,x[r].imag);
                }
fclose(fpi);
solve(a,x,y,k);
for (r=0;r<k;r++)
                {
                for (c=0;c<k;c++)
                        {
                        fprintf(fpo,"a[%d][%d]=%f+j(%f)\n",r,c,a[r][c].real,
                                a[r][c].imag);
                        }
                fprintf(fpo,"x[%d]=%f+j(%f)\n",r,x[r].real,x[r].imag);
                }
for(r=0;r<k;r++)
                {
                printf("y[%d]=%f+j(%f)=",r,y[r].real,y[r].imag);
                car_pol(&y[r],&py);
                printf("%fexpj(%f)\n",py.mag,py.angle);
                fprintf(fpo,"y[%d]=%f+j(%f)=",r,y[r].real,y[r].imag);
                fprintf(fpo,"%fexpj(%f)\n",py.mag,py.angle);
                }
printf("do you want impedance and gain phase results?\n");
scanf("%s",q);
if(q[0]=='y')
                {
                cap(&yl1,&yl2,y,&e,&se,h,k,fpo);
                bode(&yl1,&yl2,&yl,fpo );
                }
fclose(fpo);
printf("output in file simulate.p\n");
}
```

```
/**********************************************************/
/*                    cap.c                           */
/*                    date: 7/26/84                   */
/*                                                    */
/* This program calculates y11 and y12               */
/* The function is cap()                             */
/* its inputs are:                                   */
/*      V a vector of node voltages (double).        */
/*      pe pointer to normalized complex epsilon.    */
/*      pse pointer to normalized surface capacitance */
/*      h normalized height.                         */
/*      k number of nodes.                           */
/*      fp pointer to output file.                   */
/**********************************************************/
cap(py11,py12,v,pe,pse,h,k,fp)
double h;
struct complex v[];
struct complex *py11,*py12,*pe,*pse;
int k;
FILE *fp;
        {
        double m,pi,d;
        struct complex s1,s2,x,trm,temp1,temp2,temp3;
        int n,j;
        pi=PI/4.0/k;
        j=2;
        cnull(&x);
        while (j<k)
                {
                cadd(&x,&v[j-1],&x);
                j++;
                }
        m=k;
        cadd(&v[0],&v[k-1],&temp1);
        real_complex((3.0/8.0/m),&temp2);
        cmul(&temp1,&temp2,&temp1);
        real_complex((0.5/m),&temp2);
        cmul(&x,&temp2,&temp2);
        cadd(&temp2,&temp1,&temp1);
        real_complex(((2.0*m+1.0)/8.0/m),&temp2);
        cadd(&temp2,&temp1,&temp1);
        real_complex((1.0/4.0/h*PI*PI/8.0/m),&temp2);
        cmul(&temp1,&temp2,&s1);
        real_complex(2.0,&temp1);
        cmul(&s1,&temp1,&s2);
        cass(&s2,&trm);
        cnull(&temp1);
        cnull(&temp2);
        n=1;
        while ( (n<201)&&
                ( (cgt(&trm,&temp1)) || (cgt(&trm,&temp2)) ))
                {
                j=2;
                d=(3.0*cos(n*pi*(k+1.0))
```

141

```
                        -cos(n*pi*(k+3.0))
                        -2.0*cos(n*PI/4.0));
                real_complex(d,&temp1);
                cmul(&temp1,&v[0],&temp1);
                d=(3.0*cos(n*pi*(3.0*k-1.0))
                        -cos(n*pi*(3.0*k-3.0))
                        -2.0*cos(3.0*n*PI/4.0));
                real_complex(d,&temp2);
                cmul(&temp2,&v[k-1],&temp2);
                cadd(&temp1,&temp2,&x);
                while(j<k)
                        {
                        d= (2.0*cos(n*pi*(k+2.0*j-1.0))
                                -cos(n*pi*(k+2.0*j+1.0))
                                -cos(n*pi*(k+2.0*j-3.0)));
                        real_complex(d,&temp1);
                        cmul(&temp1,&v[j-1],&temp1);
                        cadd(&x,&temp1,&x);
                        j++;
                        }
                d=1.0/tanh(2.0*PI*n*h);
                real_complex(d,&temp1);
                cadd(pe,&temp1,&temp1);
                real_complex((1.0/n/n),&temp2);
                cmul(&temp1,&temp2,&trm);
                d=2.0*cos(n*PI/4.0)-2.0*cos(n*pi*(k+1));
                real_complex(d,&temp1);
                cadd(&x,&temp1,&temp1);
                cmul(&temp1,&trm,&temp1);
                real_complex((sin(n*PI/4.0)),&temp2);
                cmul(&temp1,&temp2,&x);
                real_complex((cos(n*PI)),&temp1);
                cmul(&temp1,&x,&temp1);
                cadd(&s1,&temp1,&s1);
                real_complex((1.0+cos(n*PI)),&temp1);
                cmul(&temp1,&x,&temp1);
                cadd(&s2,&temp1,&s2);
                n++;
                real_complex(0.001,&temp1);
                cmul(&s2,&temp1,&temp2);
                cmul(&s1,&temp1,&temp1);
                }
        printf("n=%d\n",n);
        fprintf(fp,"n=%d\n",n);
        real_complex((16.0*k),&temp3);
        cmul(pse,&temp3,&temp3);        /* temp3=16 kse        */
        real_complex(((-8.0)*k/PI/PI),&temp1);
        cmul(&temp1,&s1,&temp1);
        cmul(&v[k-1],&temp3,&temp2);
        cadd(&temp1,&temp2,pyl2);
        real_complex((8.0*k/PI/PI),&temp1);
        cmul(&temp1,&s2,&temp1);
        real_complex(1.0,&temp2);
        csub(&temp2,&v[0],&temp2);
```

```
csub(&temp2,&v[k-1],&temp2);
cmul(&temp2,&temp3,&temp2);
cadd(&temp2,&templ,pyl1);
printf("cl1=%f\tgl1/w=%f\ncl2=%f\tgl2/w=%f\n",(*pyl1).real,
       (-(*pyl1).imag),(*pyl2).real,(-(*pyl2).imag));
fprintf(fp,"cl1=%f\tgl1/w=%f\ncl2=%f\tgl2/w=%f\n",
              (*pyl1).real,(-(*pyl1).imag),(*pyl2).real,
              (-(*pyl2).imag));
}
```

```
/********************************************************/
/*                                                      */
/*                      convert.c                       */
/*                     date: 7/17/84                    */
/*                                                      */
/* This program contains complex arithmetic subroutines.*/
/********************************************************/
#include <stdio.h>
#include <math.h>
double square(x)
        double x;
        {
        return(x*x);
        }
/* declration of structure used */
struct complex { double real;double imag};
struct polar { double mag;double angle };
struct bod {double gain;double phase};

/* conversion procedures */
car_pol (pc,pp)
        struct complex *pc;
        struct polar *pp;
        {
        (*pp).mag=sqrt(square((*pc).real)+square((*pc).imag));
        (*pp).angle=atan2((*pc).imag, (*pc).real);
        }

pol_car (pp,pc)
        struct complex *pc;
        struct polar *pp;
        {
        (*pc).real=(*pp).mag*cos((*pp).angle);    .
        (*pc).imag=(*pp).mag*sin((*pp).angle);
        }

pol_bod (pp,pb)
        struct bod *pb;
        struct polar *pp;
        {
        (*pb).gain=20*log10((*pp).mag);
        (*pb).phase=(*pp).angle*180/3.14;
        }

car_bod (pc,pb)
        struct bod *pb;
        struct  complex *pc;
        {
        struct polar p;
        car_pol (pc,&p);
        pol_bod (&p,pb);
        }

real_complex(a,pc)
```

```
                 double a;
                 struct complex *pc;
                 {
                 (*pc).real=a;
                 (*pc).imag=0;
                 }

/* arithmatic prcdures */
cmul(pcl,pc2,pc3)   /* c3=c2*cl */
                 struct complex *pcl,*pc2,*pc3;
                 {
                 struct polar ppl,pp2,pp3;
                 car_pol (pcl,&ppl);
                 car_pol (pc2,&pp2);
                 pp3.mag=ppl.mag*pp2.mag;
                 pp3.angle=ppl.angle+pp2.angle;
                 pol_car (&pp3,pc3);
                 }

cdiv(pcl,pc2,pc3)   /* c3=cl/c2 */
                 struct complex *pcl,*pc2,*pc3;
                 {
                 struct polar ppl,pp2,pp3;
                 car_pol (pcl,&ppl);
                 car_pol (pc2,&pp2);
                 pp3.mag=ppl.mag/pp2.mag;
                 pp3.angle=ppl.angle-pp2.angle;
                 pol_car (&pp3,pc3);
                 }

cadd(pcl,pc2,pc3)   /* c3=cl+c2 */
                 struct complex *pcl,*pc2,*pc3;
                 {
                 (*pc3).real=(*pcl).real+(*pc2).real;
                 (*pc3).imag=(*pcl).imag+(*pc2).imag;
                 }

csub(pcl,pc2,pc3)   /* c3=c2-cl */
                 struct complex *pcl,*pc2,*pc3;
                 {
                 (*pc3).real=(*pcl).real-(*pc2).real;
                 (*pc3).imag=(*pcl).imag-(*pc2).imag;
                 }

cass(pcl,pc2)                    /* c2=cl */
                 struct complex *pcl,*pc2;
                 {
                 (*pc2).real=(*pcl).real;
                 (*pc2).imag=(*pcl).imag;
                 }

cnull(pc)             /* c=0 */
                 struct complex *pc;
                 {
```

```c
        (*pc).real=0;
        (*pc).imag=0;
        }


cpow(pc,x)                      /* c=c^x */
        struct complex *pc;
        double x;
        {
        struct polar pp;
        car_pol (pc,&pp);
        pp.mag=pow((pp.mag),x);
        pp.angle=(pp.angle)*x;
        pol_car (&pp,pc);
        }

csinh(pc)               /* c=sinh(c) */
        struct complex *pc;
        {
        double r,i;
        r=(*pc).real;
        i=(*pc).imag;
        (*pc).real=sinh(r)*cos(i);
        (*pc).imag=cosh(r)*sin(i);
        }
ccosh(pc)               /* c=cosh(c) */
        struct complex *pc;
        {
        double r,i;
        r=(*pc).real;
        i=(*pc).imag;
        (*pc).real=cosh(r)*cos(i);
        (*pc).imag=sinh(r)*sin(i);
        }

/* conditonals */
zero (z)                /* z==0 */
        struct complex z;
        {
        if ((z.real==0)&&(z.imag==0)) return(1);
        else return(0);
        }

cgt(pc1,pc2)                    /* c1>c2 */
        struct complex *pc1,*pc2;
        {
        struct polar p1,p2;
        car_pol(pc1,&p1);
        car_pol(pc2,&p2);
        if (p1.mag > p2.mag) return(1);
        else return(0);
        }
```

```c
/**********************************************************/
/*                                                        */
/*                    solv.c                              */
/*                    date: 7/17/84                       */
/*                                                        */
/* This program solves  a set of linear equations with   */
/* complex coefficients.                                  */
/**********************************************************/
#include <stdio.h>
#include <math.h>
solve(pa,px,py,k)
struct complex pa[][20],px[],py[];
int k;
{
struct complex b[20][20],z[20],temp[20],tempz,tempr;
int i,r,c;
for (r=0;r<k;r++)   /* initialize both b & z */
        {
        z[r].real=px[r].real;
        z[r].imag=px[r].imag;
        for (c=0;c<k;c++)
                {
                b[r][c].real=pa[r][c].real;
                b[r][c].imag=pa[r][c].imag;
                }
        }
for (i=0;i<(k-1);i++)
        {
        while(zero(b[i][i])) /* handles the case with a zero leading
coeff */
                {
                tempz.real=z[i].real;
                tempz.imag=z[i].imag;
                for(c=i;c<k;c++)
                        {
                        temp[c].real=b[i][c].real;
                        temp[c].imag=b[i][c].imag;
                        }
                for(r=i;r<(k-1);r++)
                        {
                        z[r].real=z[r+1].real;
                        z[r].imag=z[r+1].imag;
                        for(c=i;c<k;c++)
                                {
                                b[r][c].real=b[r+1][c].real;
                                b[r][c].imag=b[r+1][c].imag;
                                }
                        }
                z[k-1].real=tempz.real;
                z[k-1].imag=tempz.imag;
                for(c=i;c<k;c++)
                        {
                        b[k-1][c].real=temp[c].real;
                        b[k-1][c].imag=temp[c].imag;
```

```
                                      }
                              }
              for(r=i+1;r<k;r++) /* generates the new set of equations */
                              {
                              cmul(&z[i],&b[r][i],&tempz);
                              cdiv(&tempz,&b[i][i],&tempr);
                              csub(&z[r],&tempr,&tempz);
                              z[r].real=tempz.real;
                              z[r].imag=tempz.imag;
                              for(c=i+1;c<k;c++)
                                      {
                                      cmul(&b[i][c],&b[r][i],&tempz);
                                      cdiv(&tempz,&b[i][i],&tempr);
                                      csub(&b[r][c],&tempr,&tempz);
                                      b[r][c].real=tempz.real;
                                      b[r][c].imag=tempz.imag;
                                      }
                              }
              }
    for(r=k-1;r>=0;r--) /* back subtitution */
              {
          cdiv(&z[r],&b[r][r],&py[r]);
          for(c=r+1;c<k;c++)
                      {
                      cmul(&b[r][c],&py[c],&tempr);
                      cdiv(&tempr,&b[r][r],&tempz);
                      csub(&py[r],&tempz,&tempr);
                      py[r].real=tempr.real;
                      py[r].imag=tempr.imag;
                      }
              }
    }
```

Equation (30) can be derived using transfer relations and boundary conditions at y=t+h. The potential is continuous at surfaces "c" and "d" shown in figure (3.8).

$$\tilde{\phi}^d(n) = \tilde{\phi}^c(n) \tag{B1}$$

The normal electric field at surfaces "c" and "d" obey the following equation:

$$(\epsilon_{\ell 2} - j\sigma_{\ell 2})\tilde{E}_y^d(n) = (\epsilon_{\ell 1} - j\sigma_{\ell 1})\tilde{E}_y^c(n) \tag{B2}$$

The normal field can be written in terms of the interface potentials.

$$\tilde{E}_y^d(n) = \frac{2\pi n}{\lambda}\,\tilde{\phi}^c(n) \qquad\qquad n \# 0$$

$$\tilde{E}_y^d(0) = E_0$$

$$\tilde{E}_y^c(n) = \frac{2\pi n}{\lambda}\left(-\coth(\frac{2\pi nt}{\lambda})\tilde{\phi}^c(n) + \frac{\tilde{\phi}^a(n)}{\sinh\frac{2\pi nt}{\lambda}} \right) \tag{B3}$$

Combining equations (B2) and (B3) we get $\tilde{\phi}^c(n)$ in terms of $\tilde{\phi}^a(n)$.

$$\tilde{\phi}^c(n) = \frac{\tilde{\phi}^a(n)}{\dfrac{\epsilon_{\ell 2} - j\sigma_{\ell 2}}{\epsilon_{\ell 1} - j\sigma_{\ell 1}}\sinh(\frac{2\pi nt}{\lambda}) + \cosh(\frac{2\pi nt}{\lambda})} \tag{B4}$$

The normal field at surface "b" in terms of the potentials at surfaces "a" and "c" and E_0 is

$$\tilde{E}_y^b(n) = \frac{2\pi n}{\lambda}\left(\coth(\frac{2\pi nt}{\lambda})\tilde{\phi}^a(n) - \frac{\tilde{\phi}^c(n)}{\sinh\frac{2\pi nt}{\lambda}} \right)$$

$$\tilde{E}_y^b(\emptyset) = \tilde{E}_y^c(\emptyset) = \frac{\varepsilon_{\ell 2} - j\sigma_{\ell 2}}{\varepsilon_{\ell 1} - j\sigma_{\ell 1}} \, E_o \qquad\qquad\qquad \text{(B5)}$$

Substituting for $\tilde{\phi}^c(n)$ in equation (B5) from equation (B4) we get the normal electric field at surface "b" as given in equation (30).

References

[1] Corvo, A. M., "Diagnostic Technique and Procedures of Preventive Maintenance of Large Transformers", Intl. Conf. on Large High Voltage Electric Systems, Paris, September 1-9, 1982.

[2] Lawson, W. G., Simmons, M. A., and Gale, P. S., "Thermal Aging of Cellulose Paper Insulation", IEEE Trans. on Electr. Insul., Vol EI-12, pp61-66, February, 1977.

[3] Rogers, R. R., "IEEE And IEC Codes to Interpert Incipient Faults in Transformers Using Gas in Oil Analysis", IEEE Trans. on Electr. Insul., Vol EI-13, pp349-354, October, 1978.

[4] Baehr, R., Breuer, W., Flottmeyer, F., Kotshingg, J., Muller, R., and Nieschwietz, H., "Diagnostic Techniques and Preventive Maintenance Procedures for Large Transformers", Intl. Conf. on Large High Voltage Electric Systems, September 1-9, 1982.

[5] Burton, P., Carballeira, M., Foschum, H., Gandillon, M., Knab, H. J., Markestein, T., Praehauser, Th., Rindfleisch, H. J., Samat, J., Schliesieng, H., Serena, E., Soldner, K., Vurachex, P., Whitelock, K., and Wolf, P. G., "New Applications of Oil Dissolved Gas Analyses and Related Problems", Intl. Conf. on Large High Voltage Electric Systems, Paris, August 29-September 6, 1984.

[6] Garverick S. L., and Senturia, S. D., "An MOS Device for AC Measurement of Surface Impedance with Application to Moisture Monitoring", IEEE Trans. on Electron Devices,

Vol ED-29, pp90-94, January, 1982.

[7] Senturia, S. D., Sheppard, N. F., Lee, H. L., and Day, D. R., "In-situ Measurement of the Properties of Curing Systems with Microdielectrometry", J. Adhesion, Vol 15, pp69-90, 1982.

[8] Lee, H. L., "Optimization of a Resin Cure Sensor", EE Thesis, M.I.T., 1982.

[9] ASTM D117-81

[10] Bartnikas, R., "Dielectric Loss in Insulating Liquids", IEEE Trans. on Electr. Insul., Vol EI-2, pp33-54, April 1967.

[11] Bartnikas, R., "Dielectric Losses in Solid-Liquid Insulating Systems - Part I", IEEE Trans. on Electr. Insul., Vol EI-5, pp113-121, December 1970.

[12] Smyth, C. P., Dielectric Behavior and Structure, pp53-59, McGraw-Hill, New York, 1955.

[13] Hakim, R. M., "The Effect of Oxidation on the Dielectric Properties of an Insulating Oil", IEEE Trans. on Electr. Insul., Vol EI-7, pp185-195, December 1972.

[14] Yasufuku, S., Umemura, T., and Tanii, T., "Electric Conduction Phenomena and Carrier Mobility Behavior in Dielectric Fluids", IEEE Trans. Electr. Insul., Vol EI-14, pp28-35, February 1979.

[15] Adamczewiski, I., Ionization Conductivity and Breakdown in Dielectric Liquids, pp112, Taylor & Francis, London, 1969.

[16] Delahay, P., Double Layer and Electrode Kinetics,

pp1-32, Interscience Publishers, New York, 1965.

[17] Goffaux, R., "Sur Les Proprietes Electriques de Dielectriques Solides aux Tres Basses Frequences", Memoire de l'Academie royale de Belgiques, XXXVIII, 1968.

[18] Gartner, E., and Tobazeon, R., "On the behavior of Liquid/Solid Insulation at Very Low Frequencies", IEEE Trans. on Electr. Insul., Vol EI-12, pp86-89, February 1977.

[19] Bartnikas, R., "Electrical Conduction in Medium Viscosity Oil-Paper Films - Part I", IEEE Trans. on Electr. Insul., Vol EI-9, pp404-413 , June 1974.

[20] Ohashi, a., Shimokawa, H., and Ueda, M., "Dielectric Properties of Silicone Liquid Films, IEEE Int'l Symp. on Electr. Insul., pp245-248, 1978.

[21] Tobazeon, r., and Garton, E., "On the Behavior of Ions at Insulator/Liquid Interfaces and its Consequences for the Losses in Impregnated Insulation", Conference on Electrical Insulation and Dielectric Phenomena , pp404-413, National Academy of Sciences, Washington, D.C., 1975.

[22] Umemura, T., Akiyam, K., and Kashiwazak, T., "Dielectric Behavior of Solid/Liquid Insulation system", IEEE Trans. on Electr. Insul., Vol EI-17, pp276-280, June 1982.

[23] EPRI, "Characteristics of Insulating Oil for Electrical Application", December, 1979.

[24] El-Sulaiman, A. A., Ahmed, A. S., Quresh, M. I., and Hassan, M. M. A., "High Field DC Conduction Current and Spectroscopy of aged Transformer Oil", IEEE Trans. on PAS, Vol PAS-101, pp4358-4360, November 1982.

[25] Crine, J. P., Duval, M. and Lamarre, C., "Evaluation of Transformer Oil Aging Under Service Load from Various Chemical and Dielectric Measurements", IEEE Intl. Symp. on Electr. Insul., pp35-37, 1982.

[26] Cesar, L. C., "Aging Studies of Paraffin Base Transformer Oil", IEEE Intl. Symp. on Electr. Insul, pp167-171, 1983.

[27] Gussenbauer, I., "Examination of Humidity Distribution in Transformers by Means of Dielectric Measurements", Int'l Conf. on Large High Voltage Electric Systems, August 27-September 4, 1980.

[28] Howe, A. F., "Diffusion of Moisture Through Power-Transformer Insulation", Proc. IEE, Vol 125, October 1978.

[29] Guizonnier, R., "Nature des Porteurs de Charges", Conf. on Conduction Processes in Dielectric Liquids, pp251-255, September 17-19, 1968.

[30] Oomen, T. V., "Moisture Equilibrium in Paper-Oil Insulation Systems", IEEE Int'l Symp. on Electr. Insul., pp162-166, 1983.

[31] ASTM D1533.

[32] Szepes, L., Torkos, K., and Dobo, R., "A New Analytical Method for the Determination of the Water Content of

Transformer Oil", IEEE Trans. on Electr. Insul., Vol EI-17, August 1982.

[33] Melcher, J. R., <u>Continuum Electromechanics</u> , pp2.33, The M.I.T. Press, Cambridge, Massachusetts, 1981.

[34] Melcher, J. R., <u>Continuum Electromechanics</u> , sec. 4.5, The M.I.T. Press, Cambridge, Massachusetts, 1981.

[35] Melcher, J. R., <u>Continuum Electromechanics</u> , pp 2.35, The M.I.T. Press, Cambridge, Massachusetts, 1981.

[36] Toomer, R., and Lewis, T. J., "The Effect of Metal Electroes on Insulationg Surfaces", 3rd Int'l Conf. on Dielectric Materails Measurements and Applcations, 10-13 September, 1979.

[37] Shell Chemical Company, Technical Bulletin, sc:164-77, February 1977.

[38] Macdonald, J. R., "Interface Effects in the Electrical Response of Non-metallic Conducting Solids and Liquids", Conf on Electric Insulation and Dielectric Phenomena, 1980.

[39] Vetter, K. J., <u>Electrochemical Kinetics</u> , pp345-354, Academic Press, New York, 1967

[40] Vetter, K. J., <u>Electrochemical Kinetics</u> , pp188-193, Academic Press, New York, 1967.

[41] Melcher, J. R., <u>Continuum Electromechanics</u> , pp10.3, The M.I.T. Press, Cambridge, Massachusetts, 1981.

[42] Vetter, K. J., <u>Electrochemical Kinetics</u> pp200-205, Academic Press, New York, 1967.

[43] Davies, J. T., and Rideal, E. K., <u>Interfacial Phenomena</u>

, pp1Ø8, Academic Press, New York, 1963

[44] Koelmans, H., "Metallization Corrosion in Silicon Devices by Moisture Induced Electrolysis", IEEE 12th Rel. Phys. Symp., pp168-171, 1974.

[45] Orszag, S. A., "Spectral Methods for Problems in Complex Geometries", Proc. of mini symposium on the state of the art in computational fluid dynamics, AIAA, pp273-3Ø5, Boston, March 1984.